Thermal Conductivity and Dynamics of a Chain of Free and Bound Particles

by

Dominic J.R. Mimnagh

B.Sc., York University, 1989

M.Sc., York University, 1991

A THESIS SUBMITTED IN PARTIAL FULFILLMENT
OF THE REQUIREMENTS FOR THE DEGREE OF
DOCTOR OF PHILOSOPHY
in the Department
of
Physics

SIMON FRASER UNIVERSITY
November 1997

APPROVAL

Name: Dominic J.R. Mimnagh

Degree: Ph.D.

Title of thesis: Thermal Conductivity and Dynamics of a Chain of Free and Bound Particles

Examining Committee: Dr. Mike Plischke
Chair

Dr. Leslie Ballentine
Professor, Dept. of Physics
Senior Supervisor

Dr. Robert Russell
Professor, Dept. of Mathematics
Supervisory Committee Member

Dr. John Bechhoefer
Associate Professor, Dept. of Physics
Supervisory Committee Member

Dr. Michael Wortis
Professor, Dept. of Physics
Internal Examiner

Dr. E. Atlee Jackson
Professor, Dept. of Physics
University of Illinois at Urbana-Champaign
External Examiner

Date Approved:

PARTIAL COPYRIGHT LICENSE

Title of Thesis/~~Project/Extended Essay~~

Thermal Conductivity and Dynamics of a Chain of Free and Bound Particles.

Author:
(signature)

(name)

(date)

Abstract

The proportionality of heat current, J, to temperature gradient, ∇T, is an accepted tenet of thermal physics, Fourier's law, and can be written as $J = -\kappa \nabla T$, where κ represents the thermal conductivity. This behaviour has been shown empirically, but is difficult to derive from first principles. In the past, the thermal conductivity has been calculated for many different dynamical models to help shed light on the foundations of Fourier's law. Systems that have a finite κ that is also an intensive property of the lattice are considered to have normal thermal conductivity. Surprisingly, this property has been demonstrated for only two dynamical systems. One is the well known Toda model (a lattice of exponentially bound particles) the other is the ding-a-ling model (a lattice of alternately free and harmonically bound particles) [G. Casati, J. Ford, F. Vivaldi, and W. M. Visscher, Physical Review Letters **52**, 1861 (1984)].

The initial aim of the research was to measure dynamic quantities of the ding-a-ling model and to look for correlations with a possible transition to normal thermal conductivity. This work was delayed initially when we were unable to confirm Casati, Ford, Vivaldi, and Visscher's (CFVV) assertion that the thermal conductivity of the ding-a-ling model was independent of chain length. We have shown that what CFVV quote as an asymptotic value of κ is only a transitory plateau, and κ actually increases for longer chains. Ultimately, however, a saturation value can be established and CFVV's conclusion that the ding-a-ling model displays normal thermal conductivity is correct. In fact, the model appears to possess normal thermal conductivity for all parameter values explored, though it does demonstrate a transition in the length of chain needed to observe this Fourier law behaviour. We were able to demonstrate that this transition in scale coincides with transitions in a number of dynamical measures of the system, such as, the collision rate, the energy density, and the Lyapunov exponent λ. The change in scaling law seen for λ is known to correspond to a transition to total chaos, where all stable regions of phase space have vanished. To examine this further, we have explored the Poincaré sections for the two particle periodic ding-a-ling lattice, including the existence and stability of fixed points.

The numerical tractability of the system enabled large amounts of data to be calculated to ensure the robustness of the results and to attain very good statistics. We were able to establish a $N^{-\frac{1}{2}}$ length dependence of κ as it approached its asymptotic value. As well, we quantified the slight curvature observed in the temperature profile due to the temperature dependence of κ. Also the simplicity of the model enabled us to get good analytic estimates of dynamical quantities (such as collision rate and energy density), which were confirmed numerically.

Contents

List of Tables

List of Figures

Chapter 1

Introduction

Although Fourier's law of heat conduction (heat current being proportional to the thermal gradient) is very commonly observed, it is far from clear what properties of the dynamical system are responsible for the observed behaviour. "Neither phenomenological nor fundamental transport theory can predict whether or not a given classical many-body Hamiltonian system yields an energy transport governed by the Fourier heat law." So reads the first sentence of the paper by Casati, Ford, Vivaldi, and Visscher [CFVV84](CFVV), in which they introduced the so-called ding-a-ling model, as the simplest system in which the Fourier heat conduction law could be demonstrated. The model consists of a one-dimensional chain of atoms, alternately free and harmonically bound, which interact through hard elastic collisions. CFVV demonstrated that this model exhibits chaotic dynamics, and presented numerical evidence that, for moderately long chains, the thermal conductivity approaches a value independent of the length of the chain.

The impetus for studying the relationship between dynamics and nonequilibrium statistical mechanics began with the work of Boltzmann. The Boltzmann transport equation is the basis of much of kinetic theory and is quite physically intuitive. All that is required is the equations of motion of the particles (a dilute gas) and the assumption of a random velocity distribution prior to each collision event. This randomness assumption (the "Stosszahlansatz"), while physically reasonable, has little rigorous basis. Nonetheless, its widespread success has given physicists great confidence in its correctness. In 1929 Peierls [Pei29] generalized the Boltzmann equation to apply to the interaction of phonons in solids. This was less physically intuitive, since phonons do not possess well-defined positions and velocities as do particles in a gas. Nevertheless, Peierls provided a framework for much of the theoretical work in the study of thermal conduction in solids. In particular, he identified some phonon collision processes, due to lattice anharmonicity (Umklapp processes), which do not conserve momentum and lead to thermal resistance.

With the advent of the computer as a research tool in the early 1950s came the opportunity to test some of these theories. The celebrated work of Fermi, Pasta, and Ulam (FPU), lucidly reviewed by Ford [For92], pioneered the use of this tool and uncovered a wealth of new physics. FPU studied a harmonic chain with weak nonlinearity. Instead of the expected equipartition of energy among the modes, they found a recurrent behaviour, which is now known to be related to the Kolmogorov, Arnold, Moser (KAM) theorem, but which was originally very puzzling. In particular, the mode overlap criteria put forward by Izrailev and Chirikov [IC66] proposed a critical energy for widespread chaos. This would effectively couple the normal modes and allow equipartition to take place at a parameter range different from those tried by FPU. Northcote and Potts [NP64] were able to show energy sharing among normal modes of the harmonic-plus-hardcore potential (a lattice of harmonically coupled finite-sized particles with hard collisions). In a series of recent papers, Pettini and co-workers have quantified the time scale for the approach to equipartition, using both analytic [CLP95] and numerical [PL90] [PCS91] techniques. Furthermore, they have established that as long as there are regions of chaos present in the phase space of their dynamical systems, their systems always approach equipartition. They do, however, observe a change in time scale at the energy corresponding to a transition to total chaos (an absence of any stable regions in phase space).

This study of the temporal aspects of energy transport has been complemented by a great deal of work on the spatial aspects of energy transport, heat conduction. The theory of how heat conducts through non-metallic solids has quite successfully been shown to conform to the empirical Fourier law, which can be written as $J = -\kappa \nabla T$, where J is the heat current, ∇T the temperature gradient, and κ represents the thermal conductivity. In terms of the phonon picture of Peierls, the value of κ is governed by the mean free path length l of the phonons,

$$\kappa \propto Cvl, \tag{1.1}$$

where C is the specific heat per unit volume, and v is the sound velocity. In real materials, there are many factors that contribute to the measured value of κ, for example there are defects, impurities, dislocations, and Umklapp processes due to the anharmonic interatomic potentials. The most obvious starting point for a theoretical justification of Fourier's law would be to place a 1d chain of coupled harmonic oscillators between two simulated reservoirs at different temperatures. Though there are no resistive mechanisms, its simplicity allows for analytic solution, as was done by Rieder *et al.* [RLL67] in 1967. He found that the heat flux was proportional to the temperature difference instead of the temperature gradient and, so, did not obey Fourier's law. Away from the reservoirs the particles had approximately the mean temperature of the two reservoirs. This failure for the harmonic lattice can be attributed to the lack of coupling in the normal modes. Dean [Dea60] [Dea61] took the firsts steps to identifying the crucial ingredients in establishing normal thermal conductivity. He studied the effect of adding disorder to the harmonic lattice. This approach recognizes that even the purest crystal contains isotopic impurities; thus, by using a random mass distribution it was hoped that the problems of the simple harmonic lattice would be overcome. However, analysis of the spectra revealed that the disorder caused localization of the high frequency modes and failed to make the thermal conductivity normal. The disorder did result in a temperature gradient and, therefore, a finite κ. The length dependence of this κ was worked out by Ishii and Matsuda [MI70] [Ish73]. For free ends, they found $\kappa \propto N^{\frac{1}{2}}$; while for fixed ends, they found $\kappa \propto N^{-\frac{1}{2}}$. This was confirmed numerically by Visscher [Vis71].

Many lattices were tested to see the effect of adding anharmonicity to disordered systems. For instance, Payton *et al.* [PRV67] investigated a disordered system with and without Lennard-Jones anharmonicity. They found that the addition of the anharmonicity increased the calculated conductivity. This same dependence was found by Jackson *et al.* [JPW68] in a system with cubic anharmonicity. This result was surprising, since, from the phonon description of heat conduction, one would consider this a resistive mechanism of phonon scattering. An explanation is that the anharmonicity acts to couple the localized high-frequency modes to the low-frequency modes, increasing conduction. Since introducing these anharmonic terms to the dynamics generally makes the systems more computationally intensive, the length dependence of κ was not tested.

With the introduction of anharmonicity into the discussion, we switch from the phonon as the particle-like carrier of energy to the soliton. This also leads to an energy flux proportional to the temperature difference, and, so, a nonlinear lattice with only soliton energy transport will also not obey Fourier's law. Toda [Tod79] has reviewed the relevant concepts related to solitons and heat conduction, as well as covering an argument linking solitons to the increase of κ found by adding anharmonicity to disorder. Miura [Miu73] investigated the collisions of solitons in a harmonic-plus-hardcore lattice and found some energy loss due to the collisions. This was an indication that diffusive energy transport could result from the decaying solitons.

Because of the difficulties found by FPU and others, many people came to believe that normal thermal conductivity could not occur in one dimension [MT78]. These arguments relate to the fact that we can at best expect only a subset of the 2 and 3 dimensional physics to appear in 1-d. For instance, we cannot expect to see turbulence in a 1-d lattice. The lack of interaction of longitudinal and transverse modes might alter the fundamental character of thermal conductivity.

Eventually, however, Mokross and Büttner [MB83] gave evidence that the diatomic Toda lattice exhibited a transition to normal thermal conductivity, which later was verified by the more detailed numerical investigation of Jackson and Mistriotis [JM89]. The monatomic Toda [Tod75] lattice uses exponential coupling and has an integrable Hamiltonian. The diatomic Toda lattice has the mass ratio of the adjacent pairs of particles, r, as a variable parameter. At $r = 1$ the diatomic Toda lattice reverts to its integrable monatomic form. For $r = 0.5$, Mokross and Büttner found indications of Fourier-law behaviour. Jackson and Mistriotis found a larger chain-length limit for the onset of normal thermal conductivity and also took the opportunity to investigate the transition to Fourier law conductivity. By calculating κ for a range of r and chain length, they confirmed length independence of κ for $0.5 \leq r \leq 0.75$, provided the chains contained at least 250 particles. Applying the concept of soliton decay via soliton collisions, they found that for the same range of r the soliton collisions produced optimal energy decay. Since it was presumed that chaos played a role, it would have been natural to consider the calculation of the Lyapunov exponent. However, this was rejected, since it is an indicator of the exponential separation of adjacent trajectories for *infinite* time. The argument was that this would be irrelevant for the time scale of pulse transits across the lattice. An alternative measure was suggested that measured sensitivity to initial conditions on the correct time scale. The separation of trajectories, $d(t)$, originally near the same point in phase space Γ are fitted to both an exponential and linear function for a short time τ. The better fit indicates the exponential or linear nature of the region of phase space. That is, for

$$\int_0^\tau dt \| d(t) - [B(\Gamma,\tau)t + C(\Gamma,\tau)] \|^2 < \int_0^\tau dt \| d(t) - [A(\Gamma,\tau)\exp(k(\Gamma,\tau)t] \|^2 \qquad (1.2)$$

the divergence is considered linear, where A, B, C and k are found from the fits. From a distribution of initial conditions they were able to show that the diatomic Toda lattice displayed exponential separation of trajectories on the relevant time scale for $0.5 \leq r \leq 0.75$, as above.

Soon after Mokross and Büttner had shown that the diatomic Toda lattice could support normal thermal conductivity, CFVV found a second such lattice, the ding-a-ling model. This persuasive work gave arguments for a direct connection between normal thermal conductivity and dynamical chaos in a very simple system. This simplicity made the model attractive from a computational point of view. They also showed that the value of the thermal conductivity given by the Green-Kubo formula is in agreement with that obtained directly from numerical simulation.

In recent years, the diatomic Toda lattice has received much of the attention in the study of thermal conduction. Gendel'man and Manevich [GM92] found analytic estimates of the value of κ in certain limiting cases. Nishiguchi and Sakuma [NS90] used the diatomic Toda lattice to investigate the effect of the temperature dependence of κ on the temperature profile. Also, they looked at separating the contribution to the flux by the soliton pulses (ballistic flux, as they called it) from that of the diffusive processes.

There have also been more failures in the search for Fourier-law models. A revisit of the Lennard-Jones [MA88] and FPU [KM93] lattices has still not been able to demonstrate Fourier-law behaviour in these systems, although perhaps longer lattices (and more computer power) are all that are needed.

Since the ding-a-ling model shows such promise as a tool for exploring the microscopic aspects of heat conduction, the original purpose of this work was to examine in more detail the relations between thermal conductivity and aspects of the dynamics, such as Lyapunov exponents. After reproducing the results of CFVV and extending them, we were surprised to discover that the conductivity value which they had reported as the long-chain limit was actually only a transitory plateau. The thermal conductivity does, indeed, converge to a long-chain limit, but only at lengths considerably greater than those reported by CFVV. Moreover, the approach to the long-chain limit can be non-monotonic as a function of length.

The ding-a-ling model, as well as some of the details of the techniques used to evolve it, are introduced in Ch. 2 of this thesis. In Ch. 3, we present results for the thermal conductivity, which confirm the earlier results of CFVV, as far as they went, but which also show surprising new results in regions that they did not explore. Also, we examine the methods used to calculate the quantities needed for the evaluation of κ, that is, the temperature gradient and the flux. The temperature dependence of κ causes some difficulties by introducing a curvature in the temperature profile. The shape of this curvature and measures to address its effect on the calculation of κ are discussed. The asymptotic limit of $1/\kappa$, for long chains, is analyzed in some detail including an analytic estimate of the value for stiff springs. In Ch. 4, we study the dynamics of the model, illustrating the distinctions between the weak-spring and stiff-spring limits and the transition between the limits. The paths traveled by colliding particles are used to provide physical intuition for these distinctions, as well as to provide visual evidence of soliton-like pulses. The average path length of these pulses is one of several measures, including the collision rate and energy density, that are used to quantify the onset of the transition from the stiff- to weak-spring limit. This transition appears to be linked to the onset of total chaos. Phase-space plots and the calculation of Lyapunov exponents are used to examine this point. With the identification of various properties of thermal conductivity in the ding-a-ling model, it is important to consider other models, as is done in Ch. 5. Here, we propose two models that share some similarities with the ding-a-ling model and discuss how the differences affect the evolution of the dynamical model. Finally, we summarize the conclusions in Ch. 6.

Chapter 2

The Ding-a-ling Model

The ding-a-ling lattice consists of a set of alternately free and bound particles. The Hamiltonian for the N particle ding-a-ling model, as described by CFVV, is

$$H = \frac{1}{2}\sum_{i=1}^{N}(v_i^2 + \omega_i^2 x_i^2) + \text{hard point core}, \tag{2.1}$$

where ω_i equals ω for even i and zero for odd i, all particles have unit mass, and the i^{th} particle has a position x_i measured relative to its lattice site, and a velocity v_i. Two versions of this model will be studied. To calculate the thermal conductivity, we use an open system – a chain with a free particle at each end, which interacts with a thermal reservoir. The reservoir assigns the free particle a random velocity from an appropriate distribution, and is discussed fully in Ch. 3. To calculate the Lyapunov exponent, we use a closed ring of particles. The open chains contain an odd number of particles and the closed rings contain an even number of particles.

The dynamics of a closed ring depends on only a single dimensionless parameter, $\varepsilon = E/\omega^2 l_0^2$, where E is the average energy per particle and l_0 is the lattice spacing. CFVV fix E and l_0, and use ω as a variable parameter. We use ε as our fundamental parameter and have confirmed the scaling by varying both E and ω in some of our calculations.

In the case of the chain interacting with reservoirs, the total energy is not fixed, so we must infer its average value from the temperature. The average temperature T_{m} is midway between the temperature of the left and right reservoirs, T_L and T_R.

If we assume equipartition, then the average energy of the free particles is $\frac{1}{2}T_{\mathrm{m}}$, and the average energy of the bound particles is T_{m}. This leads to an average energy of a system particle of $\frac{3}{4}T_{\mathrm{m}}$. So, the quantity

$$\varepsilon = \frac{3T_{\mathrm{m}}}{4\omega^2} \tag{2.2}$$

is used to parameterize our open system (we set $l_0 = 1$ and Boltzman's constant $k_B = 1$).

The parameter ε should be regarded as a conventional reparameterization of the temperature as a dimensionless energy. It is only approximately equal to the energy density (more precisely the dimensionless energy per particle). The average energy of a free particle is $\frac{1}{2}T$. The average total energy of a bound particle ranges from T in the low-density limit to $\frac{1}{2}T$ in the high energy density limit, where collisions prevent the spring from stretching very far. As a result, the true energy density ranges from ε to $\frac{2}{3}\varepsilon$, as we go from the low- to the high-density limits. No confusion will arise, provided we regard the values of ε for an open chain as merely re-expressing the temperature in dimensionless units. Only when a result computed at constant E is compared with one computed at constant T can any ambiguity of interpretation arise. This is done in Fig. 4.12, where it does not cause any trouble.

Between collisions, the motion has an analytic solution; in order to evolve it forward in time, one must simply calculate the time of the collision events and then evolve the system from collision to collision. This means that the system is more naturally described in terms of a mapping than as a solution to a Hamiltonian with infinite potentials to represent the hard collisions. However, since many of the physical quantities are calculated per unit time, rather than per collision, it is necessary to have a mixed notation. A superscript 0 will identify quantities measured just after the collision, and this quantity will have a j subscript to identify which collision. For instance, x_{ij}^0 and v_{ij}^0 represent the position relative to its lattice site and velocity for particle i at the time just after collision j, while $x_i(t)$ and $v_i(t)$ represent the same quantities at the arbitrary time t, measured relative to the first collision. The evolution of the position of particle i between collision j and $j+1$ is

$$x_i(t) = \begin{cases} A^0_{ij}\sin(\omega(t-\tau_j)+\phi^0_{ij}) & i \text{ even} \\ v^0_{ij}(t-\tau_j)+x^0_{ij} & i \text{ odd} \end{cases} \tag{2.3}$$
$$\text{for } \tau_j < t \le \tau_{j+1},$$

where A^0_{ij} and ϕ^0_{ij} are the amplitude and phase of the oscillator, and τ_j is the time of the collision j. In order to calculate the time of collision j, we must find the possible collision time t^0_{ij} for each particle pair i and $i+1$ such that

$$x_i(t^0_{ij}) - x_{i+1}(t^0_{ij}) = 1, \tag{2.4}$$

the term 1 being the lattice spacing. Then we select the earliest collision time as the actual collision time for the system. To complete the collision we must evolve the system to time τ_j, then exchange the velocities of the particles involved in the collision. If we define the system's state (made up of all its position and velocity coordinates) after collision j by $\mathbf{\Gamma}^0_j$, then

$$\mathbf{\Gamma}^0_j = f(\mathbf{\Gamma}^0_{j-1}) \tag{2.5}$$

maps the physical system from the time of system collision $j-1$ to system collision j, and swaps the velocities of the pair of particles involved in the collision.

2.1 Evolution of the model

Following the procedure outlined above, one can design an efficient algorithm to evolve the system forward in time. Some care does need to be taken in the root-solving phase of the calculation, as this is where the bulk of the computation takes place.

Root solving is accomplished by combining Brent's technique with the Secant method. Brent's technique is outlined in Numerical Recipes[PTVF92] and is guaranteed to converge but is not as fast as the less reliable secant method. So, Brent's method is used initially to get close to the root and then, the secant method is used to complete the calculation to an accuracy of 10^{-10}. If the secant method fails for some reason, then Brent's method is used for the complete calculation.

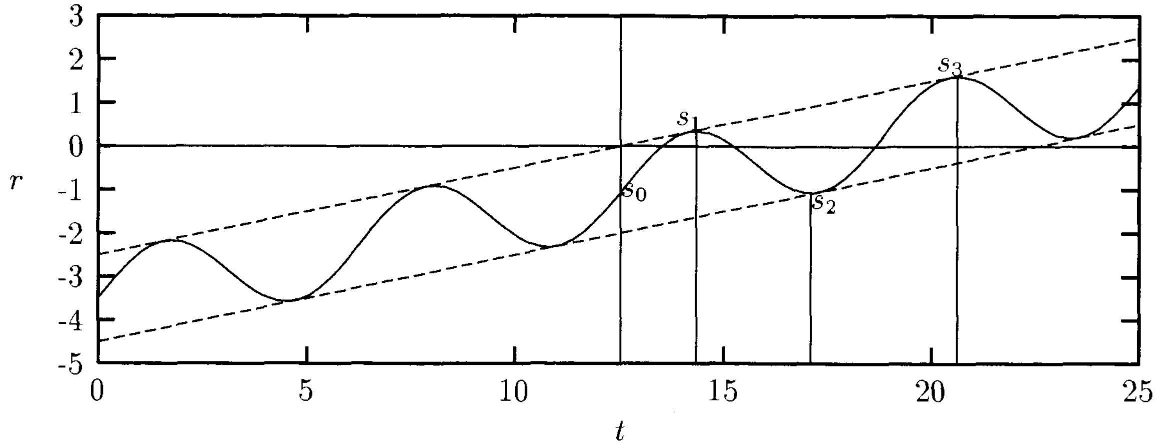

Figure 2.1: The collision function as a function of time. The function is evaluated at each s_i until the sign of s_i changes indicating that the root is bounded.

Theoretically, an advantage of using a map such as the ding-a-ling system over an ODE is that between collisions the dynamics is analytic so we don't need to evaluate the functions at the intervening times. However, the root solver requires that we have points on either side of the root to begin with. Naively evaluating our collision function at discrete time steps to bracket this root would negate the computational advantage of the model over models that require the solution of an ODE. Also, we risk stepping over a possible root thus missing a collision.

The collision function can be written as

$$r_{i\,j+1}(t) = (A^0_{ij}\sin(\omega(t-\tau_j)+\phi^0_{ij})) - (v^0_{i+1\,j}(t-\tau_j)+x^0_{i+1\,j}) - 1, \qquad (2.6)$$

where we have used Eq. (2.4) and Eq. (2.3). (Note this is the collision of a bound particle on the left and a free particle on the right. There is a complementary equation for the reverse situation.) This function has been plotted in Fig. 2.1 to demonstrate the root-bracketing strategy. First, there can be no collision unless the free particle is within ±A of the bound particles (between the dashed lines in the figure). Thus the function is evaluated at s_0. Now in order that we do not step over any possible roots, we evaluate r at the minima and maxima (s_1, s_2, and s_3). With this strategy,

(a) Weak Springs

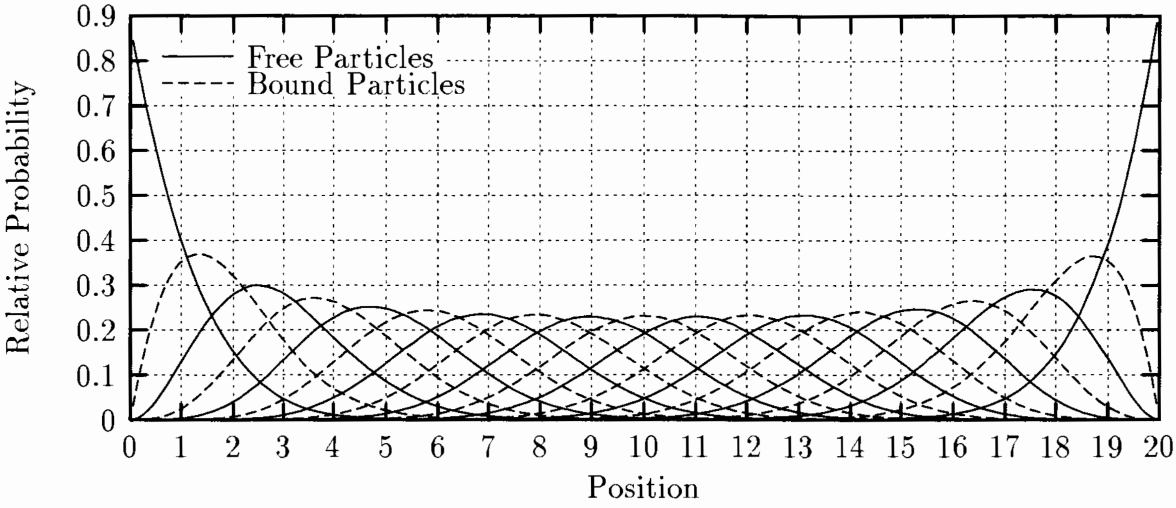

(b) Stiff Springs

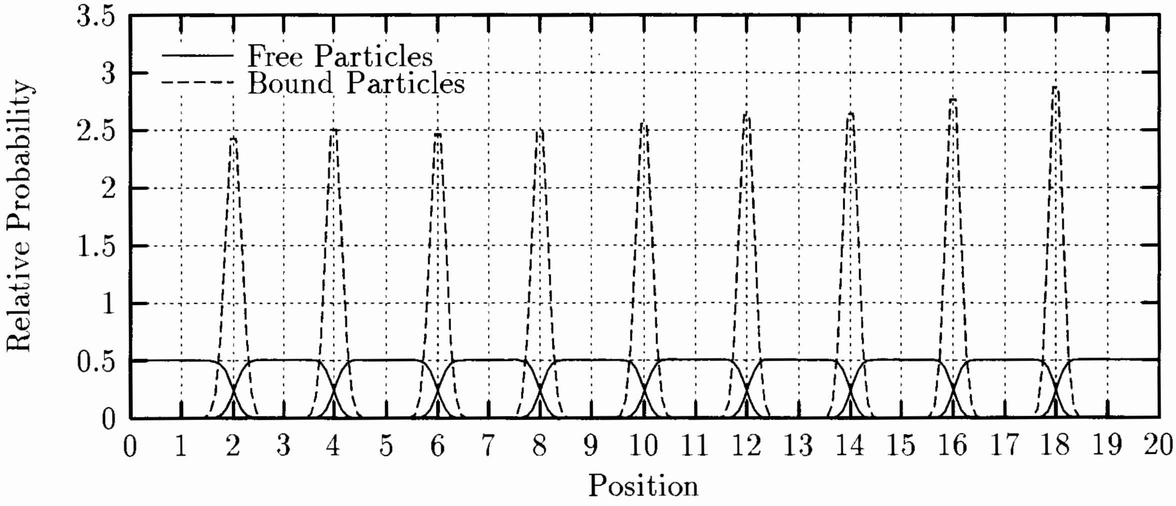

Figure 2.2: The position distribution for weak and stiff springs (a) $\omega = .3$ ($\varepsilon = 16.7$) (b) $\omega = 10$ ($\varepsilon = .015$).

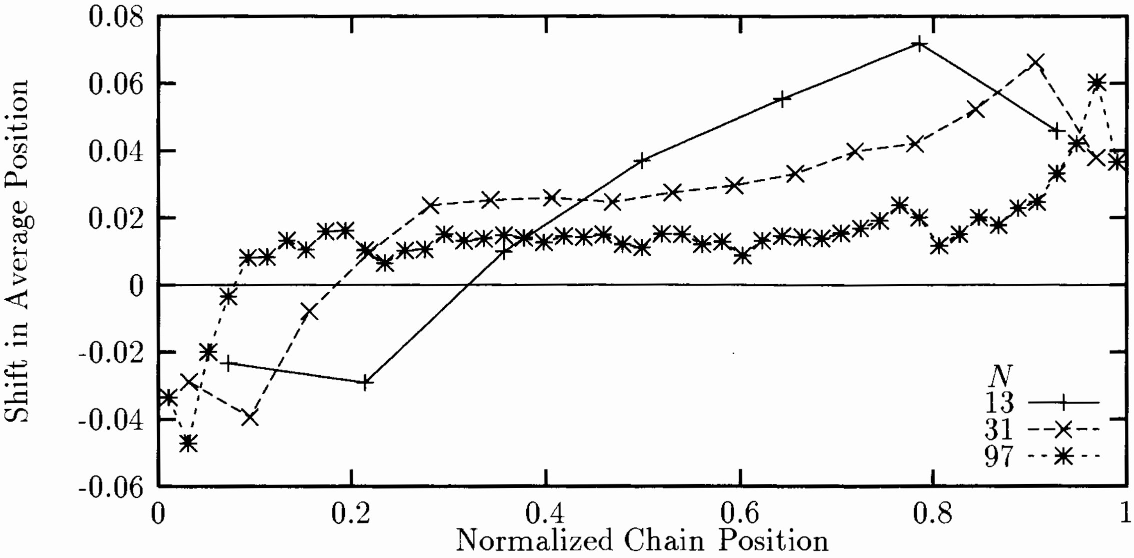

Figure 2.3: The shift in the average position of the particles relative to their lattice sites for various chain lengths N.

we can expect to bracket the root in a minimum number of steps.

Evolving this model in time allows us to discover its position-distribution characteristics. In Fig. 2.2(a), we see that, except for the end particles, both the free and bound particles display similar Gaussian distributions for this weak-spring example. Fig. 2.2(b) demonstrates the changes seen when we use a stiffer spring. In particular, the bound particles are much more localized, and the free particles' probability distributions become flat away from the bound particles, as one would expect. Also, the peaks in the distributions for the bound particles are higher on the right, since this is the cold end of the lattice where they are more tightly bound.

As seen in Fig. 2.2, the position distributions are not perfect Gaussians. The actual average positions of the particles were calculated in Fig. 2.3, where we see the error in assuming the particles average position is at their lattice sites does not exceed ±0.1 which is acceptable. It is interesting that one can see the systematic offset caused by the constant flux of energy from left to right.

Chapter 3

Calculation of the thermal conductivity

3.1 Method of Calculation

The calculation of the thermal conductivity for the system is performed in a manner similar to that described in CFVV [CFVV84]. A temperature difference ΔT is placed across the lattice to create a temperature gradient ∇T and the energy flux J is then monitored. The thermal conductivity k is $-J/\nabla T$. To establish the temperature gradient, we place heat reservoirs at different temperatures at either end of the lattice. These are random number generators that take the particles that enter the reservoir and eject them back into the system with a velocity of the appropriate distribution. The probability distribution used is

$$P(v) = (|v|/T)\exp(-v^2/2T), \tag{3.1}$$

which is the velocity distribution for particles ejected from a pinhole in the side of an oven. The difference between the energy of the particles entering and leaving during the m^{th} reservoir interaction, ΔE_m, is used in the calculation of the flux,

$$J_n = \frac{1}{t_n} \sum_{m=1}^{n} \Delta E_m, \tag{3.2}$$

where t_n represents the time of the n^{th} reservoir interactions. After eliminating the initial transients, we calculate a sufficient number of collisions so that $J_n \approx J_\infty$. The value of the local temperature is calculated as twice the average kinetic energy of each particle. Then, we assume that the position of the particles is, on average, at its lattice site and we perform a linear fit to the data. The slope is the effective temperature gradient,∇T_{eff}. It will, in general, differ from the applied temperature gradient, ∇T_{app}, because there is a temperature jump at the ends of the lattice, similar to a Kapitza resistance. For this reason, the end particles are never included in any of our ∇T_{eff} calculations. They function merely as the interface between the reservoir and the system.

To compare the results for different parameter values, we find it useful to consider dimensionless quantities. For example, $\mathcal{J} \equiv J/\omega^3$ is a dimensionless flux, and $\kappa \equiv k/\omega$ is a dimensionless thermal conductivity. We have found, as expected, that we obtain approximately the same κ for different T_{m} and ω, if they are chosen such that ε is constant.

3.2 Details of Convergence

In the calculation of κ, many tests and checks are performed to validate the converged value. First, the initial conditions are set up and the system is evolved to eliminate initial transients; then the relevant quantities are calculated. When fluctuations are sufficiently small, the results are output.

The initial conditions are chosen so as to minimize the time it takes to bring the system to an equilibrium state. For short lattices, the velocities were chosen such that $v = \sqrt{T}g$, where g is a Gaussian distributed random number. The positions of the bound particles were set to $x = g\sqrt{T}/\omega$. Then a free particle would be placed between each pair of bound particles with a uniform probability distribution. If the position of any two bound particles overlapped, then the whole set was rejected. The energy was then scaled to the desired energy by scaling the velocity and position of the particles. Initial conditions generated in this fashion produce position distribution similar to those seen in the evolution of the system (see Fig. 2.2).

For longer lattices, however, this process was too time consuming, and a simpler system was used. The velocity of each particle was chosen to give the correct energy at its position in the temperature gradient. The bound particles were placed on their origins and the free particles were given a uniform distribution between -1 and $+1$.

Now, the system is evolved forward, and the flux is calculated. The flux at both reservoirs is calculated; once the difference is less than 1%, the system is deemed to have reached a steady state. Now, this transient data is discarded, and the main calculation phase is begun.

To calculate κ, we need to calculate the slope of the temperature gradient and the flux through the lattice. To establish convergence criteria, we estimate the standard deviation in the flux, $\sigma_{\mathcal{J}}$, and the standard deviation in the temperature of one of the particles, σ_T. This is done by calculating $\mathcal{J}$ and T for a reasonable-sized time bin. The fluctuations in these quantities are then used to estimate the relative error in κ,

$$\frac{\sigma_\kappa}{\kappa} = \frac{\sigma_{\mathcal{J}}}{\mathcal{J}} + \frac{\sigma_T}{T}. \tag{3.3}$$

When the calculation is sufficiently stable (typically a relative fluctuation of 1%) further tests are performed on the data to ensure that the result is not atypical. The continuously calculated values are not used unless they are within 1% of the binned averages. Also the fluxes at the two ends must be within 1% of each other. In Fig. 3.1, we see how the data converge in the particular case of $N = 11$ and $\varepsilon = 0.09375$ for an error in κ of 1%.

In Fig. 3.2, we see the time to achieve a 1% error in κ for various N. From the figure, we see that for shorter lattices, it takes a longer system time for convergence. For very long lattices, the convergence time seems to be independent of the chain length. This results because the error in κ (the main stopping criteria) has two contributions, the error in ∇T and $\mathcal{J}$. When the lattice is long, the calculation of ∇T is easier since the linear fit of the temperature profile is improved with the increased number of data points. Since the sum of the two sources of error is constant, then the error in the flux must dominate in the very large lattices. The error in the flux is dependent mostly on the reservoir-interaction rate, which will be independent of N. In the small-N limit, the error in κ is mostly from the difficulty in calculating ∇T for

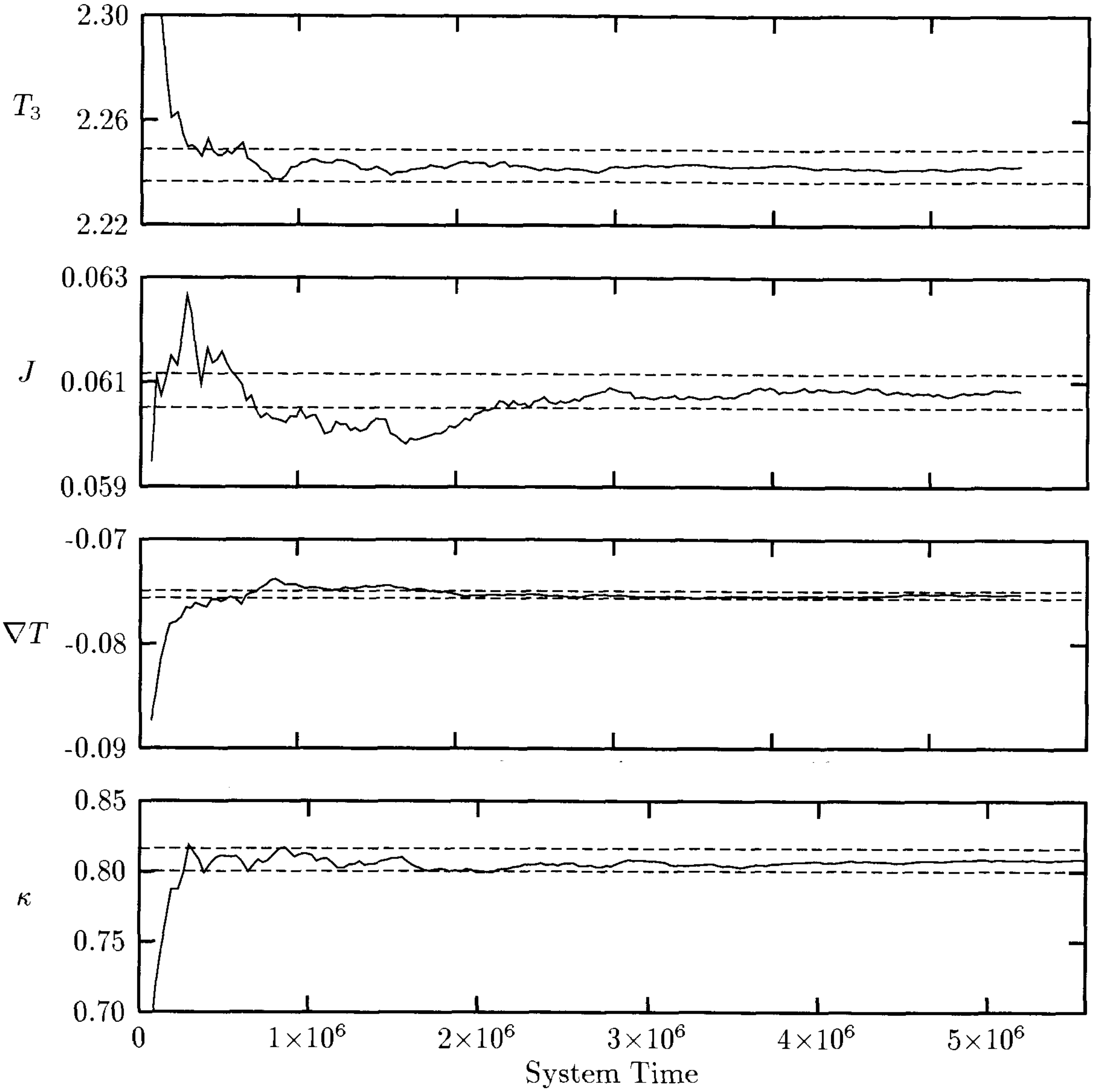

Figure 3.1: The convergence of T_3 the temperature of particle 3 (the second free particle on the left), the flux J, the temperature gradient ∇T, and the thermal conductivity κ. This data was calculated for $N = 11$ and $\varepsilon = 0.09375$ with the standard deviation σ_κ in the fluctuations of κ such that $\sigma_\kappa = 1\%$ at convergence. The dashed lines represent the measured σ in all quantities.

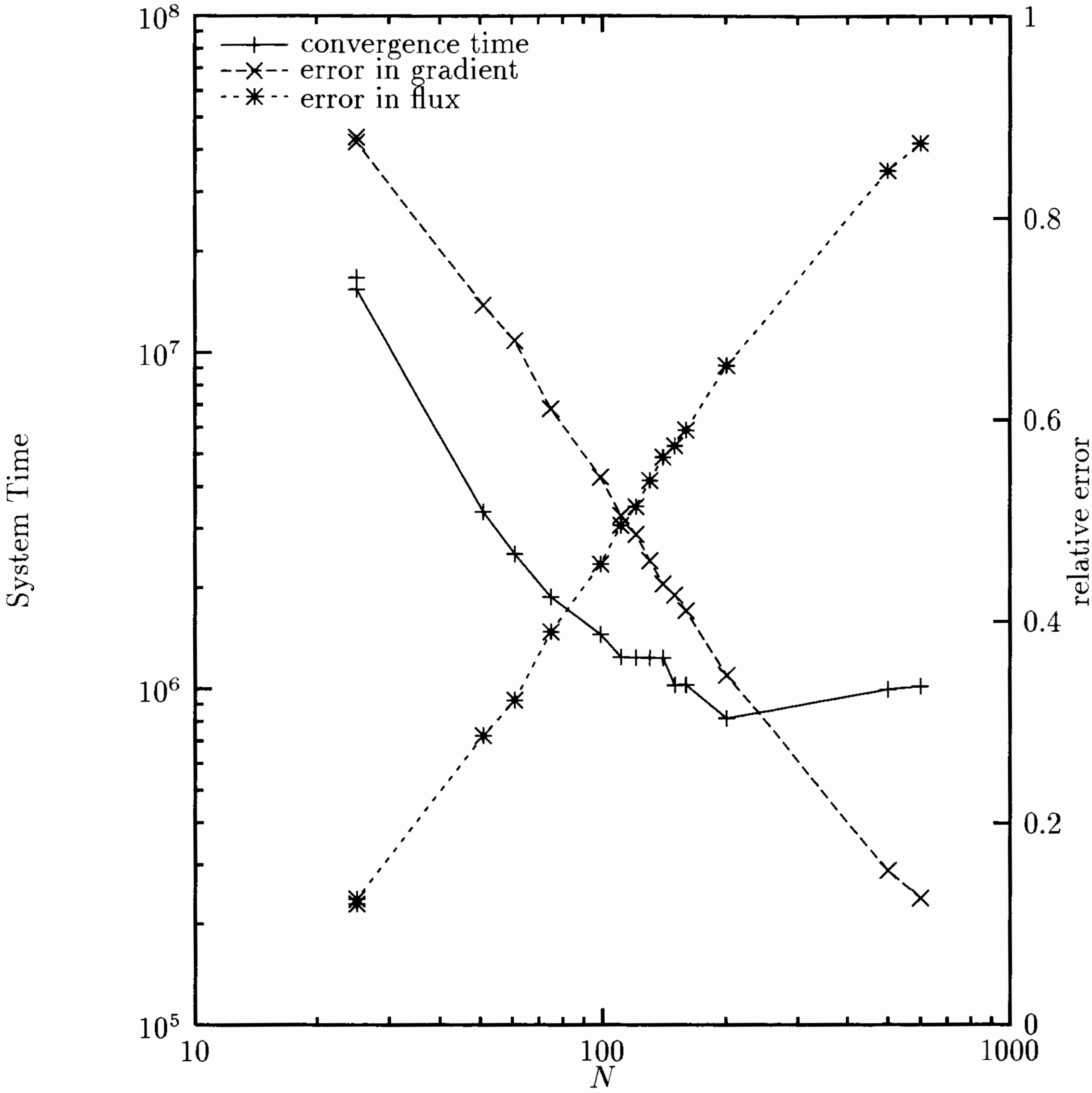

Figure 3.2: The system convergence time for various numbers of particles N with $\omega = .5$ ($\varepsilon = 6$).

short lattices; it gets worse the shorter the lattice.

The situation is a little different if we look at system convergence time as a function of ε. We see from Fig. 3.3 that there is a minimum. This feature can also be explained, once again, by discussing the contributions to the error. For small ε, the error in $\mathcal{J}$ dominates since a reduction in ε makes the system effectively colder and thus collisions with the reservoir are less frequent. As ε is increased, the system gets hotter and converges more quickly. For larger ε, the error in ∇T dominates. Because the Kapitza resistance is larger (see Fig. 3.4), the effective temperature gradient is smaller, so the relative error is larger due to fluctuations. Also, the larger energy creates larger fluctuations in T for the individual particles. This gets worse as ε gets larger. As a result convergence times are increased.

3.3 Calculation of ∇T

Fig. 3.4 shows the temperature profiles for a range of ε. For small ε (stiff springs), the coupling to the reservoirs appears to be good; while for large ε, there is a distinct temperature jump at the left ($T_\mathrm{L} = 2.5$) and right ($T_\mathrm{R} = 1.5$) reservoirs. These temperature jumps do not cause any particular concern, since we are only interested in the gradient of the profile, which is still uniquely defined by the linear fit to the data. However, since the smaller gradients do take longer to converge, this does affect the calculation. The slight curvature of the profiles is due to the temperature dependence of κ and will need to be addressed in the calculation of ∇T. As pointed out by Nishiguchi and Sakuma [NS90], the curvature in the temperature profile can be a source of error in the calculation of κ. We include only the central 60% of the particles in the calculation of ∇T. This section of the lattice has a much more linear T profile and, thus, a more accurate value of κ could be calculated. In Sect. 3.6, we will discuss the exact form of this curvature.

We explore the temperature jump more fully in Fig. 3.5, and we look at the way the shrinking reduces the effective temperature gradient in Fig. 3.6. The jumps are not symmetric at opposite reservoirs due to the curvature in the profile. This curvature also causes a reversal of the sign of the jump for the $\varepsilon = 0.015$ case shown. This

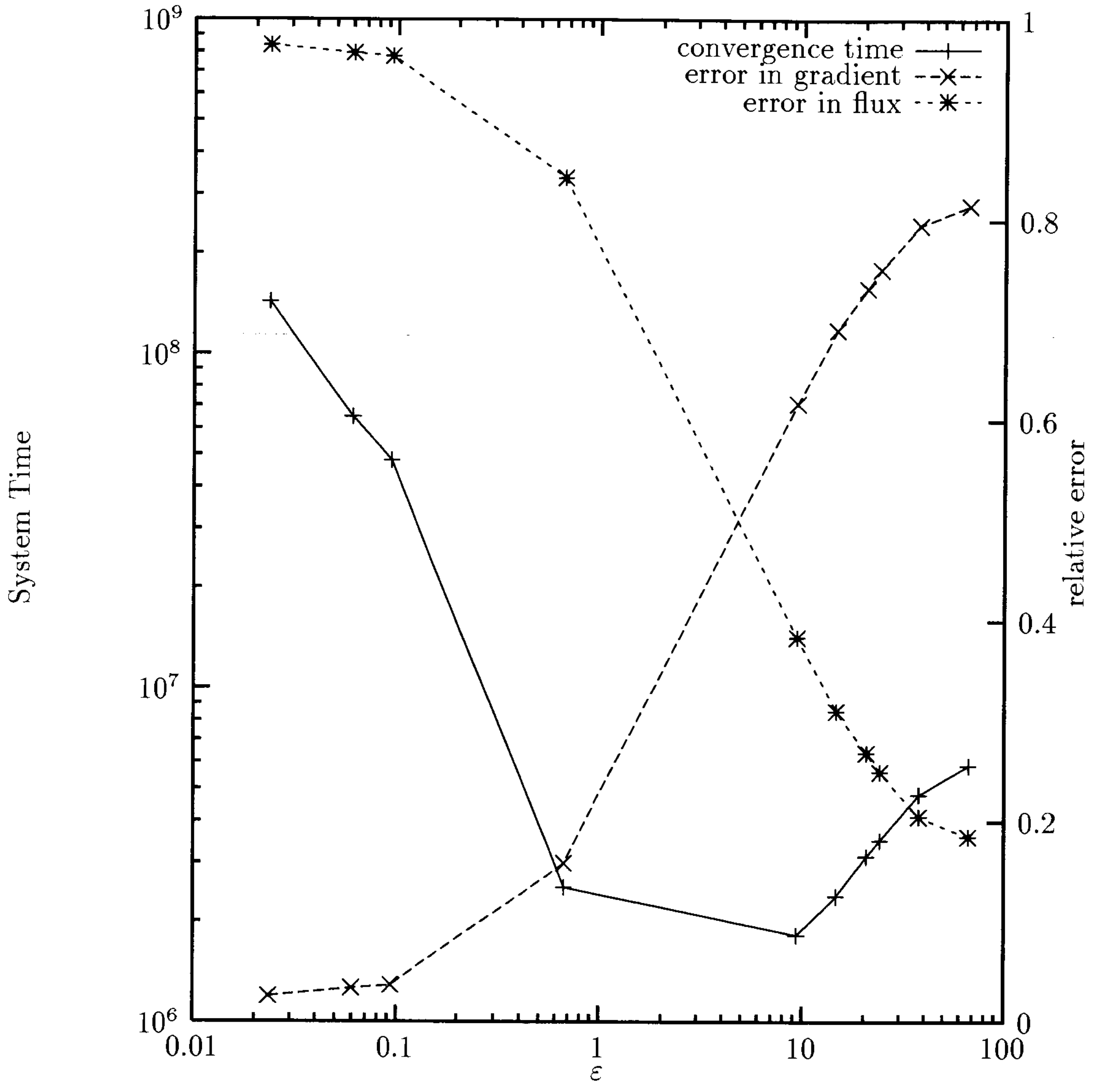

Figure 3.3: The system convergence time for ε with $N = 101$.

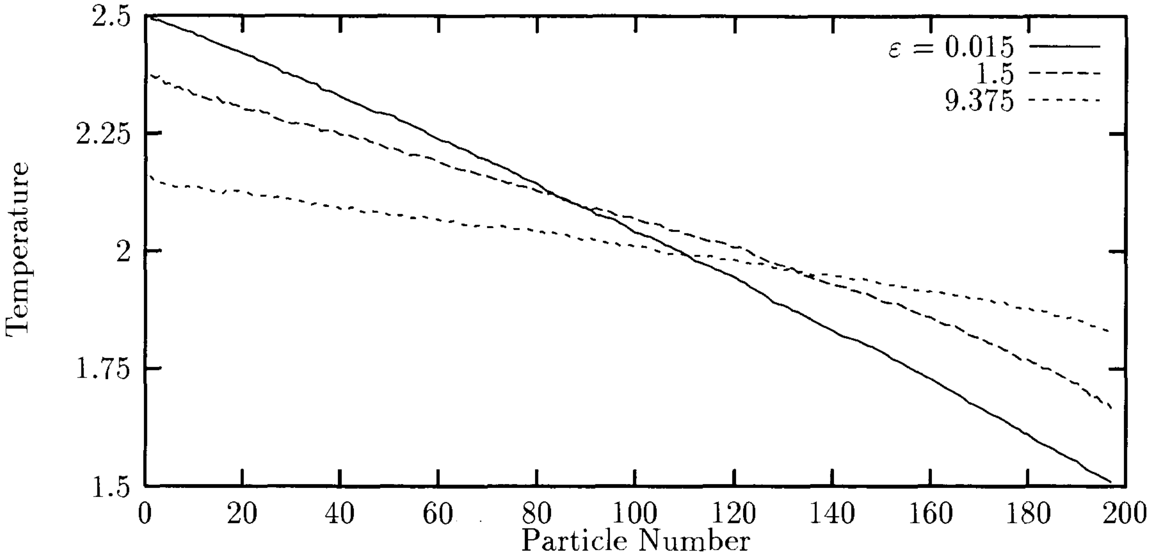

Figure 3.4: The temperature profile for various energy densities ε.

reversal can be seen more clearly in Fig. 3.5 in the case where we have fixed the length at $N = 9$, as a change in sign of the jump at around $\varepsilon = \varepsilon_c$. In Fig. 3.6 we see that this creates a slope such that $\nabla T_{\text{eff}} > \nabla T_{\text{app}}$ for small ε.

The behaviour of the gradient with varying chain length is shown in Fig. 3.7. We expect a $1/N$ dependence of ∇T from its definition as the slope of the temperature profile. This is clearly the reason $\nabla T \to 0$ for large N. However, for large ε, we also see $\nabla T \to 0$ as $N \to 0$. As we have just seen in Fig. 3.5 and Fig. 3.6, the temperature jumps are large in this limit, and a large temperature jump reduces ∇T_{eff}. A better understanding of the temperature jumps would help us to explain the size and position of these minima in ∇T (and the resulting minima in the plots of κ versus chain length we will see in Fig. 3.11). Both the role the soliton-like pulses play in the formation of the temperature gradient and these temperature jumps should also be explored.

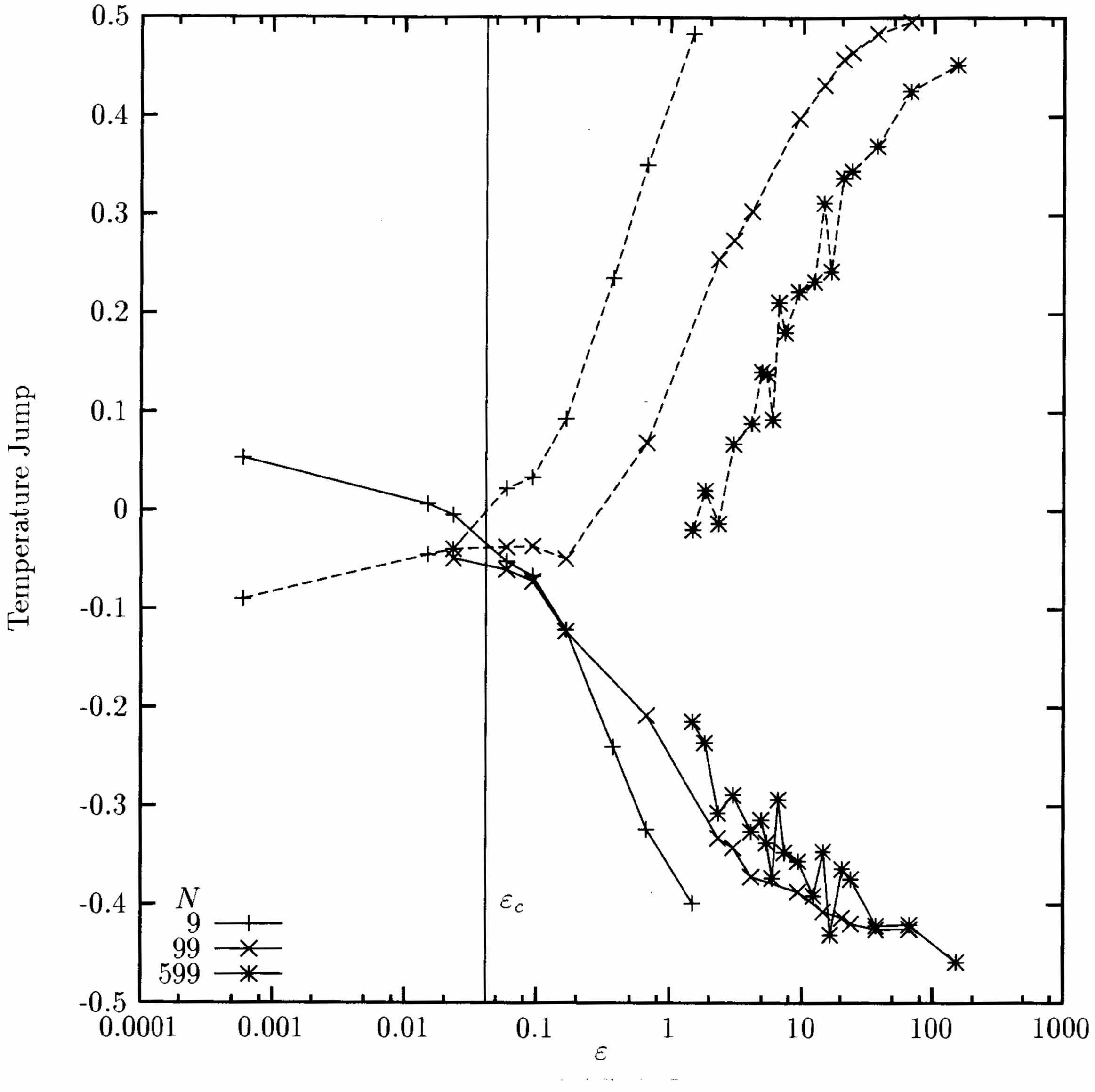

Figure 3.5: The difference between the temperature of the reservoir and the temperature evaluated from the linear fit at the position of the reservoir. The solid line corresponds to data evaluated for the left reservoir, while the dashed line corresponds to the right.

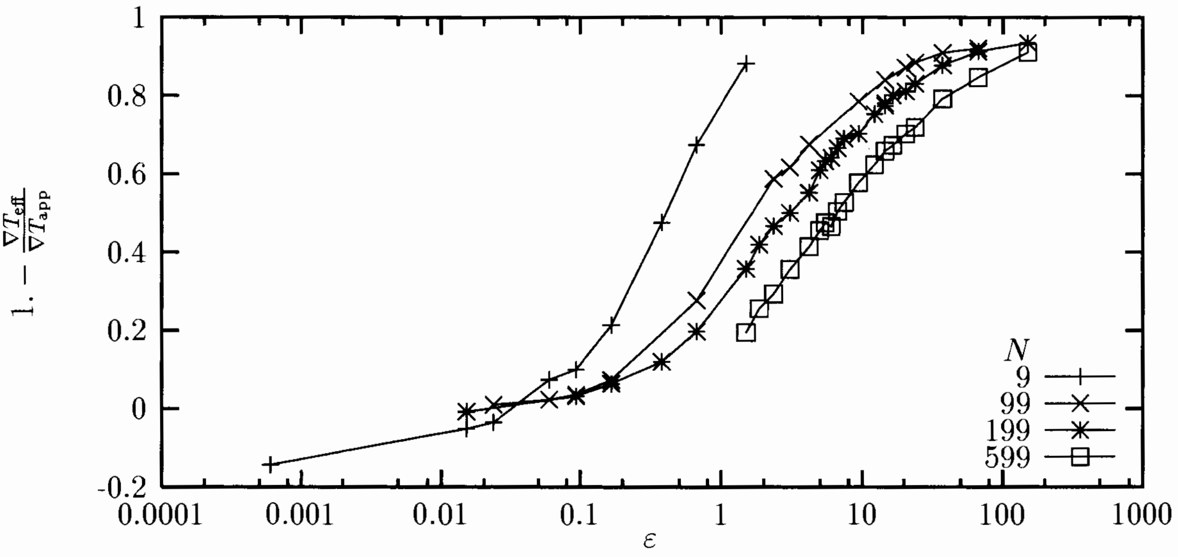

Figure 3.6: The normalized difference between the effective temperature gradient and the applied temperature gradient.

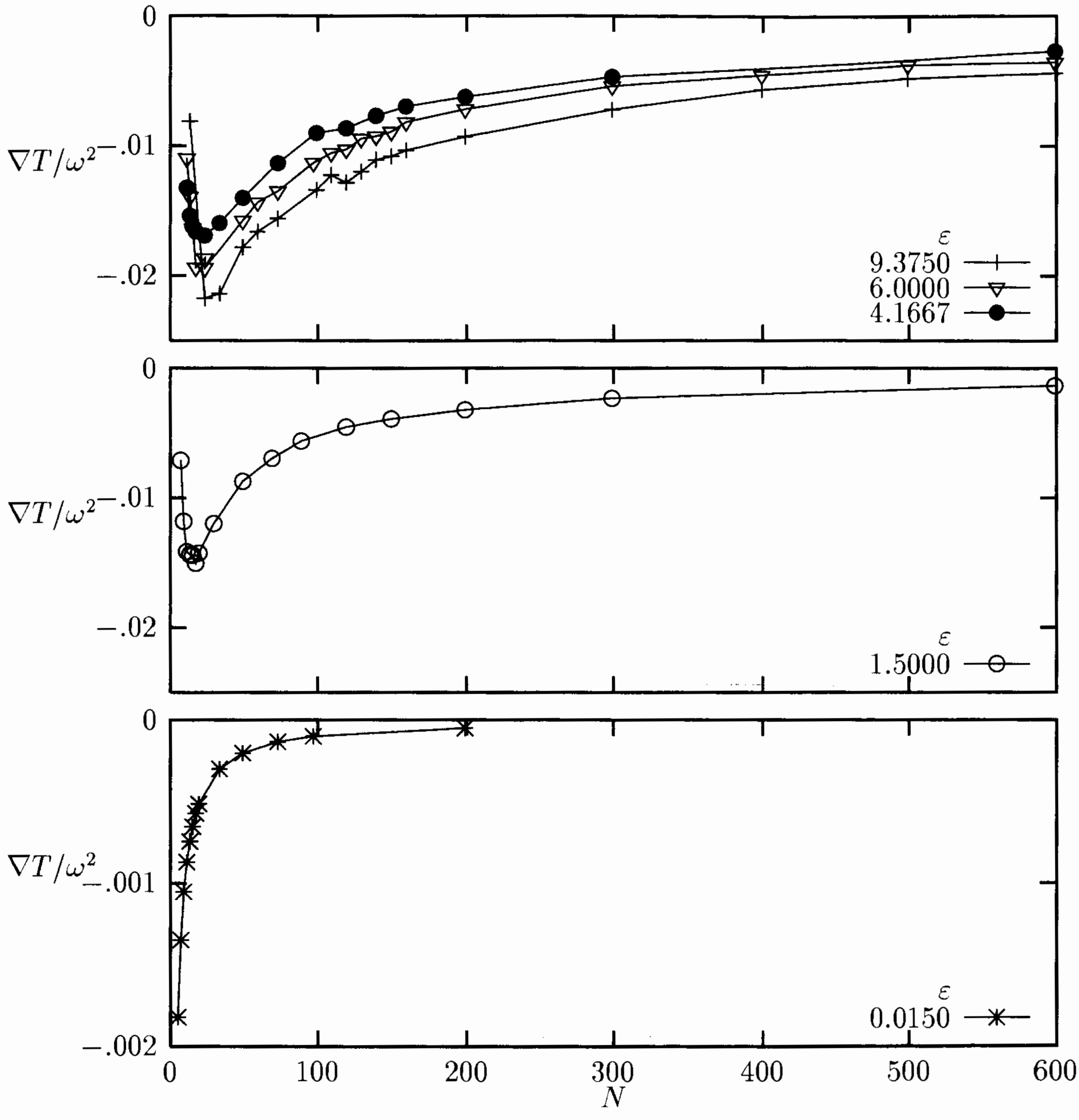

Figure 3.7: The temperature gradient for various numbers of particles N.

3.4 Calculation of $\mathcal{J}$

Compared to the calculation of ∇T, the calculation of the flux $\mathcal{J}$ encounters few complications. The flux is calculated for both sides and is only acceptable if the two values are within 1% of each other. As seen in Fig. 3.8, the flux decreases as the lattice size is increased. This is expected since, as we have seen, the gradient's magnitude will shrink as the lattice size is increased.

3.5 Comparison with CFVV

CFVV presented results for the thermal conductivity as a function of the chain length (their Fig. 3). We compared data from their plot with our own data for the equivalent value of ε and with the temperature of the left reservoir, T_{L}, set to 2.5 and the right, T_{R}, set to 1.5. Our data, Fig. 3.9, clearly agree with the results of CFVV. However, it is premature to conclude, as CFVV did, that this corresponds to the asymptotic limit of the thermal conductivity. In Fig. 3.10, we show that this is only a minimum and that bulk thermal conductivity cannot be said to have been observed until $N > 200$. The minimum is deepest for large energy densities and disappears entirely for very small density, as can be seen in Fig. 3.11.

CFVV also produced a table of k, J, and ∇T values for $\omega = 10$, which are also confirmed by our calculations.

	$N = 5$		$N = 9$	
	CFVV	our results	CFVV	our results
k	0.374 ± 0.008	0.373 ± 0.004	0.376 ± 0.022	0.361 ± 0.004
∇T	-0.180	-0.182 ± 0.001	-0.105	-0.105 ± 0.0005
$\langle J \rangle$	0.0672	0.0678 ± 0.0002	0.0396	0.0380 ± 0.0002

Table 3.1: Comparison of our values for k, ∇T, $\langle J \rangle$ with $N = 5, 9$ for $\omega = 10$ ($\varepsilon = 0.015$) and those presented by CFVV

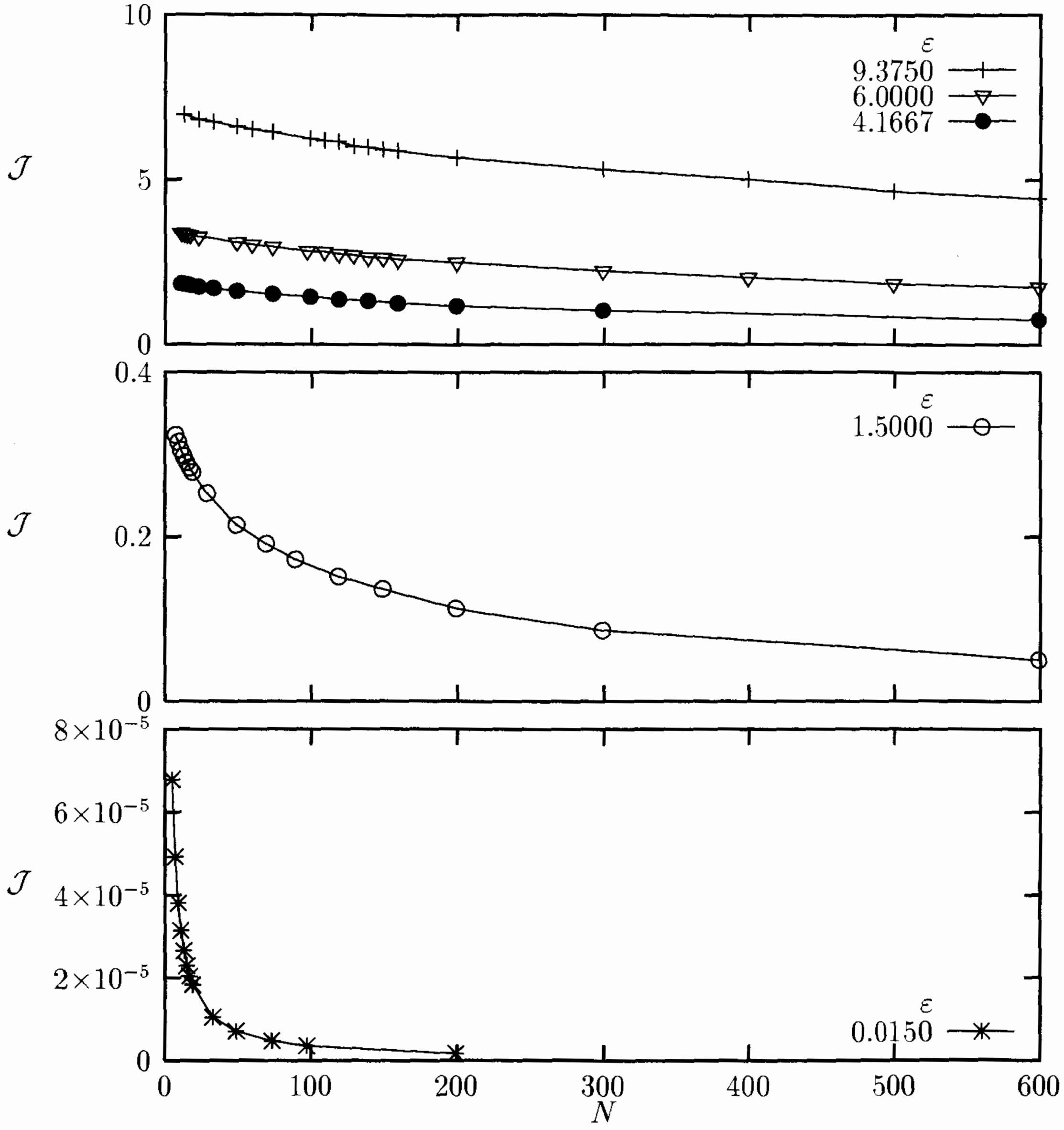

Figure 3.8: The flux for various numbers of particles N.

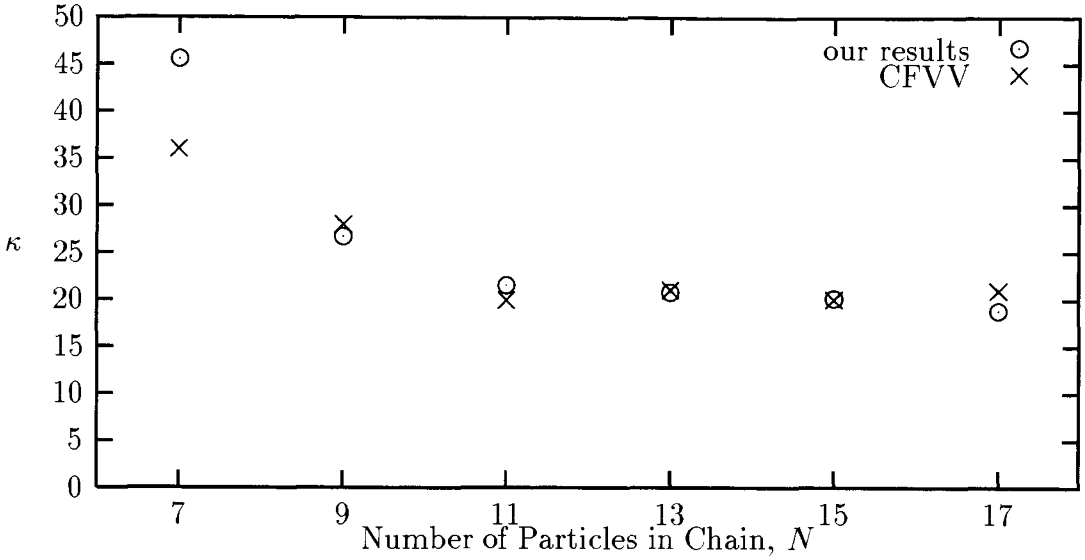

Figure 3.9: Comparison of thermal conductivity κ with the CFVV results for $\omega = 1$ ($\varepsilon = 1.5$).

3.6 Temperature dependence of k

If Fourier's law, $J = -k\nabla T$, is valid, we would expect that after initial transients have died out, there would be a uniform gradient of temperature along the chain. Fig. 3.12 shows that the local temperature (computed as twice the average kinetic energy of each particle) actually has a smooth nonlinear variation with position. We interpret the curvature as being due to the temperature dependence of the conductivity k. If k increases with T, then the decrease of $k(T)$ from left to right along the chain must be compensated by an increase in ∇T.

We have calculated $k(T)$ directly by varying the central temperature (Fig. 3.13). To ensure that the variation of $k(T)$ along the chain does not affect our results, we use a small temperature difference ΔT. In Fig. 3.13 we see results for chains of 9 and 31 particles with $\Delta T = 0.2$. The results are different from what one might expect for an anharmonic lattice. For example, the work of Maeda and Munakata [MM95] shows a different relationship for small T, $k(T) \propto T^{-\frac{1}{2}}$. This results because they

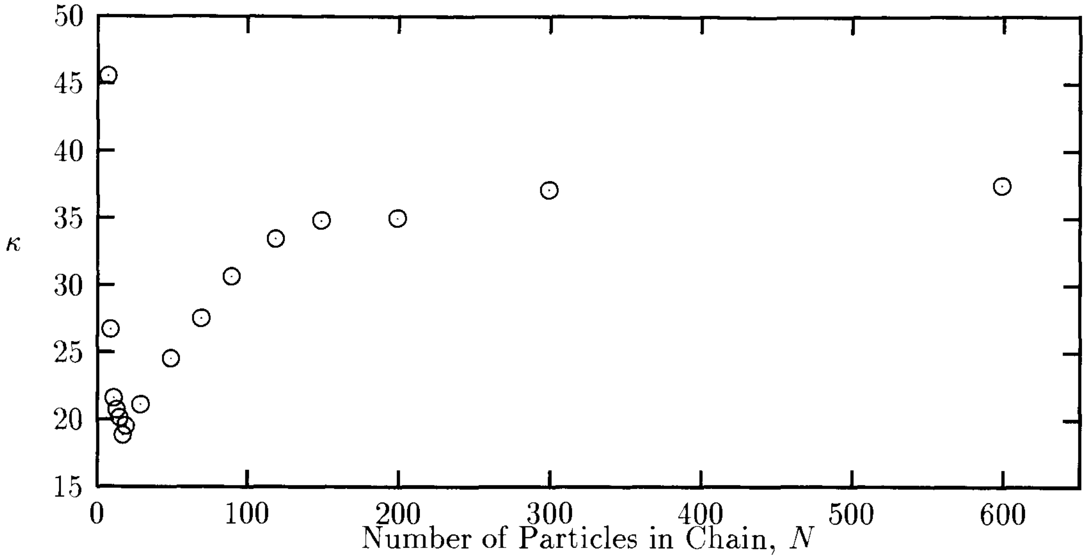

Figure 3.10: Thermal conductivity κ for $\omega = 1$ ($\varepsilon = 1.5$) with very large lattices.

were modeling the FPU β lattice (harmonic lattice with quartic anharmonicity). For small T, the anharmonic term will not contribute and one expects a divergent k for an integrable (harmonic) lattice. For the ding-a-ling lattice, as the energy is reduced, the bound particles are more tightly bound to their sites. Because this attenuates soliton-like energy transport, one does not expect k to diverge as $T \longrightarrow 0$. In fact, we see $k \longrightarrow 0$ in Fig. 3.13. On the other hand, the high-T regime should produce divergent k since, in this limit, the lattice behaves as free particles on a wire (an integrable system).

From Fig. 3.13, we see that the temperature dependance of κ between $T = 1.5$ and 2.5 is approximately linear, and we shall use this to predict the curvature of $T(x)$ in Fig. 3.12. Following a procedure described by Gebhart [Geb93], we approximate $k(T)$ as

$$k(T) = k_r + \beta(T - T_r), \tag{3.4}$$

where T_r is the temperature of the right-most ($i = N - 1$) particle used in the

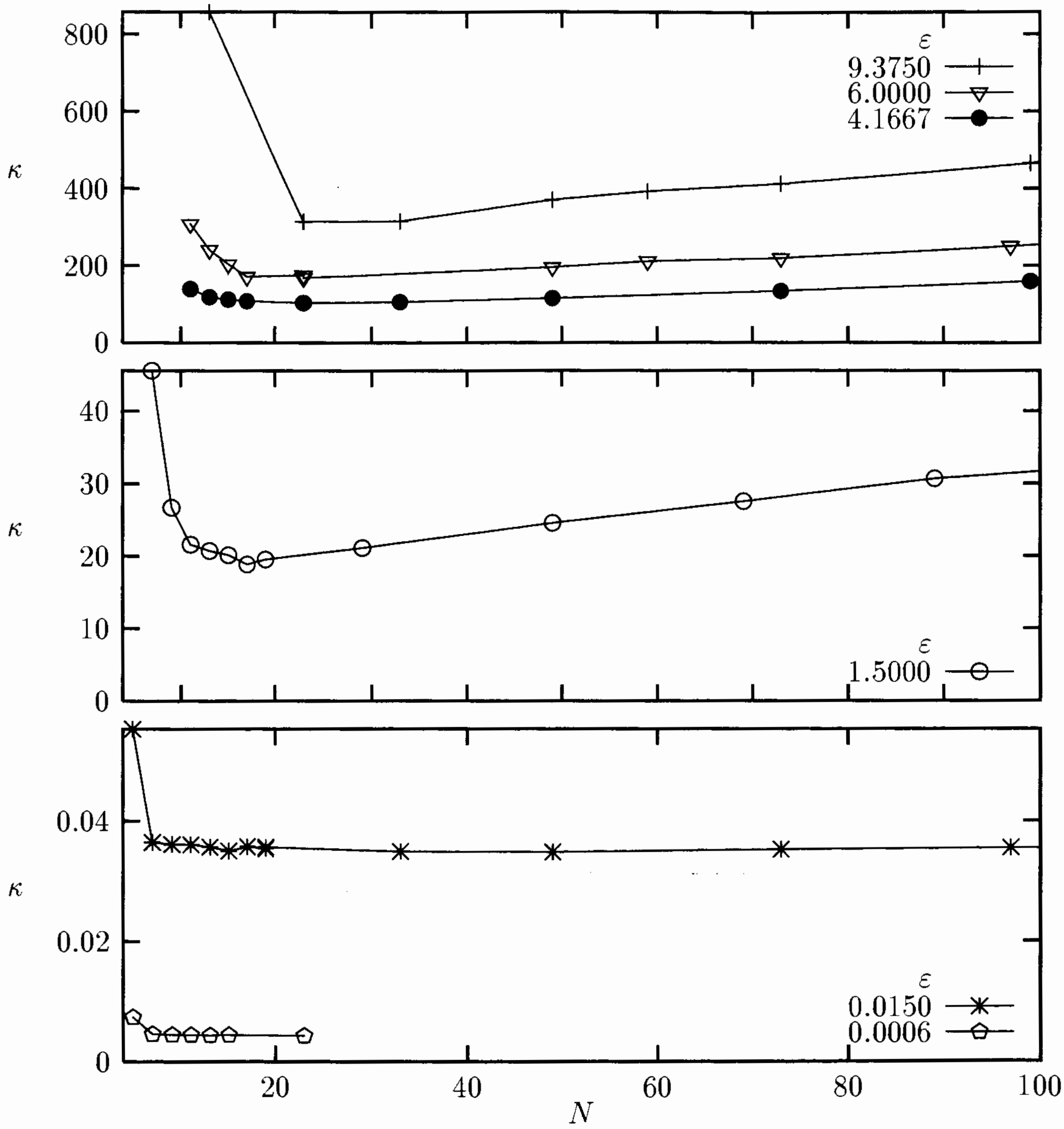

Figure 3.11: The thermal conductivity for various numbers of particles N.

calculation of k, and k_r is $k(T_r)$. From Fourier's law, we have

$$\int_{T_\ell}^{T} k(T')dT' = -\int_{2}^{x} J dx', \tag{3.5}$$

where the left-most ($i = 2$) particle involved has a temperature T_ℓ. Since J is constant along the lattice, we have

$$-\int_{2}^{x} J dx' = -J(x-2) \tag{3.6}$$

and using Eq. (3.4) we get

$$\int_{T_\ell}^{T} k(T')dT' = \left(k_r T' + \beta\left(\frac{T'^2}{2} - T_r T'\right)\right)\Bigg|_{T_\ell}^{T}. \tag{3.7}$$

We now use these two equations to solve for $T(x)$,

$$T(x) = -\gamma \pm \left[\gamma^2 - 2\left(\frac{J}{\beta}(x-2) - \frac{k_r T_\ell}{\beta} - \left(\frac{T_\ell^2}{2} - T_r T_\ell\right)\right)\right]^{\frac{1}{2}}, \tag{3.8}$$

where γ is $k_r/\beta - T_r$. Notice that the fit for T is exact for $x = 2$ (the left end), while k is exact for $T = T_r$ (the right end).

The temperature profile data of Fig. 3.12 was fitted to the formula (3.8), using β as the only adjustable parameter. The nonlinear least-square fit yields the value $\beta = 3.0$. This may be compared to the slope of the $k(T)$ curve in Fig. 3.13 at the central temperature $T_{\mathrm{m}} = 2$, which yields $\beta = 2.8$. The agreement between the two independent determinations of β is satisfactory.

3.7 Effect of shrinking ΔT

In order to measure the effect of shrinking ΔT, we tried reducing the applied temperature difference. For this calculation, we used all but the end particles in the calculation of ∇T, instead of only using the 60% as we typically do. This is thus a worst case. Using very small ΔT incurred a greatly increased convergence time and was only practical for short lattices. In any case, the κ extrapolated to $\Delta T = 0$ is not appreciably different from that calculated for $\Delta T = 1$ (the value we use in most of our calculation), as we can see from Fig. 3.14. The fitting form of a constant term plus a

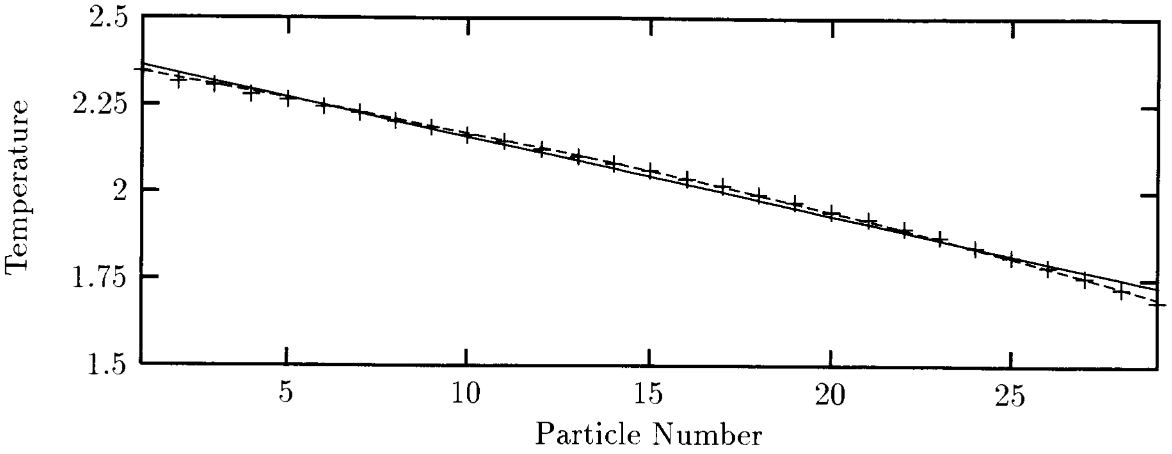

Figure 3.12: Temperature profile with $\omega = 2$. The solid line is a linear fit through the data; the dashed line is a fit using Eq. (3.8) with β the only variable parameter.

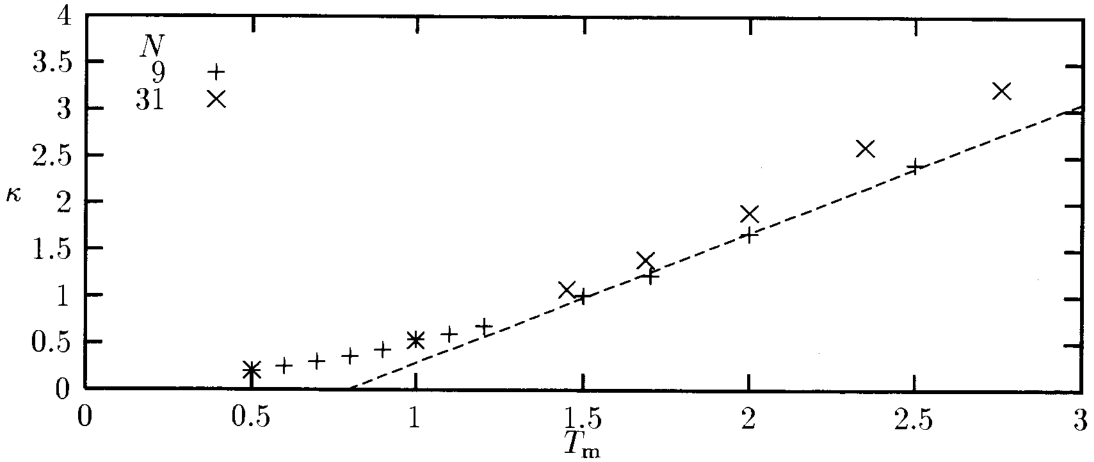

Figure 3.13: The value of κ as a function of T, for $\omega = 2$ and chain lengths of 9 and 31 particles with $\Delta T = .2$. The dashed line is a linear fit through the points between 1.5 and 2.5 for $N = 9$.

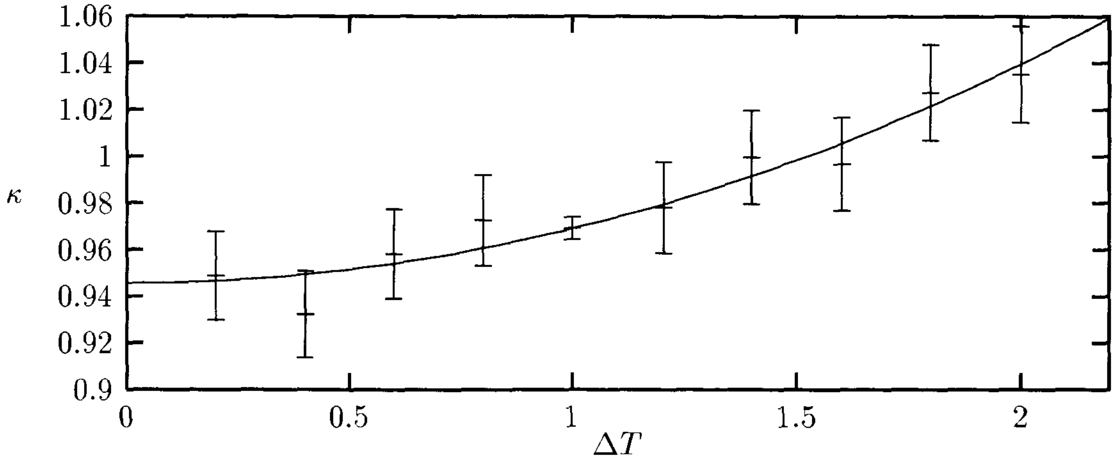

Figure 3.14: κ for various ΔT with central temperature of 2, spring constant $\omega = 2$ ($\varepsilon = .375$) and chain of $N = 31$ particles.

quadratic was used because κ should be even in ∇T. (A linear fit was also calculated for comparison but produced larger residuals.) The deviation seen for large ΔT can be attributed to both the temperature dependence of κ and correction to Fourier's law.

3.8 Long-Chain Limit

In addition to confirming the results of CFVV, we wish to determine the range of parameters, ε and N, over which Fourier's law applies. Although Fig. 3.10 shows clearly that a constant value of κ has been reached in this case, it is more effective to plot the thermal resistivity, $\rho = 1/\kappa$, as a function of $N^{-\frac{1}{2}}$. We use $N^{-\frac{1}{2}}$ rather than $1/N$ as the variable because it yields a good linear fit for large N (see Fig. 3.15 to 3.18). The linear function

$$\rho(N) = \mu N^{-\frac{1}{2}} + \rho_\infty, \tag{3.9}$$

is thus used to describe our large-N resistivity data. A positive intercept of the ρ axis ($\rho_\infty > 0$) for $N^{-\frac{1}{2}} \rightarrow 0$ implies that the conductivity has a finite limit for arbitrarily long chains. A zero intercept implies that κ diverges as $N \rightarrow \infty$, and so Fourier's law would not apply. A negative intercept would imply that κ diverges for some finite N. In fact, however, the appearance of a negative intercept in Fig. 3.15 merely means that the data are insufficient to resolve an intercept very close to zero.

Although we have no explanation for the $N^{\frac{1}{2}}$ dependence, Toda [Tod79] has predicted $N^{\frac{1}{2}}$ behaviour for an isotopicly disordered lattice. He found $\kappa \sim N^{\frac{1}{2}}$ for free boundaries and $\kappa \sim N^{-\frac{1}{2}}$ for fixed boundaries. However, his analysis involved localization of normal modes, which is not relavent to the ding-a-ling model.

The plots of resistivity, Fig. 3.15 to 3.18, give a fairly complete picture of the behaviour as we vary ε. Fig. 3.15 shows the weak-spring limit, in which we might expect Fourier's law to break down. These data demonstrate the limit of our numerical capabilities, since we would need to calculate κ for much longer lattices in order to resolve whether the intercept is positive or negative. In Fig. 3.16 and 3.17 we can say with confidence that, for these values of ε, we have a positive intercept. We can also see a very distinct maximum in ρ, for some values of ε, which corresponds to the minima in Fig. 3.11. The maxima have disappeared in Fig. 3.18.

The intercepts in Fig. 3.15 to 3.18 tell us how the conductivity behaves for an infinite lattice, so it is useful to plot it as a function of ε, as in Fig. 3.19. (We have not included the intercepts from Fig. 3.15 since they are not accurate enough.) We can see quite clearly the change in behaviour from small ε (stiff springs) to large ε (weak springs). The power-law variation in ρ_∞ for $\varepsilon > \varepsilon_c$ implies that infinite conductivity should occur only in the limit of vanishing spring constant, which is the integrable limit of the free particle hard point gas. We introduce $\varepsilon_c = 0.04$ at this point, since it functions well as a benchmark for the breakdown of the stiff-spring limit. Its value is derived from the scaling properties of the Lyapunov exponent and is discussed fully in Sect. 4.6. We will put a vertical bar in our plot at ε_c to distinguish the two regimes, stiff and weak spring.

The slope μ changes sign, with $\mu \lesssim 0$ for $\varepsilon \lesssim \varepsilon_c$. If we rewrite Eq. (3.9) in a normalized form,

$$\bar{\rho}(N) = \bar{\mu}N^{-\frac{1}{2}} + 1, \tag{3.10}$$

where $\bar{\rho} = \rho/\rho_\infty$ and $\bar{\mu} = \mu/\rho_\infty$. For $\bar{\rho}(N)$ to be within some δ of 1, we must take $N > N_\delta$, where

$$N_\delta = \left(\frac{\bar{\mu}}{\delta}\right)^2. \tag{3.11}$$

Fig. 3.20 shows that as ε increases, for $\varepsilon > \varepsilon_c$, we need increasingly larger lattices to approximate the asymptotic limit; however, for $\varepsilon < \varepsilon_c$ only short lattices are needed, and N_δ is not strongly dependent on ε. A dashed line is used in Fig. 3.20 to emphasize that the slope does go through zero and show the dominant features. Fourier's law is always obeyed provided the lattices are long enough.

3.9 Stiff-Spring Limit

It is possible to deduce the value of the thermal conductivity by means of a simple argument, which should be valid in the limit of very stiff springs on the bound particles. We assume that each bound particle behaves as a harmonic oscillator with a Maxwellian velocity distribution governed by the local temperature. A free particle bounces back and forth between two bound particles. At each elastic collision it exchanges velocities with the bound particle, and so on average it carries energy from the higher to the lower temperature side.

Let v_+ be the speed of a free particle traveling in the positive direction (down the temperature gradient), and v_- be its speed of return in the negative direction. The contribution to the energy flux from this round trip will be equal to the difference between the energies carried in the two directions divided by the time for the round trip,

$$J = \frac{\frac{1}{2}v_+^2 - \frac{1}{2}v_-^2}{\frac{2}{v_+} + \frac{2}{v_-}} \tag{3.12}$$

The factor of 2 in the denominator comes from the distance between the bound particles, which is 2 lattice units.

We can estimate the conductivity if we replace the velocities in Eq. (3.12) by their rms averages $\bar{v}$, which are related to the temperature by equipartition, $\frac{1}{2}\bar{v}^2 = \frac{1}{2}T$

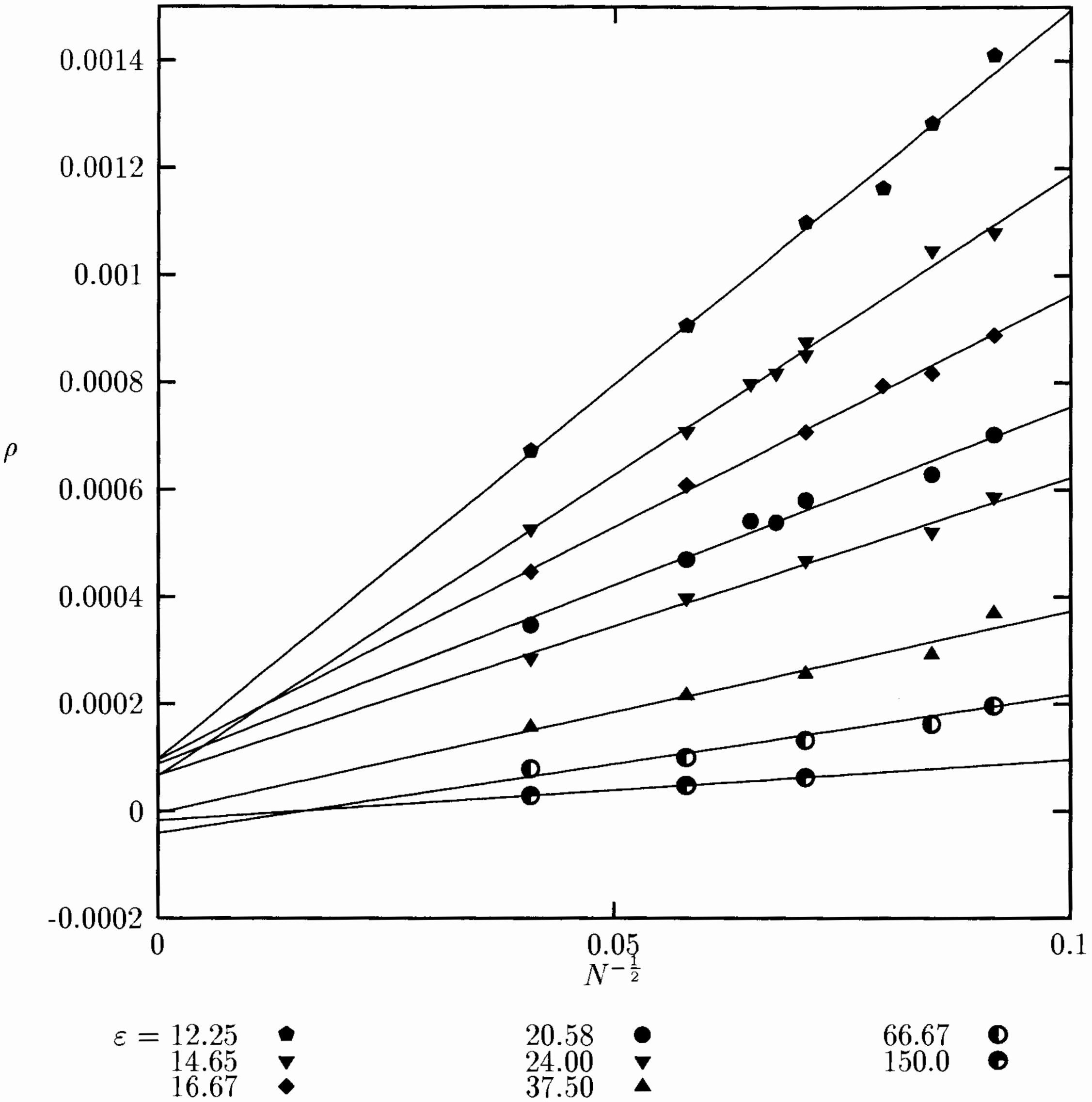

Figure 3.15: Resistivity for long chains and large ε. The solid line is a least-squares fit for $N^{-\frac{1}{2}} < 0.12$.

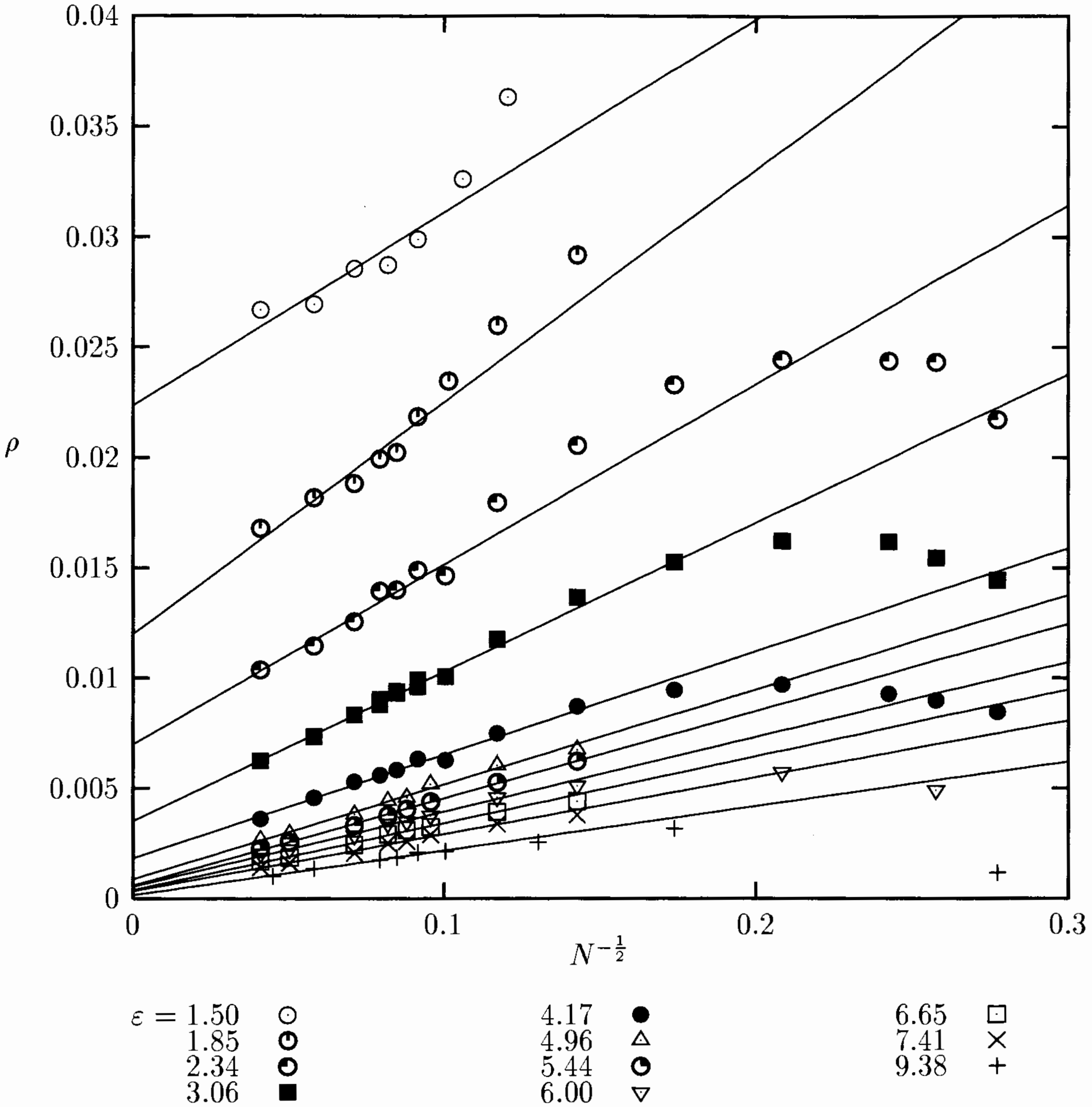

Figure 3.16: Resistivity for long chains and medium ε. Only every second data point is displayed for $\varepsilon > 4.5$ to make the graph more readable. The solid line is a least-squares fit for $N^{-\frac{1}{2}} < 0.12$.

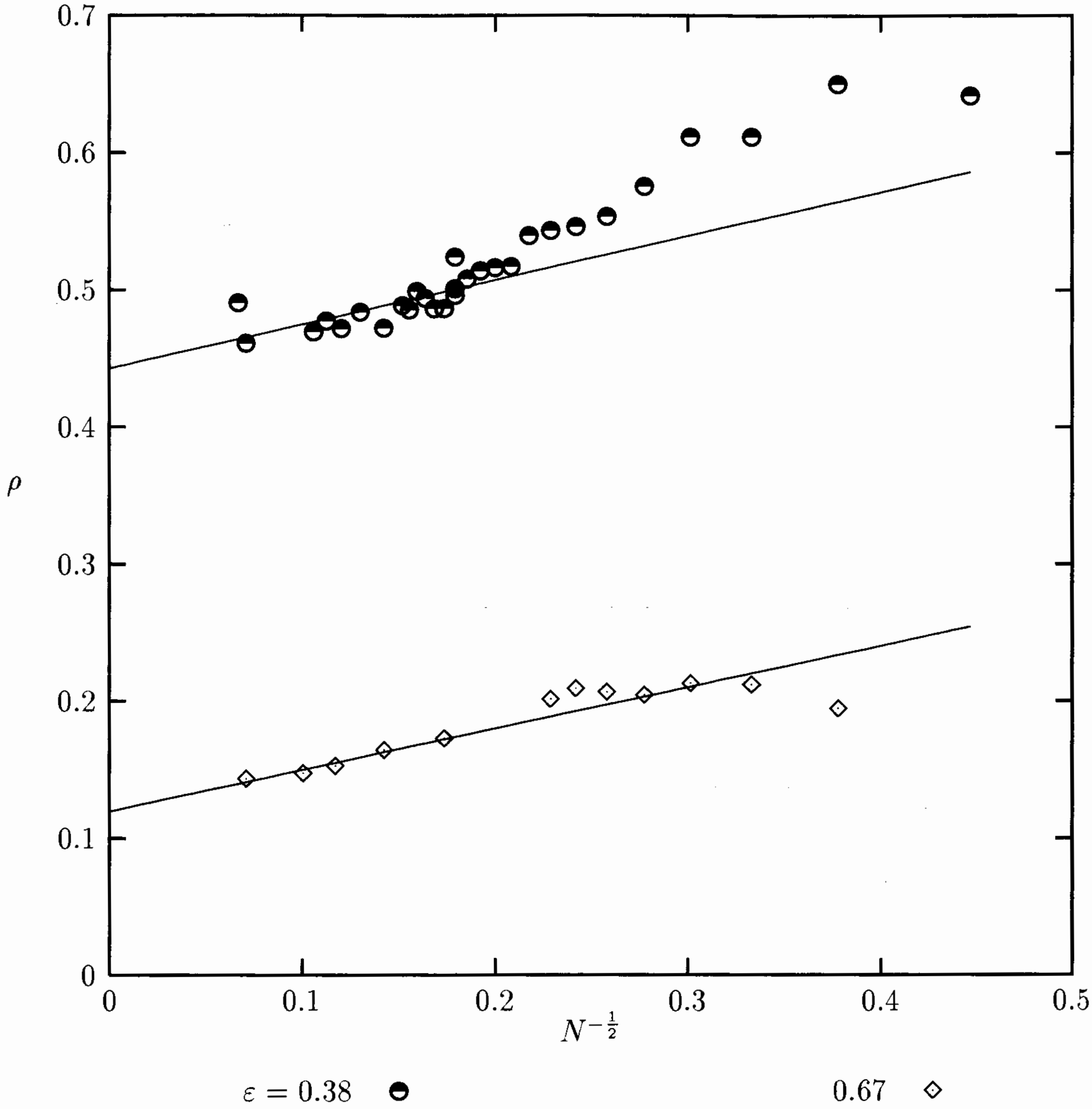

Figure 3.17: Resistivity for long chains and small ε. The solid line is a least-squares fit for $N^{-\frac{1}{2}} < 0.20$.

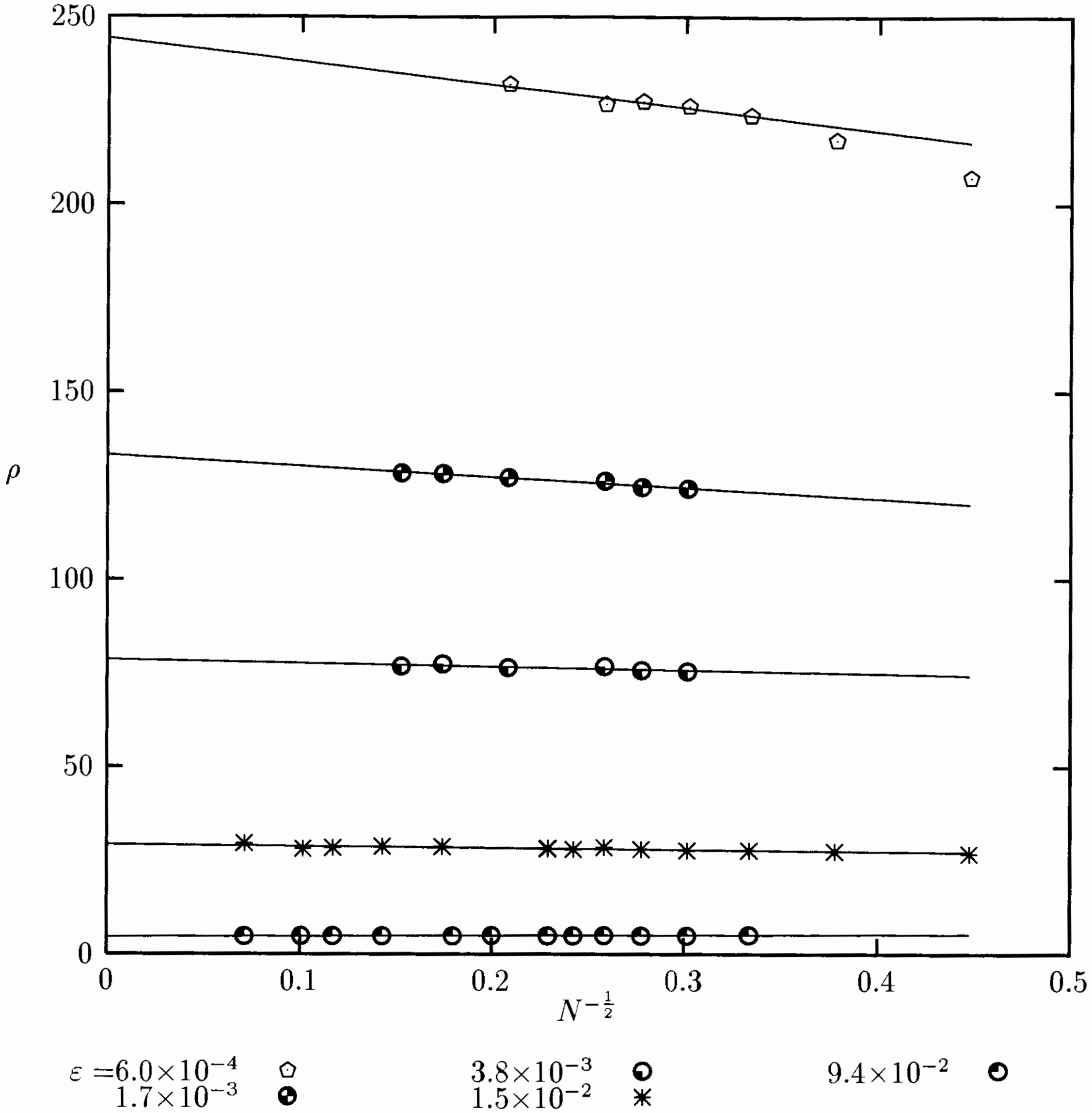

Figure 3.18: Resistivity for long chains and very small ε. The solid line is a least-squares fit for $N^{-\frac{1}{2}} < 0.32$.

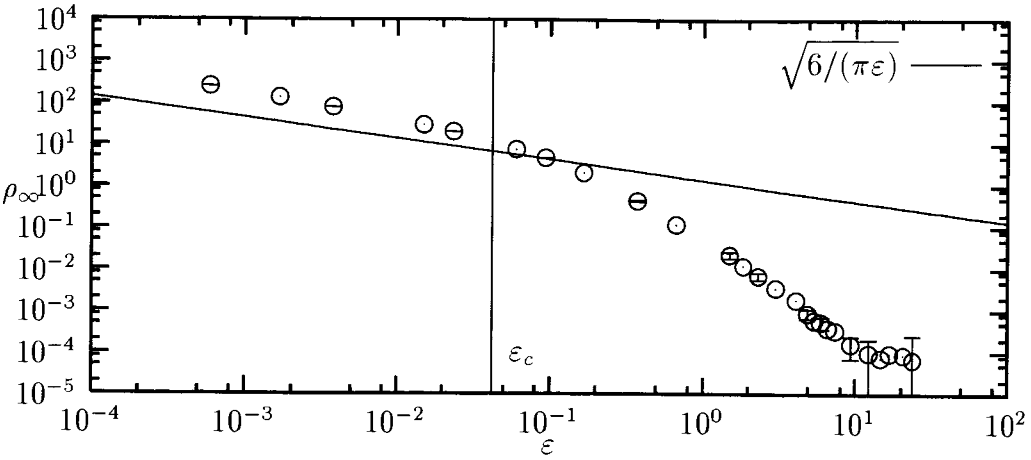

Figure 3.19: Resistivity for infinite chains (the intercept in Fig. 3.16 to 3.18). The solid line is the analytic result from Eq. (3.21)

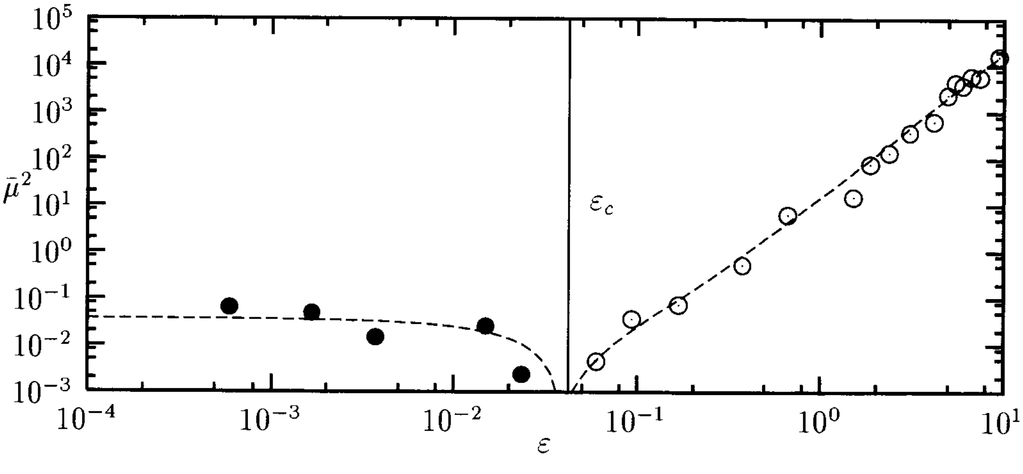

Figure 3.20: The square of the normalized slope in Eq. (3.10). The open circles correspond to a positive slope while the filled circles correspond to a negative slope. The dashed line is used to guide the eye only.

(Boltzmann's constant has been set to unity). Writing the temperature of the left and right bound particles as $T_+ = T - \nabla T$ and $T_- = T + \nabla T$ and neglecting the difference between v_+ and v_- in the denominator, we obtain $J = -\nabla T/(2T^{-\frac{1}{2}})$, whence the conductivity becomes

$$k = -\frac{J}{\nabla T} = \sqrt{\frac{T}{2}}. \tag{3.13}$$

In terms of our dimensionless parameters, $\kappa = k/\omega$ and $\varepsilon = 3T/4\omega^2$, this becomes

$$\kappa = \sqrt{2\varepsilon/3}. \tag{3.14}$$

A better approximation is obtained if we average the energy current J in Eq. (3.12) over the distributions of v_+ and v_-. The appropriate distribution, $P_T(v)$, is the probability that a free particle will transit at speed v between two bound particles. The Boltzmann distribution, which is the probability that a randomly selected particle will have instantaneous velocity v, differs from $P_T(v)$ by a factor proportional to the transit time (v^{-1}). Hence, the appropriate distribution is

$$P_T(v) = \frac{|v|}{T} e^{(-v^2/2T)}. \tag{3.15}$$

Upon simplifying Eq. (3.12), we obtain the average energy current

$$\langle J \rangle = \frac{1}{4}[\langle v_+^2 \rangle \langle v_- \rangle - \langle v_+ \rangle \langle v_-^2 \rangle], \tag{3.16}$$

where the distributions for v_+ and v_- are given by Eq. (3.15) with temperatures T_+ and T_-, respectively. The calculation of the averages in Eq. (3.16) are

$$\langle v^2 \rangle = 2T, \tag{3.17}$$

$$\langle v \rangle = \sqrt{\frac{\pi T}{2}}, \tag{3.18}$$

so we have

$$J = \sqrt{\frac{\pi}{8}} \left[T_+ T_-^{\frac{1}{2}} - T_+^{\frac{1}{2}} T_- \right]. \tag{3.19}$$

If we now expand J in a Taylor series in ∇T, we have

$$J = -\sqrt{\frac{\pi T}{8}} \nabla T. \tag{3.20}$$

This results in an approximate value for the conductivity of $k = \sqrt{\pi T/8}$ or in dimensionless variables

$$\kappa = \sqrt{\frac{\pi}{6}\varepsilon}. \tag{3.21}$$

These are compared to the results of the numerical simulations in Fig. 3.19. One can see approximate agreement with the slope corresponding to the exponent of $\frac{1}{2}$ in Eq. (3.21).

The essential assumption in this simple argument is the neglect of correlations among the particles. This assumption becomes more reasonable in the stiff limit, when the bound particles oscillate very rapidly compared to the motion of the free particles. But the systematic difference between Eq. (3.21) and the numerical results in Fig. 3.19 indicates that correlation effects are not entirely negligible, even in that limit.

Chapter 4

Analysis of the Dynamics

In order to demonstrate the role of chaos in establishing Fourier's law of heat conduction, we need to study a system that has both an integrable and a non-integrable limit. The ding-a-ling model becomes integrable in the zero spring-constant limit. As the spring stiffness increases, the dynamics becomes more chaotic. We wish to observe the transition between two such regimes and to correlate the dynamics with the behaviour of the thermal conductivity. The transition between the two regimes is continuous rather than sharp; but, evidence for it can be found in many different aspects of the dynamics.

4.1 Particle Paths

The ding-a-ling model was expected to support a Fourier law conductivity because the energy transport via soliton-like pulses should be suppressed by the phase randomization caused by the oscillating bound particles. In Fig. 4.1, we see the displacement of particles as a function of time, with the "left" and the "right" labels on the y-axis marking the position of the corresponding reservoirs and the tics marking the lattice sites.

Particle trajectories cannot cross each other. They merely exchange velocities in elastic collisions. The apparently smooth lines, in Fig. 4.1(a), from one end of the lattice to the other, represent the transmission of energy without its being scattered or diffused. These soliton-like pulses are typical of the weak-spring limit. As the spring constant increases, the trajectories of the bound particles become more curved, as is shown in Fig. 4.1(b). This causes the soliton-like pulses to propagate along curved paths in the space-time diagram. Sometimes the spatial direction of propagation is reversed, corresponding to the reflection of soliton-like pulses. Energy from the pulse is exchanged with the potential energy of the springs, making soliton-like pulses less effective as a mechanism of energy transport. In the stiff-spring limit, Fig. 4.1(c), the pulses are effectively destroyed and diffusive energy transport is dominant. The transition between the dominant energy transport mechanism being soliton-like pulses or diffusion will clearly depend on the length of the lattice. The weaker the spring, the longer must the lattice be in order for energy diffusion to dominate. This is consistent with the results of Fig. 3.15-3.18 and Fig. 3.20, which show that, as the spring becomes weaker, longer lattices are needed to approximate the bulk conductivity limit.

4.2 Path Length of Soliton-like Pulses

Solitons were originally found by Zabusky and Kruskal [ZK65] in a variation of the FPU model. This was a continuum limit of the FPU lattice that described a partial differential equation with solutions that were localized disturbances that retained their shape and energy on collision. While there is no continuum limit of the ding-a-ling model to provide partial differential equations with such solutions, in Fig. 4.1(a) we see what appear to be particle-like disturbances that travel, undeviated, across the lattice. Their apparent constant velocity (hence constant kinetic energy) is the main reason for the association with the soliton concept. Also, they are localized, existing precisely at the location of the corresponding particle. Energy transport via pure solitons generates a flux proportional to the temperature difference rather than the temperature gradient since it is independent of lattice length. Hence, they cause deviations from Fourier-law behaviour.

From the description of the particle trajectories in Sect. 4.1, we can see how the soliton-like pulses can propagate energy in the lattice and how the exchange of potential and kinetic energy while traveling as a bound particle alters their kinetic

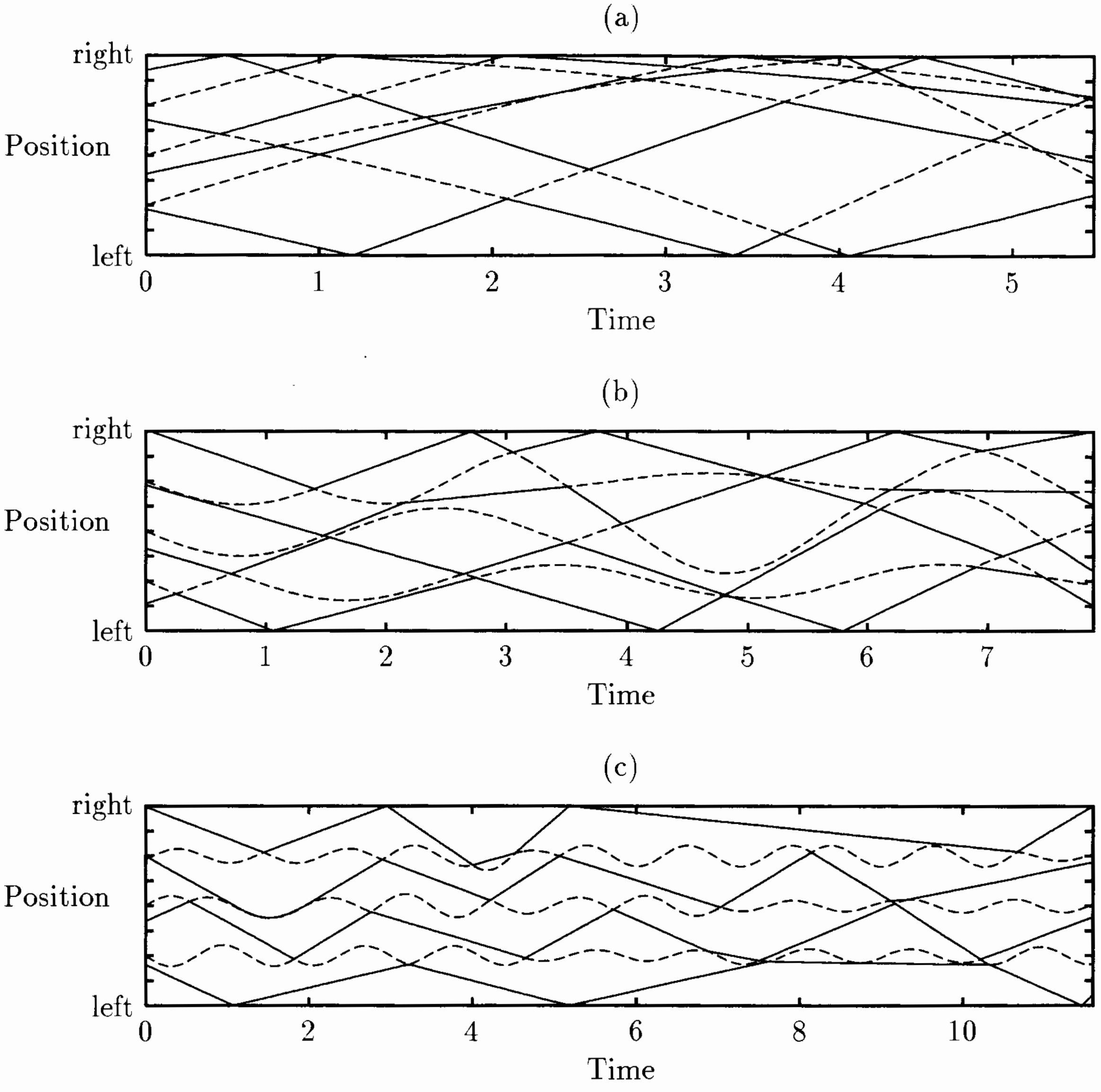

Figure 4.1: Lattice dynamics for a 7 particle chain with different ω: (a)$\omega = 0.5$ ($\varepsilon = 6.0$) (b)$\omega = 2$ ($\varepsilon = .375$) (c)$\omega = 5$ ($\varepsilon = .06$). The solid lines represent the paths of the free particles while the dashed lines represent the bound particles.

energy. If we monitor the kinetic energy from when it leaves the reservoir, as it is passed from free to bound particles and from bound to free particles, we can measure the decay of these energy carriers. In Fig. 4.1(b), we can see that some of these soliton-like pulses do not reach the opposite reservoir; instead, they reverse their direction. A soliton-like pulse that has reversed can be considered terminated, since it is not carrying energy from one reservoir to the other. This termination distance is the path length of the soliton-like pulse. These reversals can only occur when the particle carrying the soliton is a bound particle. The path length is, thus, measured relative to the lattice site of the first bound particle in the chain. The distribution of these path lengths for a number of different ε is displayed in Fig. 4.2. Each curve is normalized so that the area under the curve is equal to 1. In Fig. 4.3 we have replotted Fig. 4.2 on a semi-log scale (to emphasize the exponential decay) using the unnormalized bin counts of the histogram.

These figures were constructed by allowing an open system to evolve (in the same way used to calculate the thermal conductivity with $T_{\mathrm{L}} = 2.5, T_{\mathrm{R}} = 1.5$, and $N = 299$ for 10^5 collisions per particle), while monitoring the decay of the soliton-like pulses. These decay lengths were assigned to bins to form a histogram. The histogram has a bin width of 2 lattice spacings, since the free particles cannot terminate a soliton-like pulse.

In general, the distributions decay exponentially; however, for large ε, we see that a maximum is reached, followed by this exponential decay. In the weak-spring limit, we also see very long tails, indicating that a significant fraction of the energy transport can be attributed to these pulses, even for reasonably large lattices.

The average value of the path lengths was calculated. This mean-free-path length, Λ, is a good indicator of how effective the pulses are for a given ε. In Fig. 4.4, we see that Λ increases monotonically, with ε obeying a power law in the two regions separated by ε_c. Because the pulses can only terminate when the bound particle extends to its amplitude, it is reasonable to assume that Λ is related to the amplitude A of an oscillator having the energy of the reservoir that created the pulse. In the stiff-spring limit, we can make a rough estimate of this dependence on A by assuming that the pulses go no farther than the second bound particle. We will then have pulses that suffer one collision and thus have an average path length of A, as well as those that suffer two collisions and thus have an average path length of $2 + A$. The mean free path will be calculated from the contributions of both

$$\Lambda = P_1 A + P_2(2 + A) \tag{4.1}$$

where P_1 is the probability of suffering one collision before terminating and P_2 is the probability of suffering two. To calculate the probabilities P_i we assume that if the free particle is within A of the bound particle it will collide so as to allow the pulse to travel to the second bound particle. Otherwise the pulse will terminate after the first collision. From Fig. 2.2(b) we see that in this stiff-spring limit the probability distribution is approximately uniform between the bound particles (a total width of 2). So we estimate that the probability of this occurring is $A/2$; this implies

$$\begin{aligned} P_1 &= 1 - A/2 && (4.2) \\ P_2 &= A/2. && (4.3) \end{aligned}$$

Using this with Eq. (4.1) and simplifying we have

$$\Lambda = 2A. \tag{4.4}$$

We now need to express this in terms of ε. From equipartition, we have $E = T_{\mathrm{L}}$ (T_{L} is the temperature of the left reservoir). Since the energy of the oscillator is $A^2\omega^2/2$ we have

$$A = \sqrt{2T_{\mathrm{L}}}/\omega = \sqrt{\frac{8\varepsilon T_{\mathrm{L}}}{3T_{\mathrm{m}}}}, \tag{4.5}$$

where we have used Eq. (2.2) to express the amplitude in terms of ε. For $T_{\mathrm{L}} = 2.5$ and $T_{\mathrm{m}} = 2$, we have $\Lambda = 2\sqrt{10\varepsilon/3}$, which has been plotted in Fig. 4.4. This is only an estimate of the lower bound on Λ (since we neglect pulses that suffer more than 2 collisions) but is a good approximation in for $\varepsilon < \varepsilon_c$.

In the weak-spring limit, we can also make a rough estimate of the functional form of Λ. From Fig. 2.2, we see that, in this limit, the position distributions are approximately Gaussians of equal width. The most probable position for the particles of the lattice is their respective lattice sites. If we then try to model a typical soliton-like trajectory, we could start by saying that the collisions all occur at the lattice sites. We need not restrict the velocities of these particles as long as this is so. To start this model pulse off, the free particle farthest to the left has just left the reservoir with a velocity corresponding to a temperature of T_L. While traveling as a bound particle, this pulse will exchange kinetic energy for the particle's potential energy. After each collision, an energy of $\frac{1}{2}\omega^2\Delta x$ is lost to soliton-like pulse. Given the initial conditions we will always have $\Delta x = 1$ and so the loss of energy is $\frac{1}{2}\omega^2$. Since its initial energy is $\frac{1}{2}T_\mathrm{L}$, the pulse can suffer only $(\frac{1}{2}T_\mathrm{L})/(\frac{1}{2}\omega^2)$ such collisions before it exhausts its energy. Since these types of collisions are 2 lattice sites apart, we have an estimate of this weak-spring mean free path length

$$\Lambda = \frac{2T_\mathrm{L}}{\omega^2} = \frac{8T_\mathrm{L}\varepsilon}{3T_\mathrm{m}}, \tag{4.6}$$

where we have again used Eq. (2.2) to express the amplitude in terms of ε. For $T_\mathrm{L} = 2.5$ and $T_\mathrm{m} = 2$, we have $\Lambda = 10\varepsilon/3$ which has also been plotted in Fig. 4.4. To estimate the error associated with deviations from the initial conditions, consider the effect of the displacement of a bound particle by some small $\pm\delta x$ from its lattice site. The amount of energy lost by the subsequent collision with the neighbouring free particle (on its lattice site) will be $\frac{1}{2}\omega^2(1-\delta x)$. On the other hand, if this bound particle were to start on its lattice site and collide with a free particle displaced by $\pm\delta x$, the energy loss would be $\frac{1}{2}\omega^2(1\pm\delta x)$. Thus, the symmetry in the position distributions ensures that the deviations in the initial positions of the free particles have no net effect; however, the deviations in the initial positions of the bound particles do tend to always decrease the amount of energy lost. As a result, Eq. (4.6) is an underestimate of the mean free path. While the underestimate in Fig. 4.4 appears quite large, the power of the ε dependence seems to be accurate. Indeed, a fit of the data for $\varepsilon > 1$ estimates that power as 0.94 rather than the 1 in Eq. (4.6).

From the study of the path lengths of the soliton-like pulses, we see that in the stiff-spring limit, they are suppressed. The mean free path can be accurately predicted by considering only two collisions in this limit and is proportional to $\sqrt{\varepsilon}$. Λ can also be shown to be linearly dependent on ε in the weak-spring limit. The division between these two regimes occurs at approximately $\varepsilon = \varepsilon_c$.

4.3 Phase Space

For any system to be a good candidate for a demonstration of the role chaos plays in its ability to support a temperature gradient and obey Fourier's Law, that system should have both an integrable and a non-integrable limit. In the ding-a-ling model when the spring constant goes to zero, we have the integrable free particle gas and, as we increase the spring constant, we expect increasingly chaotic dynamics. The best way to see this is with a Poincaré section of the phase space for the two particle periodic lattice. In Fig. 4.5 we have used the following coordinate system:

$$\begin{aligned} q_1 &= (x_2 - x_1 + 1)/\sqrt{2} \\ q_2 &= (x_2 + x_1 + 1)/\sqrt{2} \\ p_1 &= (v_2 - v_1)/\sqrt{2} \\ p_2 &= (v_2 + v_1)/\sqrt{2} \end{aligned} \tag{4.7}$$

and we use a section such that $q_1 = 0$ (at a collision) and $p_1 > 0$. Note, we have plotted only the upper half of the phase space, since by symmetry the lower half is identical.

Poincaré sections give a strong visual indication of the chaoticity of the phase space. In Fig. 4.5(a), we see the KAM tori circling a fixed point in the surface of sections. The destruction of this fixed point, with increasing ε, is an indication of the transition between two dynamical regimes.

From Fig. 4.5(a), we know that the main fixed point has $p_2 = 0$, so the velocity of the bound particle is equal to the negative of the velocity of the free particle and the section is such that the particles have just collided. The sign of the relative velocities, as defined for a section with $p_1 > 0$, is such that the particles would collide on the right of the loop, as in Fig. 4.6(c). After colliding, they exchange velocities and swing around toward the left. By symmetry, the particles must both be on their lattice sites at some intermediate time, as in Fig. 4.6(b). Proceeding to the left, the particles collide again, Fig. 4.6(a) and retrace their paths back to the state described

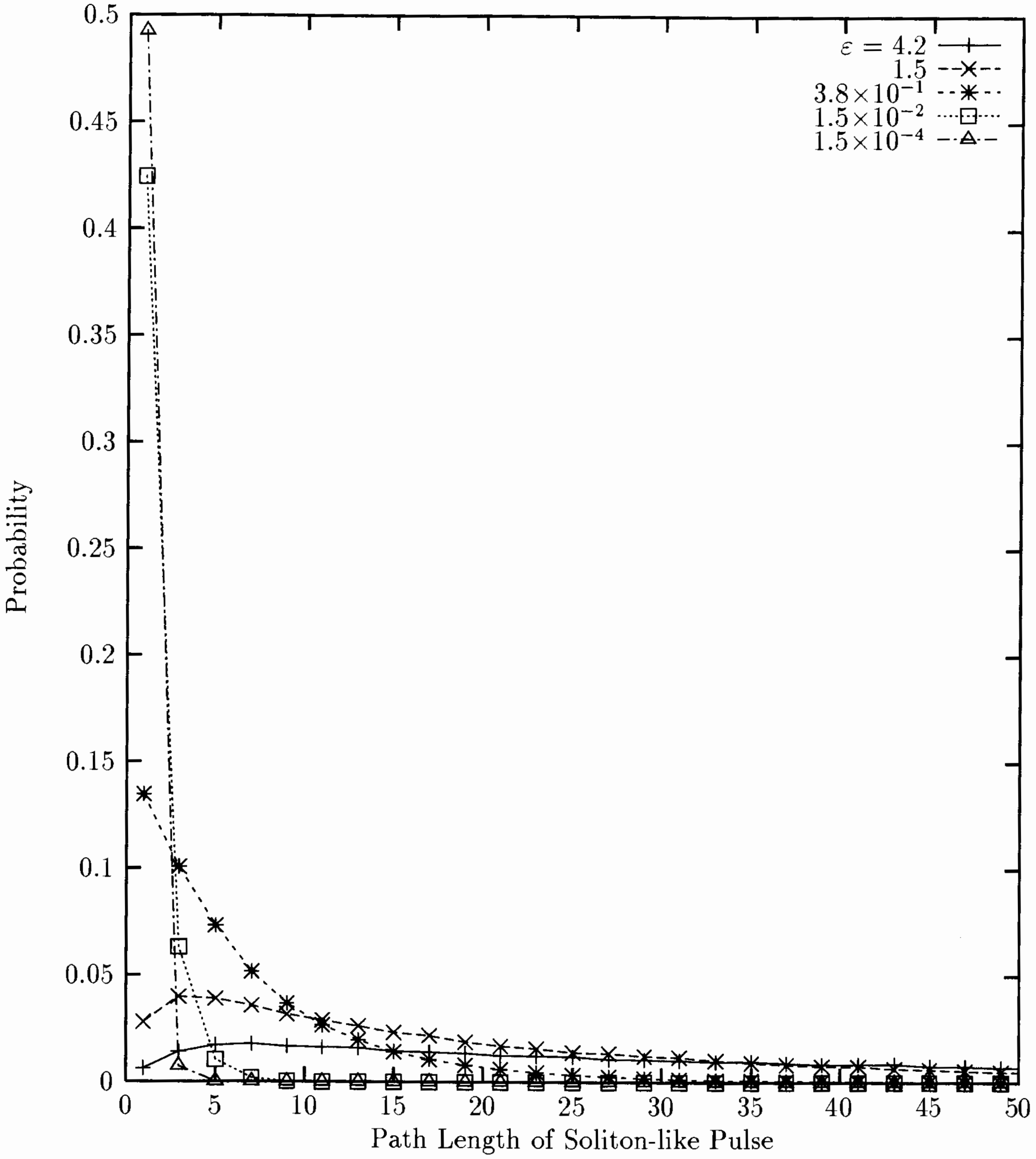

Figure 4.2: Distribution of path lengths for soliton-like pulses. The paths are measured relative to the position of the first oscillator. The area under the curves has been normalized so the total probability is 1.

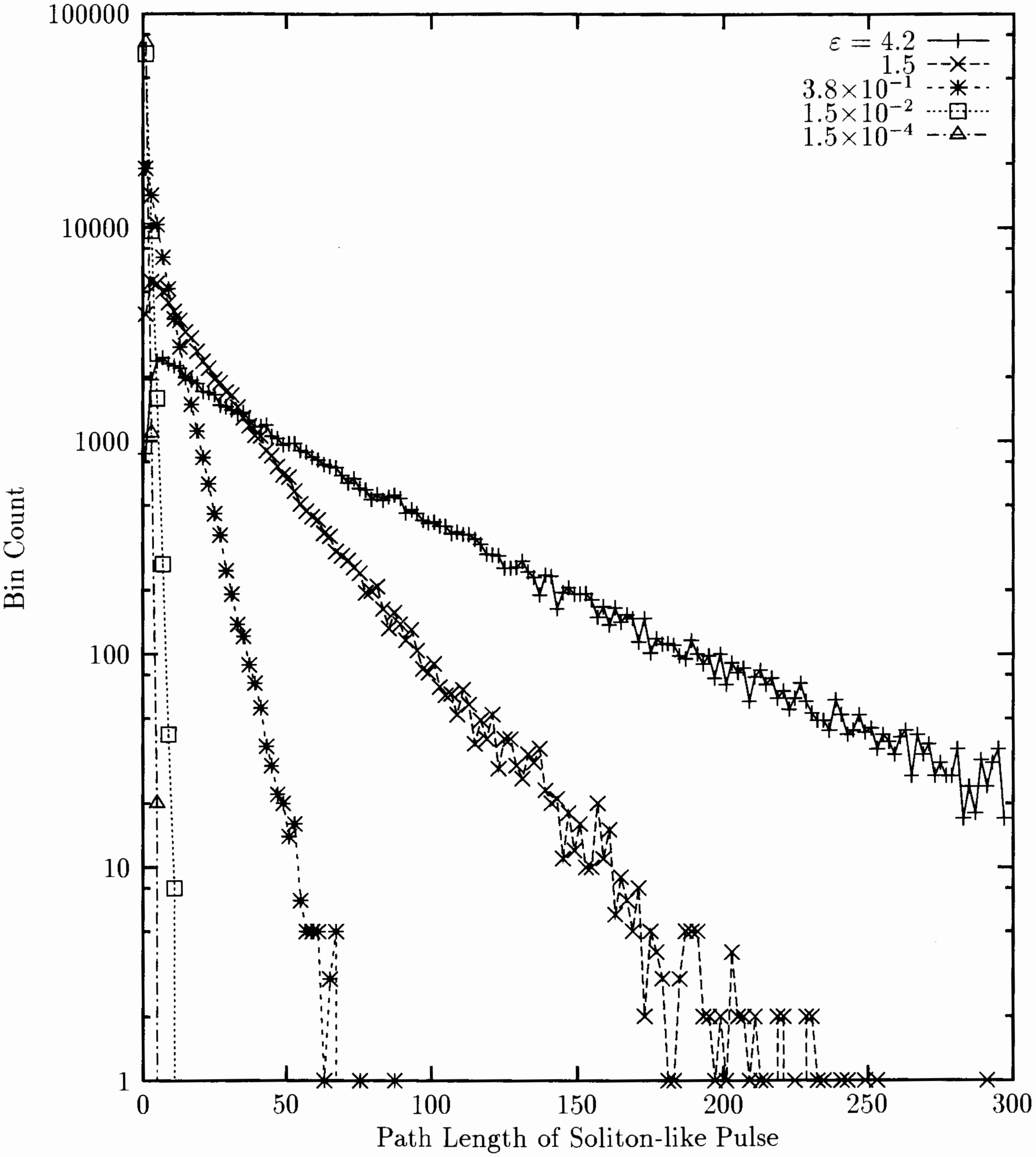

Figure 4.3: Distribution of path lengths for soliton-like pulses. The paths are measured relative to the position of the first oscillator. The y-axis represents the number of pulses within a particular bin.

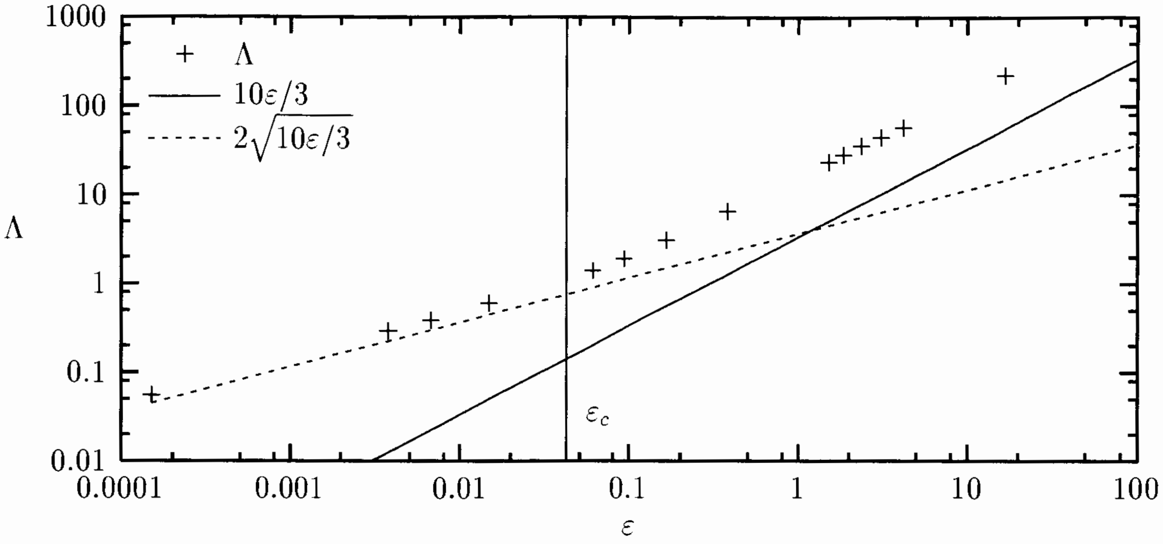

Figure 4.4: Mean free path length for soliton-like pulses.

by Fig. 4.6(c). The fixed point thus maps the system from a configuration similar to that shown in Fig. 4.6(c), onto itself.

To explain analytically the fixed point's destruction, we need to evaluate the position of the fixed point in phase space. Since the particles have just collided, their positions must satisfy Eq. (2.4)

$$x_b - x_f = 1, \tag{4.8}$$

where x_f and x_b are the position of the free and bound particles relative to their respective lattice sites. Also, the velocities are equal in size but opposite in direction, so that

$$-v_f = v_b = v, \tag{4.9}$$

where v_f and v_b are the velocities of the free and bound particles after the collision. From energy conservation, we have

$$E = \frac{1}{2}v^2 + \frac{1}{2}v^2 + \frac{1}{2}\omega^2 x_b^2 = 2, \tag{4.10}$$

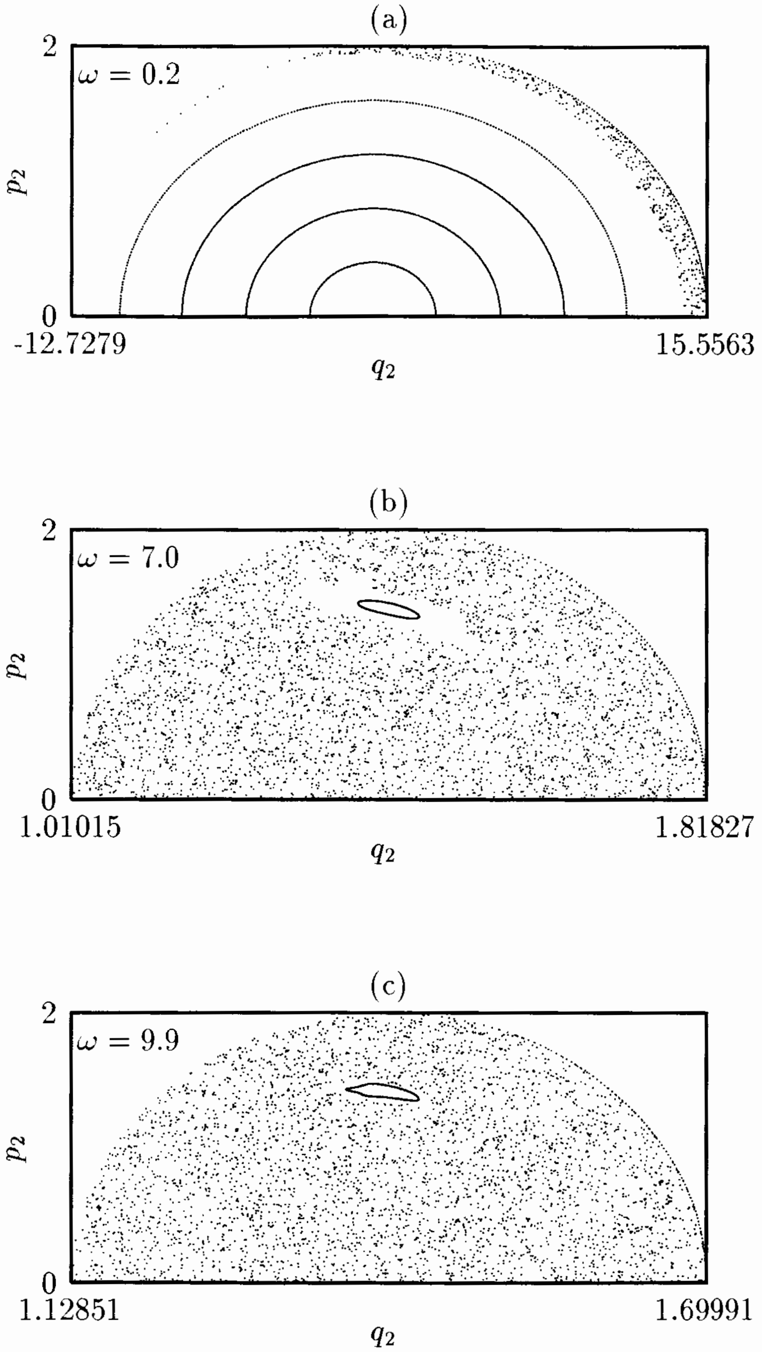

Figure 4.5: Poincaré section for the two particle periodic ring with (a)$\omega = 0.2 (\varepsilon = 37.5)$ (b)$\omega = 7.0 (\varepsilon = 0.0306)$ (c)$\omega = 9.9 (\varepsilon = 0.153)$ and an energy of 1 per particle.

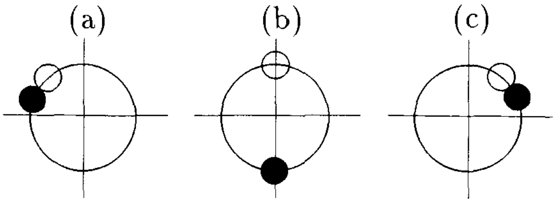

Figure 4.6: Two particles on a periodic ring, the solid circle represents a bound particle while the empty circle represents a free particle.

where we have made use of the initial condition on the energy as specified by CFVV. Solving for v yields

$$v = \left(2 - \frac{1}{2}\omega^2 x_b^2\right)^{\frac{1}{2}} . \tag{4.11}$$

The time t to travel from (b) to (a) is the same for both particles; hence,

$$t = \frac{x_f}{-v} = \frac{1}{w} \arctan \frac{\omega x_b}{v}. \tag{4.12}$$

Using this with Eq. (4.11) and Eq. (4.8) and solving numerically for v, x_f and x_b, we can predict the position of the fixed point in phase space. There are no real solutions for $\varepsilon > 0.151$ (corresponding to $\omega > 2.57$ for an energy per particle of 1 as specified by CFVV), which is consistent with the Poincaré sections. This dimensionless energy, $\varepsilon_p = 0.151$, is a convenient marker to identify the values of ε for which we may expect to see changes in the properties of the physical quantities of our system. It will be particularly relevant for measurements made on short chains.

The second fixed point shown in Fig. 4.5 (b) and (c) is somewhat more interesting. If we start with all the energy in the free particle and the bound particle at rest at its lattice site, then the free particle will collide and exchange velocities with the bound particle. The bound particle will swing out and back, collide with the free particle, and the free particle will travel all the way around the ring and collide with the bound particle. This is an interesting fixed point since it seems to be very persistent and goes stable and unstable periodically in ω, as shown in Fig. 4.7. Here, we have divided the phase space up into cells and then counted the number of points in each cell for

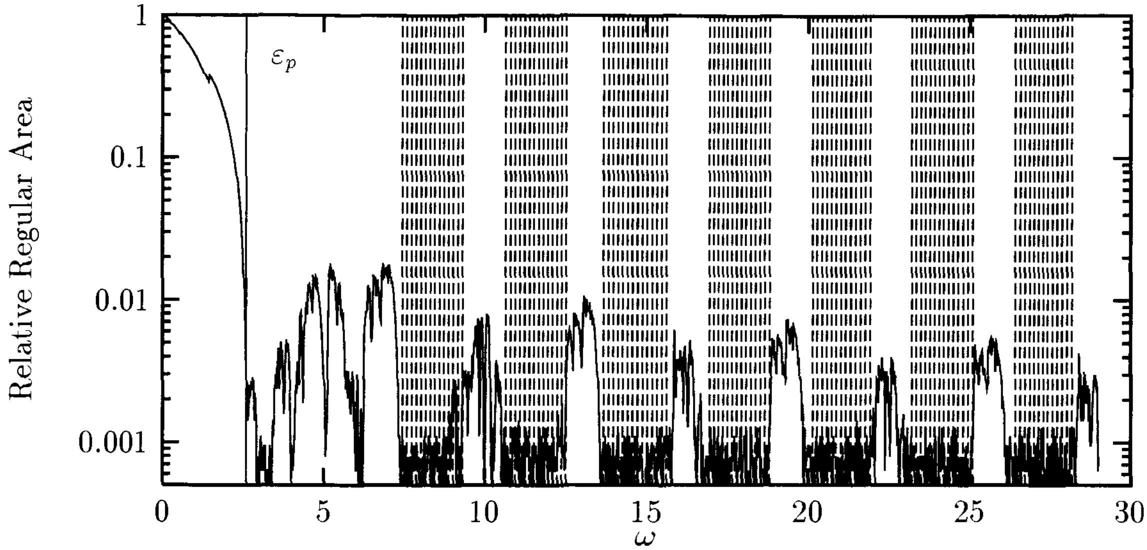

Figure 4.7: Relative unoccupied area in energetically accessible phase space.

1.4×10^6 collisions. Then, for a given ω we calculated the number of cells not visited by the trajectory relative to the total number of cells energetically accessible to it. There are several peaks between $\omega = 3$ and 7; however, they are from fixed points different from the ones described above. For larger ω, one can see the periodicity. Although the peaks are decaying (stable regions in phase space are shrinking), they are still visible for $\omega = 200$.

Stability analysis was performed on this fixed point, to help explain the periodicity in Fig. 4.7. We first need to linearize about this secondary fixed point which occurs at a (q_2, p_2) coordinate of $(\sqrt{2}, \sqrt{2})$. There are four collisions before the system returns to the same point in phase space. We will use the following notation: $\bar{\mathbf{\Gamma}}_i^0 = (x_f, v_f, x_b, v_b)$ and $\bar{t}_i$ is the time relative to the last collision for $i = 1, 2, 3, 4$. These collisions will occur at

$$\begin{aligned}
\bar{\mathbf{\Gamma}}^0_1 &= (+1,0,0,+2) \quad , \quad \bar{t}_1 = 1 \\
\bar{\mathbf{\Gamma}}^0_2 &= (+1,-2,0,0) \quad , \quad \bar{t}_2 = \pi/\omega \\
\bar{\mathbf{\Gamma}}^0_3 &= (-1,0,0,-2) \quad , \quad \bar{t}_3 = 1 \\
\bar{\mathbf{\Gamma}}^0_4 &= (-1,+2,0,0) \quad , \quad \bar{t}_4 = \pi/\omega,
\end{aligned} \tag{4.13}$$

where we know that the time for the free particle to travel around the loop is 1 and the time for the oscillator to swing out and back is half a period, π/ω. So we must iterate the map Eq. (2.5) four times to return to the fixed point. For a point near the fixed point this is

$$\bar{\mathbf{\Gamma}}^0_1 + d\gamma_j = f^{(4)}(\bar{\mathbf{\Gamma}}^0_1 + d\gamma_{j-1}), \tag{4.14}$$

where we have used the map f as defined in Eq. (2.5), $f^{(4)}$ signifies the map iterated four times, and $d\gamma_j$ is the size of the perturbation after j such four-fold iterations. We wish to convert this to

$$d\gamma_j = F(d\gamma_{j-1}). \tag{4.15}$$

The sequence is

$$\begin{aligned}
d\bar{\mathbf{\Gamma}}^0_2 &= f(\bar{\mathbf{\Gamma}}^0_1 + d\bar{\mathbf{\Gamma}}^0_1) - \bar{\mathbf{\Gamma}}^0_2 && (4.16)\\
d\bar{\mathbf{\Gamma}}^0_3 &= f(\bar{\mathbf{\Gamma}}^0_2 + d\bar{\mathbf{\Gamma}}^0_2) - \bar{\mathbf{\Gamma}}^0_3 && (4.17)\\
d\bar{\mathbf{\Gamma}}^0_4 &= f(\bar{\mathbf{\Gamma}}^0_3 + d\bar{\mathbf{\Gamma}}^0_3) - \bar{\mathbf{\Gamma}}^0_4 && (4.18)\\
d\bar{\mathbf{\Gamma}}^{0\prime}_1 &= f(\bar{\mathbf{\Gamma}}^0_4 + d\bar{\mathbf{\Gamma}}^0_4) - \bar{\mathbf{\Gamma}}^0_1, && (4.19)
\end{aligned}$$

where $d\bar{\mathbf{\Gamma}}^{0\prime}_1$ and $d\bar{\mathbf{\Gamma}}^0_1$ correspond to $d\gamma_j$ and $d\gamma_{j-1}$. In order to evaluate f, we must solve for the perturbed collision time $\bar{t}_i + d\bar{t}_i$. We can do this by using the collision criteria $q_1 = 0$ and Eq. (2.3),

$$q_1(t) = \frac{1}{\sqrt{2}}\left(\left(x^0_f + v^0_f t\right) - \left(x^0_b\cos(\omega t) - \frac{v^0_b}{\omega}\sin(\omega t) + 1\right)\right), \tag{4.20}$$

to solve for $d\bar{t}_i$ corresponding to a perturbation $d\bar{\mathbf{\Gamma}}^0_i$. In particluar, we have

$$d\bar{t}_i = \left(\left.\frac{\partial q_1}{\partial t}\right|_{\bar{\mathbf{\Gamma}}^0_i}\right)^{-1}\left(-dx_f\left.\frac{\partial q_1}{\partial x_f}\right|_{\bar{\mathbf{\Gamma}}^0_i} - dv_f\left.\frac{\partial q_1}{\partial v_f}\right|_{\bar{\mathbf{\Gamma}}^0_i} - dx_b\left.\frac{\partial q_1}{\partial x_b}\right|_{\bar{\mathbf{\Gamma}}^0_i} - dv_b\left.\frac{\partial q_1}{\partial v_b}\right|_{\bar{\mathbf{\Gamma}}^0_i}\right) \tag{4.21}$$

from linearizing Fig. 4.20 and solving for $d\bar{t}_i$. The new map $F(dx_f, dv_f, dx_b, dv_b)$ is now linearized about $d\gamma = 0$. Then, the coordinates are translated to q's and p's using

$$\begin{aligned} dx_f &= -1/\sqrt{2}(dq_1 + dq_2) && (4.22)\\ dv_f &= -1/\sqrt{2}(dp_1 + dp_2) && (4.23)\\ dx_b &= 1/\sqrt{2}(dq_1 + dq_2) && (4.24)\\ dv_b &= 1/\sqrt{2}(dp_1 + dp_2). && (4.25)\end{aligned}$$

Further, we set $dq_1 = 0$ and $dp_1 = -dp_2$ to ensure, respectively, that the particles collide and that energy is conserved. Finally, this leads us to

$$\begin{bmatrix} dq_2 \\ dp_2 \end{bmatrix} = M \begin{bmatrix} dq_2 \\ dp_2 \end{bmatrix}, \tag{4.26}$$

where

$$M = \begin{bmatrix} \cos(2\omega) - \frac{\pi}{2}\sin(2\omega) & \frac{3\pi}{\omega}\cos(2\omega) - \frac{(-2+\pi^2)}{\omega}\sin(2\omega) + \frac{\pi}{\omega} \\ -\frac{\omega\pi}{4}\cos(2\omega) - \frac{\omega}{2}\sin(2\omega) + \frac{\omega\pi}{4} & \left(1 - \frac{\pi^2}{2}\right)\cos(2\omega) - \frac{3\pi}{2}\sin(2\omega) + \frac{\pi^2}{2} \end{bmatrix}. \tag{4.27}$$

The eigenvalues of M are

$$\begin{aligned} e_\pm &= -\pi\sin(2\omega) - \left(\frac{\pi^2}{4} + 1\right)\cos(2\omega) + \frac{\pi^2}{4} \\ &\pm \frac{1}{4}\left((-2\pi^4 + 8\pi^2)\cos(2\omega) - 8\pi^3\sin(2\omega) + (-12\pi^2 + \frac{\pi^4}{2} + 8)\cos(4\omega)\right. \\ &\left. +(4\pi^3 - 16\pi)\sin(4\omega) + 4\pi^2 - 8 + \frac{3\pi^4}{2}\right)^{\frac{1}{2}}. \end{aligned} \tag{4.28}$$

These are plotted in Fig. 4.8. Since the Poincaré section is an area-preserving map, the product of the eigenvalues is 1 for all ω. The only way for the fixed point to be stable (that is, to have the magnitude of both eigenvalues less than or equal to 1) is for $e_\pm$ to be a complex conjugate pair of magnitude 1. This is the case for the plateau regions in Fig. 4.8. The complementary unstable ranges of ω are shown as shaded in Fig. 4.7, where we see good agreement with the destruction of the periodic regions

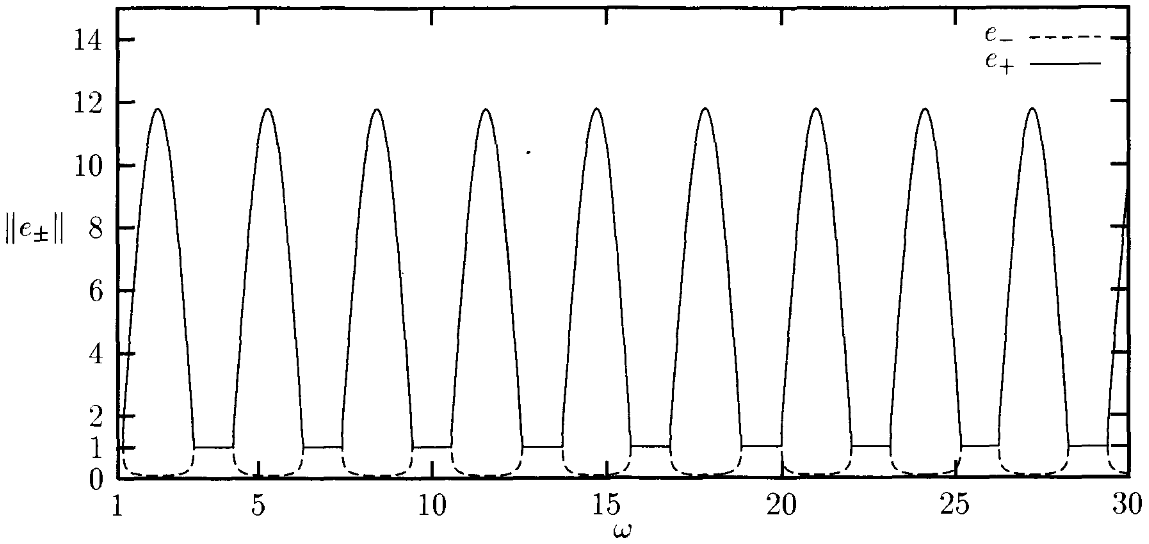

Figure 4.8: Magnitude of eigenvalues vs. the spring constant.

of phase space. As stated previously, there are several fixed-points that appear for $\omega < 7$, so the shading is only shown for $\omega > 7$, where the only fixed point present is the one we are interested in. For $\omega < 1$, the point in phase space is no longer a fixed point, since the amplitude of the oscillator is larger than 2 (the length of the loop), which would brake up the sequence Eq. (4.13) by introducing new collisions.

4.4 Energy Density

As mentioned in Ch. 2, the true energy density is equal to ε in the stiff-spring limit but is only $\frac{2}{3}$ of ε in the free particle limit. By calculating

$$\alpha = \frac{E/\omega^2}{\varepsilon}, \tag{4.29}$$

where E is the energy per particle, we will have a measure of which regime we are in for a particular ε. In Fig. 4.9, we can see that there is a transition region around

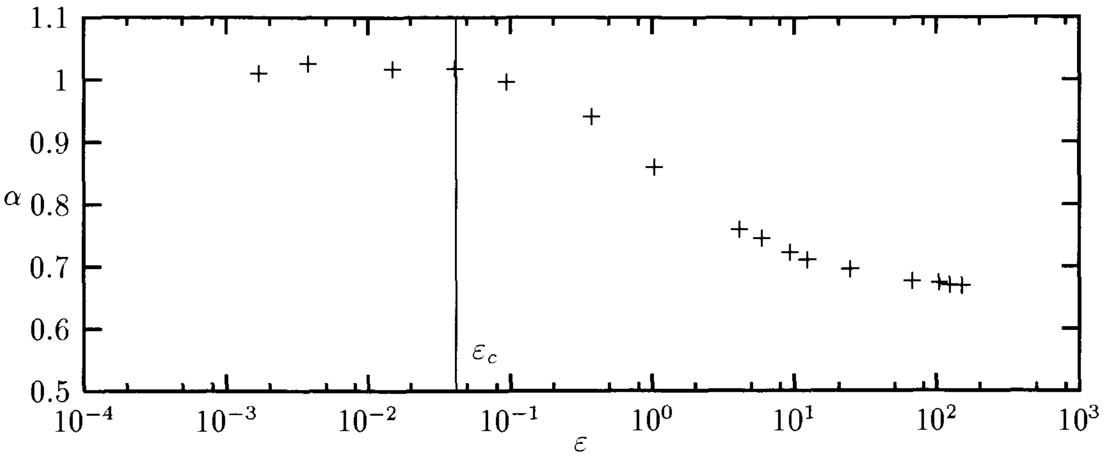

Figure 4.9: The ratio of the true energy density to ε for a 99 particle reservoir system.

$\varepsilon = 1$ separating the two limits. The total energy of the system can be attributed to three different sources. In the stiff-spring limit, $\frac{1}{3}$ of the total comes from the kinetic energy of the free particles, $\frac{1}{3}$ from the kinetic energy of the bound particles, and $\frac{1}{3}$ from the potential energy of the bound particles. In the weak-spring limit ($\varepsilon \to \infty$) the potential energy contribution becomes negligible. This leads to $\alpha_\infty = \frac{2}{3}$ in this limit and $\alpha_0 = 1$ in the opposite limit where the potential energy is not restricted.

From Fig. 4.9 we see the value of α is slightly greater than 1 in the stiff-spring limit, which may be attributed to the temperature dependence of κ. This causes the average temperature of the lattice to be larger than the average of the two reservoirs, T_{m}.

This quantity α plays a role in our calculation when we wish to know the temperature of a periodic chain, because in this case we specify the energy via the initial conditions not the temperature. Rewriting Eq. (4.29) using the definition of ε in Eq. (2.2), we have

$$T_{\mathrm{m}} = \frac{4E}{3\alpha}. \tag{4.30}$$

4.5 Collision Rate

The collision rate also shows a transition region that divides the two asymptotic limits. The definition of the collision rate per particle is

$$R = \frac{1}{2\tau} \tag{4.31}$$

where τ is the typical time between collisions and each collision takes place between 2 particles. In order to determine the asymptotic limits we need to estimate τ.

In the stiff-spring limit of $\varepsilon \to 0$, with a free and a bound particle originally at their respective origins, the position of the collision is determined by the amplitude of the oscillator. That is, since the oscillator's deviation from equilibrium is small, due to the strong spring, we can assume that a typical collision also takes place near the equilibrium position of the oscillator. We can estimate the time between such collisions as the time it takes the free particle to travel from its lattice site to the bound particles lattice site, and back. To do this we make use of the collision definition Eq. (2.4)

$$v_f \frac{\tau}{2} - 0 = 1 \tag{4.32}$$

where v_f is the velocity of the free particle, and the time, τ, includes both the time to travel from the origin to the collision and back. We have chosen particle i to be a free particle and particle $i+1$ to be a bound particle so v_f is a positive quantity, and from equipartition of energy we have $v_f = \sqrt{T_\mathrm{m}}$. This leads to a collision rate of $R_0 = \sqrt{T_\mathrm{m}}/4$ in the stiff-spring limit.

We now approximate R_∞, the collision rate in the $\varepsilon \to \infty$ limit. The bound particle behaves like a free particle, $v_f \approx -v_b \approx \sqrt{T_\mathrm{m}}$, thus

$$v_f \frac{\tau}{2} - v_b \frac{\tau}{2} = 1. \tag{4.33}$$

This leads to a value of $R_\infty = \sqrt{T_\mathrm{m}}/2$.

We would like to remove the ε dependence present in the limiting values in the form of $\sqrt{T_\mathrm{m}}$. Since it is E and not T_m that we specify in the closed system, we define the reduced collision rate $\mathcal{R}$ as

$$\mathcal{R} = \frac{R}{\sqrt{E}} = \frac{R}{\sqrt{\frac{3}{4}\alpha T_\mathrm{m}}}, \tag{4.34}$$

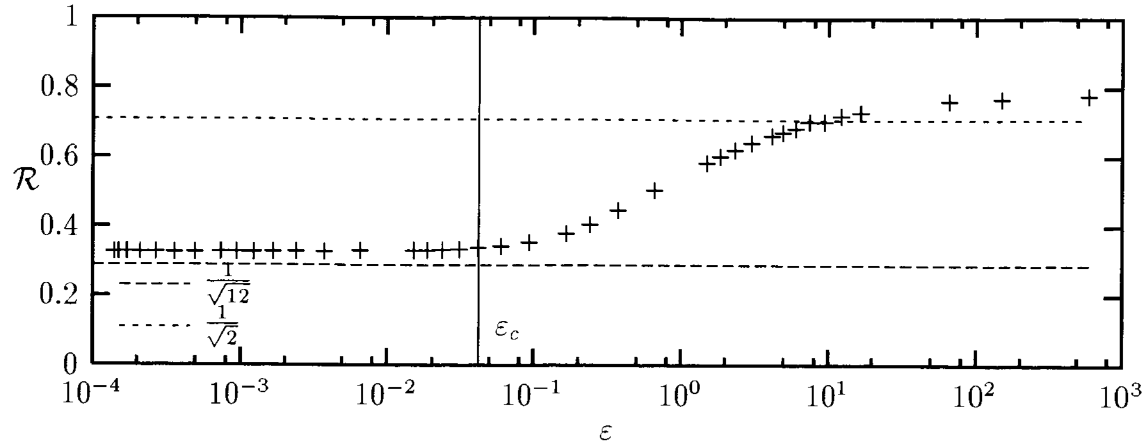

Figure 4.10: Reduced collision rate per particle for a 98 particle periodic ring.

where we made use of Eq. (4.30). This quantity is calculated for a 98 particle chain in Fig. 4.10 and shows two distinct limiting values. Using Eq. (4.34), we have estimates of $\mathcal{R}$ in the two limits

$$\mathcal{R}_0 = \frac{1}{4\sqrt{\frac{3}{4}\alpha_0}} = \frac{1}{\sqrt{12}} \tag{4.35}$$

$$\mathcal{R}_\infty = \frac{1}{2\sqrt{\frac{3}{4}\alpha_\infty}} = \frac{1}{\sqrt{2}} \tag{4.36}$$

which can be seen to agree well with the asymptotes in Fig. 4.10. The discrepancies are probably due to the neglected correlations.

4.6 Lyapunov Exponents

The maximum Lyapunov Exponent, λ, is a common indicator of the onset of chaos and would appear to be an ideal candidate for a dynamical indicator of the transition to normal thermal conductivity. λ is defined as

$$\lambda = \lim_{\substack{\delta\mathbf{\Gamma}\to 0 \\ t\to\infty}} \frac{1}{t} \ln\left(\frac{\|\mathbf{\Gamma}(\mathbf{\Gamma}_0 + \delta\mathbf{\Gamma}, t) - \mathbf{\Gamma}(\mathbf{\Gamma}_0, t)\|}{\|\delta\mathbf{\Gamma}\|}\right), \tag{4.37}$$

where $\mathbf{\Gamma}$ is the state vector describing the position of the system in phase space after evolving a time t from its initial state of $\mathbf{\Gamma}_0$ or $\mathbf{\Gamma}_0$ plus a small displacement $\delta\mathbf{\Gamma}$. We see from this definition that λ is a long time average measuring the exponential rate of separation of trajectories that are initially close in phase space. So, we have $\lambda > 0$ in a chaotic region and $\lambda = 0$ in a stable region. However, the relevant time scales for the conduction of heat via a lattice are the time for a particle to cross a lattice spacing or the transit time of soliton-like pulses across the lattice. These times are short, so the relevance of the long-time average λ on its own is uncertain; but, it will be made clear in what follows.

4.6.1 Calculation of λ

The Lyapunov exponent was calculated on a per collision basis, λ_C, which eliminates some technical problems with attempts to calculate the Lyapunov exponent on a per unit time basis, λ_t. The definition of λ_C is

$$\lambda_\mathrm{C} = \lim_{\substack{\delta\mathbf{\Gamma}\to 0\\ n\to\infty}} \frac{1}{n} \ln\left(\frac{||\mathbf{\Gamma}_n^0(\mathbf{\Gamma}_0+\delta\mathbf{\Gamma}) - \mathbf{\Gamma}_n^0(\mathbf{\Gamma}_0)||}{||\delta\mathbf{\Gamma}||}\right), \tag{4.38}$$

where, in contrast to being measured after a time t in Eq. (4.37), $\mathbf{\Gamma}_n^0$ is the state vector calculated after the n^{th} collision. The calculation of the Lyapunov exponent for a map is outlined by Rasband [Ras90]. Briefly, one evolves both a fiducial and perturbed trajectory from just after one collision to just after the next collision. Then, one renormalizes the perturbed trajectory with a scale factor. The maximum Lyapunov exponent is simply the sum of the log of these scales divided by the total number of collisions.

To understand the details of this, we make use of the fact that, since the separation of the trajectories is small, the vector defined by the difference between the perturbed and fiducial state vectors is tangential to the system's evolution. One can think of the evolution of this perturbation as the evolution of a vector $\mathbf{w}$ in tangent space. We will start by addressing the calculation of λ_t then λ_C. Consider Eq. (4.37) rewritten in terms of $\mathbf{w}$,

$$\lambda_\mathrm{t} = \lim_{t\to\infty} \frac{1}{t} \ln \frac{||\mathbf{w}(t)||}{||\mathbf{w}_0||}. \tag{4.39}$$

To calculate λ_t directly without periodic renormalization would lead to overflow errors on the computer. So, every t_i we calculate a scale factor α_i and use it to keep the size of $\mathbf{w} \approx \mathbf{w}_0$. For example,

$$\begin{aligned}
\alpha_1 &= \frac{\|\mathbf{w}(t_1)\|}{\|\mathbf{w}_0\|} && (4.40)\\
\mathbf{w}_1(t) &= \mathbf{w}(t)/\alpha_1 && (4.41)\\
\alpha_2 &= \frac{\|\mathbf{w}_1(t_2)\|}{\|\mathbf{w}_0\|} && (4.42)\\
\mathbf{w}_2(t) &= \mathbf{w}_1(t)/\alpha_2, && (4.43)
\end{aligned}$$

so

$$\mathbf{w}(t) = \alpha_1 \mathbf{w}_1(t) = \alpha_1(\mathbf{w}_2(t)\alpha_2). \tag{4.44}$$

That is, as long as we know the product of all the scale factors, we can always work back to the original unscaled $\mathbf{w}(t)$. In fact, at t_i all that is required to find $\mathbf{w}(t_i)$ is this product of the α's,

$$\mathbf{w}(t_2) = \alpha_1\alpha_2 = \frac{\|\mathbf{w}(t_1)\|}{\|\mathbf{w}_0\|}\frac{\|\mathbf{w}_1(t_2)\|}{\|\mathbf{w}_0\|}, \tag{4.45}$$

and

$$\|\mathbf{w}(t_n)\| = \prod_{i=1}^{n} \alpha_n. \tag{4.46}$$

This leads us to a new definition for λ_t,

$$\begin{aligned}
\lambda_t &= \lim_{n\to\infty} \frac{1}{t_n} \ln\left(\prod_{i=1}^{n} \alpha_i\right) && (4.47)\\
&= \lim_{n\to\infty} \frac{1}{t_n} \sum_{i=1}^{n} (\ln \alpha_i). && (4.48)
\end{aligned}$$

If λ is calculated on a per-collision basis, this becomes

$$\lambda_C = \lim_{n\to\infty} \frac{1}{n} \sum_{i=1}^{n} (\ln \alpha_i), \tag{4.49}$$

where

$$\alpha_i = \frac{\|\mathbf{w}_i\|}{\|\mathbf{w}_0\|}, \tag{4.50}$$

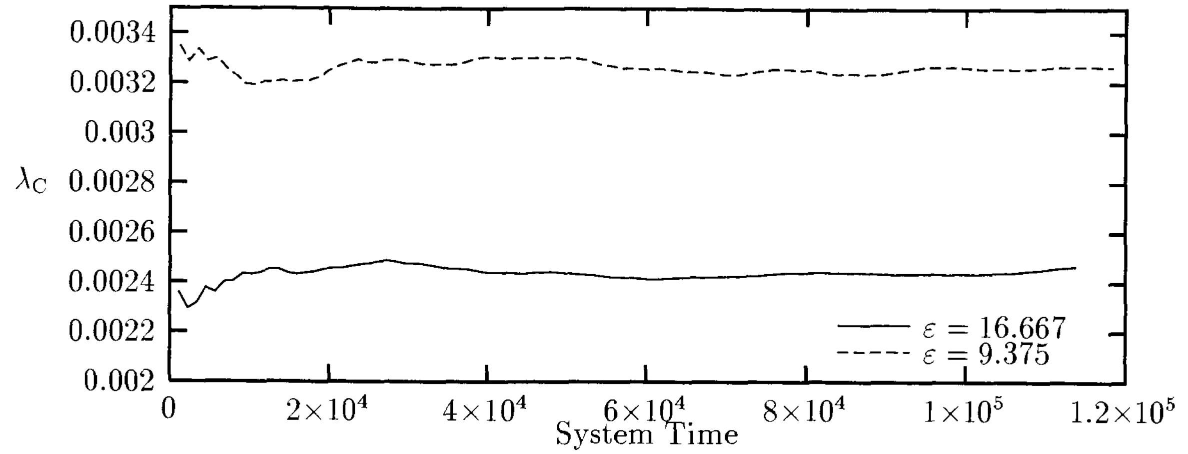

Figure 4.11: Lyapunov exponent for 98 particle lattice with $\varepsilon = 9.375$ and 16.667 as a function of system time to show the convergence.

that is, $\mathbf{w}_i$ is calculated at collision i rather than at time t_i (the distinction is more than semantic, as will be explained). The calculation of λ_C then is reduced to the accumulation of the log of the scale factors. To initiate the evolution, we need to define the perturbation. With the position of the perturbed and fiducial trajectories at collision i represented by $\mathbf{\Gamma}_{fi}$ and $\mathbf{\Gamma}_{pi}$, respectively, we make the identification

$$(\mathbf{\Gamma}_{fi} - \mathbf{\Gamma}_{pi}) = \mathbf{w}_i \tag{4.51}$$

and

$$\mathbf{w}_0 = (\mathbf{\Gamma}_{f0} - \mathbf{\Gamma}_{p0}) \tag{4.52}$$

$$||\mathbf{w}_0|| = \delta, \tag{4.53}$$

where δ is the initial perturbation.

There are some elements of the implementation of this algorithm that need to be made explicit. To arrive at an initial fiducial trajectory, we use the same technique developed for the calculation of κ. Typically, we evolve these generated coordinates for 10^5 collisions per particle to eliminate transients, then we take the coordinate at this time for $\mathbf{\Gamma}_{f0}$. To calculate the perturbation to add to the $\mathbf{\Gamma}_{f0}$ to get $\mathbf{\Gamma}_{p0}$, we generate a vector of uniformly distributed random numbers. This vector, $\mathbf{w}_0$, is then scaled so $\|\mathbf{w}_0\| = \delta$, where δ is our prescribed perturbation (typically 10^{-7}). Then, the fiducial and perturbed trajectories are evolved forwards in time. We cannot take more than one step in our evolution before rescaling because of the possibility that the collisions that occurred for the fiducial trajectory are not the ones that occurred for the perturbed trajectory (in this case the trajectories would not be topologically conjugate as required). The system is then evolved for enough collisions so that an accurate value for λ can be assured (greater than 10^6 collisions per particle) from plots such as Fig. 4.11. In fact, this figure is a "worst case" since these large ε values converge the slowest.

There is a problem with the scaling procedure as outlined in the algorithm since it doesn't include the constraint that the particles may not pass through each other. This is the major problem with the direct calculation of λ_t. Consider a pair of colliding particles, the fiducial pair $x_{fi}(t_{fj})$, $x_{fi+1}(t_{fj})$ and the perturbed pair $x_{pi}(t_{pj})$, $x_{pi+1}(t_{pj})$, where the subscripts f and p represent fiducial and perturbed trajectories for particle i at collision j. Since $t_{fj} \neq t_{pj}$, we must evolve the sooner of the two collisions forward to a common time t_j. This will separate the colliding pair slightly. Now we must calculate the scale factor and renormalize. We adjust the perturbed coordinates of these colliding particles,

$$\begin{aligned} x'_{pi}(t_j) &= x_{fi}(t_j) + \frac{1}{\alpha_j}(x_{pi}(t_j) - x_{fi}(t_j)) \\ x'_{pi+1}(t_j) &= x_{fi+1}(t_j) + \frac{1}{\alpha_j}(x_{pi+1}(t_j) - x_{fi+1}(t_j)). \end{aligned} \tag{4.54}$$

It is clear that this procedure may well cause the scaled perturbed particles to pass through one another, since there is no restriction that

$$x'_{pi}(t_j) + 1 \leq x'_{pi+1}(t_j), \tag{4.55}$$

where the term 1 is needed to account for the different origins. Since we know that Eq. (4.55) does apply for the fiducial coordinates, it is the second terms in Eq. (4.54) that cause the trouble. If particles i and $i+1$ were in contact in both fiducial and perturbed systems, then these terms would be equal and the scaling would simply be a translation of the pair. This is the case for the calculation of λ_C, since we no longer need to evolve the trajectories to the same time. We have estimated λ_t by calculating the product of λ_C and the collision rate. This is an acceptable approximation as long as the difference between the time of collision for the perturbed and fiducial trajectories do not contribute on average.

The numerical computation of λ can be tricky. The computed value may appear to be converging to a limit, only to abruptly shift to another value. This sequence of apparent convergences may depend on the initial conditions, even within a single chaotic region of phase space. Only when the trajectory has sampled all of the available phase space can we be sure of true convergence, and that is hard to ensure for a many-particle system. We have verified that our results for λ are not sensitive to changes in the initial conditions, size of the displacement of the perturbed trajectory from the fiducial trajectory, and the type of norm used to measure the separation between trajectories. Table 4.1 presents some of this data.

4.6.2 Results for the λ calculation

Like the energy density and the collision rate, the Lyapunov exponent displays a change in behaviour during the transition between the two limits. In Fig. 4.12 we see that λ_C obeys a power law with a sharp change in slope. A power-law fit of the data for the two limits is also shown in the figure to emphasize the behaviour. λ_t also obeys a power law, with some deviations; however, the sharp transition is not seen. Since the ratio of λ_C and λ_t is the collision rate and the collision rate displays two essentially constant regions separated by a transition region, one would expect to see some reflection of this in Fig. 4.12. The sharp change in slope for λ_C is at approximately the same ε as the start of the transition region in both Fig. 4.9 and 4.10. While there is some evidence of a change of behaviour for λ_t at $\varepsilon \approx 10$ (where the transition region ends), more data would be required to confirm this.

The data in Fig. 4.12 is for a 98-particle lattice, from which we infer the behaviour of an infinite lattice. To understand how the features in Fig. 4.12 depend on lattice

	$\omega = 0.3$	$\omega = 0.4$
(a)	$0.01230 \pm 6.7\%$	$0.01524 \pm 4.8\%$
(b)	$0.01238 \pm 10.4\%$	$0.01544 \pm 6.6\%$
(c)	$0.01216 \pm 8.1\%$	$0.01538 \pm 2.7\%$
(d)	$0.01264 \pm 9.0\%$	$0.01542 \pm 5.0\%$
(e)	$0.01188 \pm 10.2\%$	$0.01535 \pm 5.2\%$
(f)	$0.01220 \pm 8.7\%$	$0.01534 \pm 3.6\%$
(g)	$0.0118621 \pm 7.3\%$	$0.0150530 \pm 3.1\%$
(h)	$0.0118622 \pm 7.3\%$	$0.0150532 \pm 3.1\%$
(i)	$0.0118615 \pm 7.3\%$	$0.0150528 \pm 3.1\%$

Table 4.1: Comparison of our values for λ with $N = 21$ and $\omega = 0.3$ and 0.4. These values are the averages of 20 runs and the errors represent the standard deviation of the sample. (a) Uses the technique to generate initial conditions for long lattices, perturbation of 1×10^{-7}, 1×10^{4} transient collisions per particle, modulus used was $\sqrt{v^2 + x^2}$. (b) As (a) except uses the technique to generate initial conditions for short lattices. (c) As (a) except perturbation of 5×10^{-8}. (d) As (a) except perturbation of 2×10^{-7}. (e) As (a) except 1×10^{5} transient collisions per particle. (f) As (a) except 1×10^{3} transient collisions per particle. (g) As (a) except different set of 20 initial conditions. (h) As (g) but modulus used was $\sqrt{x^2}$. (i) As (g) but modulus used was $\sqrt{v^2}$

size, we show some smaller lattices in Fig. 4.13. As expected, ε_p accurately predicts the transition in the 2 particle case, but for 98 particles the transition occurs at a smaller ε. Note also that for $N > 2$ there is a noticeable curvature which changes from convex to concave. This feature is still noticeable for $N = 98$.

An idea of Pettini and Landolfi [PL90] may explain the physical significance of the change of slope in Fig. 4.12. They studied the time to equipartition of two different coupled anharmonic oscillator systems and found that there is a change in scaling behaviour for $\lambda(\varepsilon)$ beyond the energy density for which all stable regions of phase space disappear. The value of the energy density at which this strong stochasticity threshold, as they call it, occurs was later verified by an analytical technique [CLP95].

In the work of Pettini and Landolfi, the time scale for a system's approach to equipartition was studied, and two time scales, one fast and one slow, were discovered. The slow approach to equipartition is characteristic of a system soon after the onset of chaos. In this case chaotic trajectories diffuse through phase space along the intersection of the homoclinic manifold of the large dimensional phase space, that is, along the threads of the so called Arnold web. As the energy density increased a transition in the time scale to equipartition was observed. This is due to a breakdown of the Arnold web, so that now the system is able to diffuse freely rather than just along the resonances. This transition in time scales is seen to occur at the same critical dimensionless energy as the strong stochasticity threshold.

We have found very similar results for conductivity in the ding-a-ling system. In Fig. 4.12 there is a change in the power law dependence of our Lyapunov exponent calculations at the same dimensionless energy as a change in *length* scale for convergence to a Fourier law conductivity. Pettini and Landolfi found that for $\varepsilon > \varepsilon_c$ the *time* to reach equipartition for a system with only a few initially excited normal modes increased as a power law, while for $\varepsilon < \varepsilon_c$ the *time* was independent of ε. We have seen in Fig. 3.20 that the *length* scale needed to reach a Fourier law regime had both a power law and an approximately constant region. Note that the integrable limit for the ding-a-ling system is high energy, rather than low energy as in the systems studied by Pettini and Landolfi, so the dependence of the transition on energy density is reversed.

Since the strong stochasticity threshold is meant to indicate the destruction of all stable regions in our large dimensional phase space, it is instructive to look also at λ for the 2 particle case in Fig. 4.13, since then we have Poincaré sections that will confirm this. There is a lot of structure around $\varepsilon = \varepsilon_p$, which corresponds to the dimensionless energy of the destruction of the main fixed point. The solid vertical line at ε_p does indeed appear to separate different kinds of behaviour for the Lyapunov exponent. For larger N the transition ε is smaller, converging to the value ε_c as shown in Fig. 4.12. Table 4.2 shows how this critical ε varies with the chain length. In Ref. [CLP95] it is proven that the infinite chain limit of ε_c exists, and Table 4.2 shows that in the ding-a-ling system it reaches quickly.

In Fig. 4.12 we see that the transition in the value of $\bar{\mu}^2$ does coincide with the

N	critical ε
18	0.031
38	0.055
58	0.032
78	0.042

Table 4.2: Intersection of power-law fits of the Lyapunov exponent for short lattices.

transition in λ. In Ref. [PL90] it was stressed that equipartition is always reached if one waits long enough and that the transition is simply one of scale. For our system we find that the Fourier law should always be obeyed if one makes the lattice large enough.

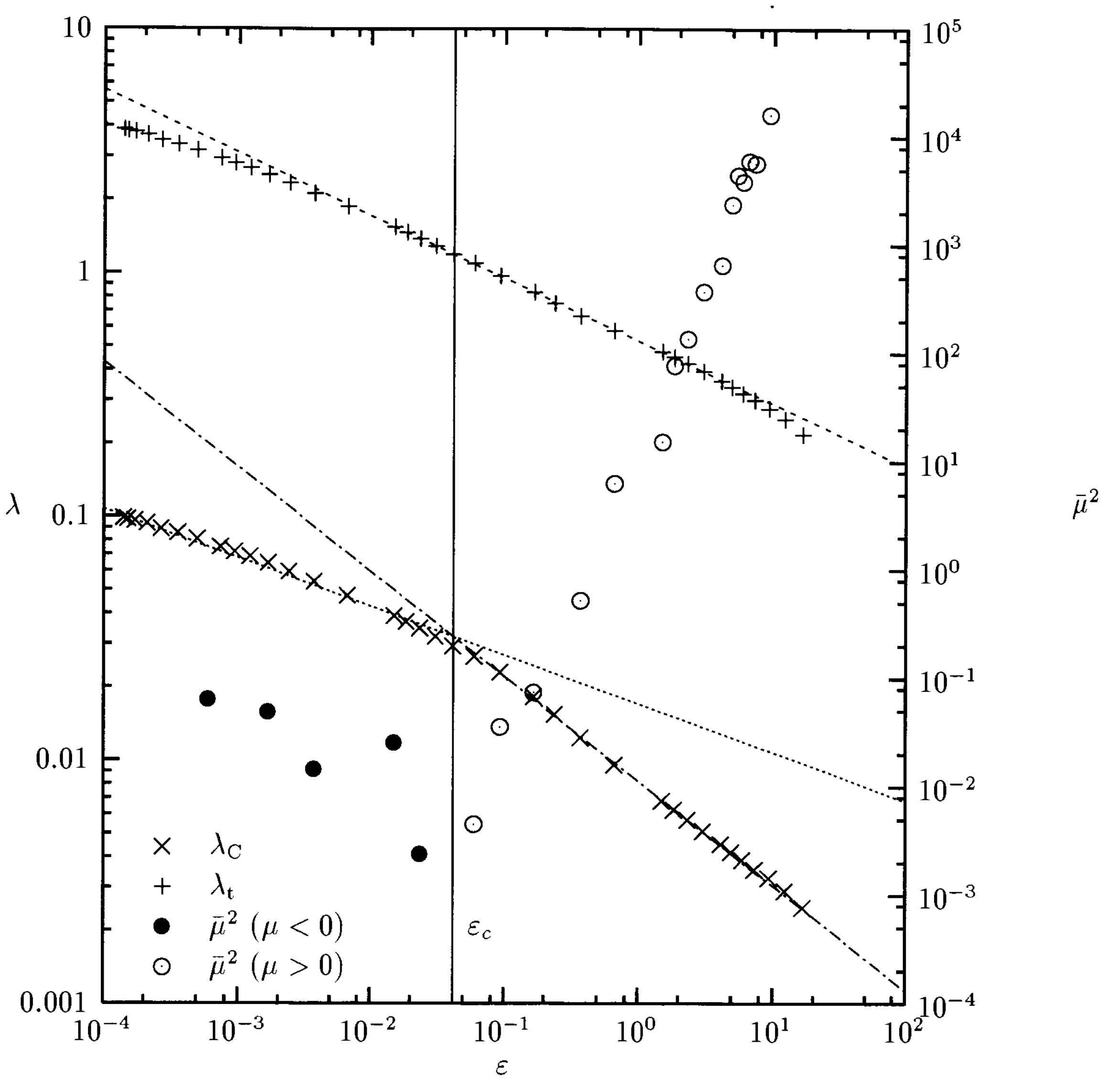

Figure 4.12: Lyapunov exponent for 98-particle lattice, with λ calculated both per unit time and per collision. For comparison, $\bar{\mu}^2$ is replotted.

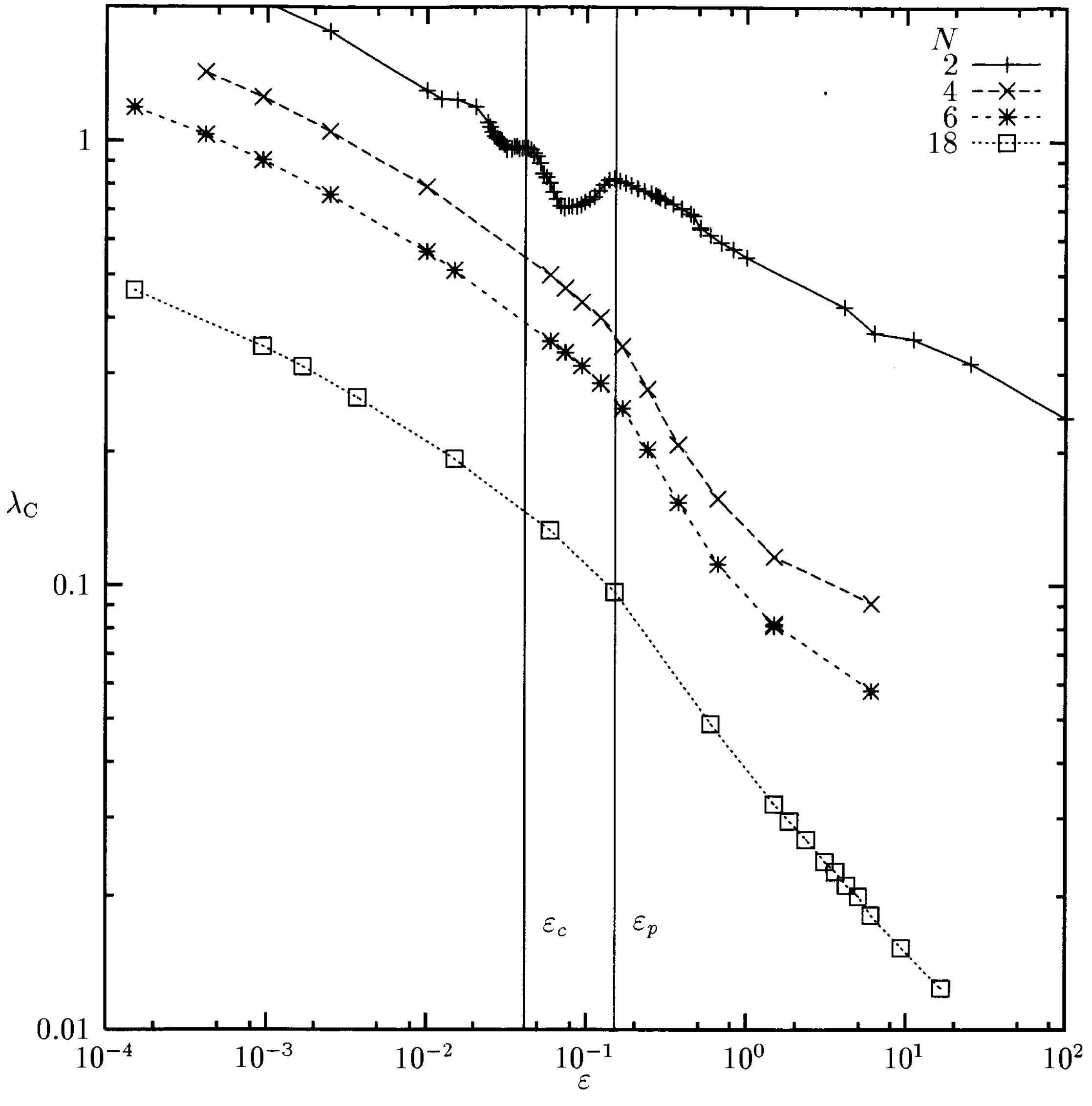

Figure 4.13: Lyapunov exponent, calculated per collision, for small lattices.

Chapter 5

Alternative Models

Having achieved success at producing normal thermal conductivity with the ding-a-ling model, we considered other models. They are needed both to confirm and to extend the range of possible observations about Fourier's law. It has been shown [JM89] that increasing the number of dimensions does not qualitatively affect the system's thermal properties, so higher dimensional systems were not investigated. Before proposing alternate models, we consider some of the essential features of the ding-a-ling model.

The computational efficiency that the ding-a-ling model achieves is primarily due to the possibility of describing its time evolution as a map. Its success at demonstrating normal thermal conductivity can be attributed to the chaotic nature of the map. To see this normal behaviour in very short lattices, the model used stiff-springs to produce random phases between collisions and to minimize energy transport via solitary pulses.

The goal in proposing a model was to enhance the useful properties found in the ding-a-ling model while only eliminating aspects that were not essential to the physics. The most time consuming part of the evaluation of the ding-a-ling model was the calculation of the collisions times. This required the use of a rootsolver. The elimination of this step could improve the computational power of the routine by an order of magnitude. With this efficiency we may be able to extend the investigation of Fourier law conductivity to its limits, including the way it breaks down as the chaos is reduced. For the ding-a-ling model, this is in the weak-spring limit, where it is difficult to get accurate asymptotic values of κ, as shown by Fig. 3.15.

5.1 The Linear Plus Complex Oscillator Model

The linear plus complex oscillator (LPCO) lattice is similar to the ding-a-ling in that it is a chain of free and oscillatory particles. However, the oscillators are highly idealized, having both real and imaginary momentum components but with a fixed position. The reason for having the oscillators fixed was to make this model computationally more efficient than the ding-a-ling model, since it allowed for the calculation of the collision times without the need for the evaluation of a root involving a transcendental function. The lack of a variable position lead to the addition of an imaginary component of the momentum so the oscillators still contributed one degree of freedom (a 2-d phase space) just like the oscillators in the successful ding-a-ling model.

In this system the free particles travel from lattice site to lattice site and collide elastically so as to exchange real momenta. The fact that the collisions occur only at the lattice sites makes this model somewhat similar to the stiff-spring limit of the ding-a-ling model. Unlike the ding-a-ling model the free particles can pass through the bound particles, so they can travel throughout the lattice. (This is a necessity since the oscillator may have a momentum in the same direction as the free particle at the time of collision but the bound particle must remain fixed to its lattice site.) The free particles do not collide with each other but only with bound particles. The momenta of the bound particles can be described by the following,

$$p_i(t) = A_{ij}^0 e^{i(\omega(t-\tau_j)+\phi_{ij}^0)} \tag{5.1}$$

for $\tau_j < t \leq \tau_{j+1}$, where we have used the same notation as used in Ch. 2, A_{ij}^0 and ϕ_{ij}^0 are the amplitude and phase of the oscillations of particle i between collision j and $j+1$. The calculation of the collision time τ_j is performed by choosing the value of the earliest free particle collision with a bound particle lattice site. The details of the execution of the map are worked out in the next section for the two-particle case. The generalization to large lattices should be obvious.

5.1.1 Phase Space

It is necessary that the model have a chaotic limit. To examine this we make use of the method of Poincaré sections, as we did in Sect. 4.3 for the ding-a-ling model. The implementation of this technique requires the definition of the map for a loop containing one free and one bound particle.

The equations of motion for the system between collisions are

$$p = \alpha e^{i(\omega \Delta t + \phi)} \quad . \tag{5.2}$$

and

$$v_f = \frac{\ell}{\Delta t}, \tag{5.3}$$

where ℓ is the length of the loop and Δt is the time between collisions. These equations apply between collisions. We will need some notation to distinguish between events before and after the collisions,

$$q(t_i \pm \delta) = q^i_{\pm}, \tag{5.4}$$

where q is some measured quantity and t_i the time of collision i. The collisions are assumed to be elastic so the following conditions hold:

$$p^i_{I-} = p^i_{I+}, \qquad p^i_{R-} = v^i_{f+}, \qquad v^i_{f-} = p^i_{R+}, \tag{5.5}$$

where $p_R = \Re(p)$ and $p_I = \Im(p)$. This leads to the mapping,

$$\begin{aligned} p^{i+1}_{I-} &= \alpha^i_+ \sin(\omega \Delta t^i + \phi^i_+) && (5.6)\\ p^{i+1}_{R-} &= \alpha^i_+ \cos(\omega \Delta t^i + \phi^i_+) && (5.7)\\ v^{i+1}_{f-} &= v^i_{f+}, && (5.8) \end{aligned}$$

where we have

$$\begin{aligned} \alpha^i_+ &= \left((p^i_{R+})^2 + (p^i_{I+})^2\right)^{\frac{1}{2}} && (5.9)\\ \phi^i_+ &= \tan^{-1}\left(\frac{v^i_{I+}}{v^i_{R+}}\right) && (5.10)\\ \Delta t^i &= t^{i+1} - t^i = \frac{\ell}{|v^i_{f+}|}. && (5.11) \end{aligned}$$

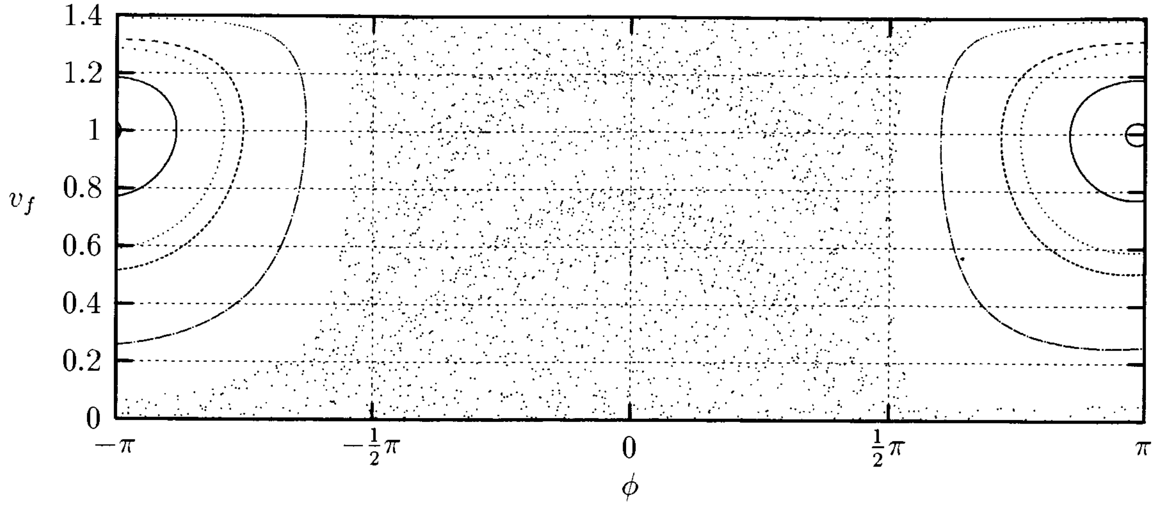

(a) $\omega = 0.10$

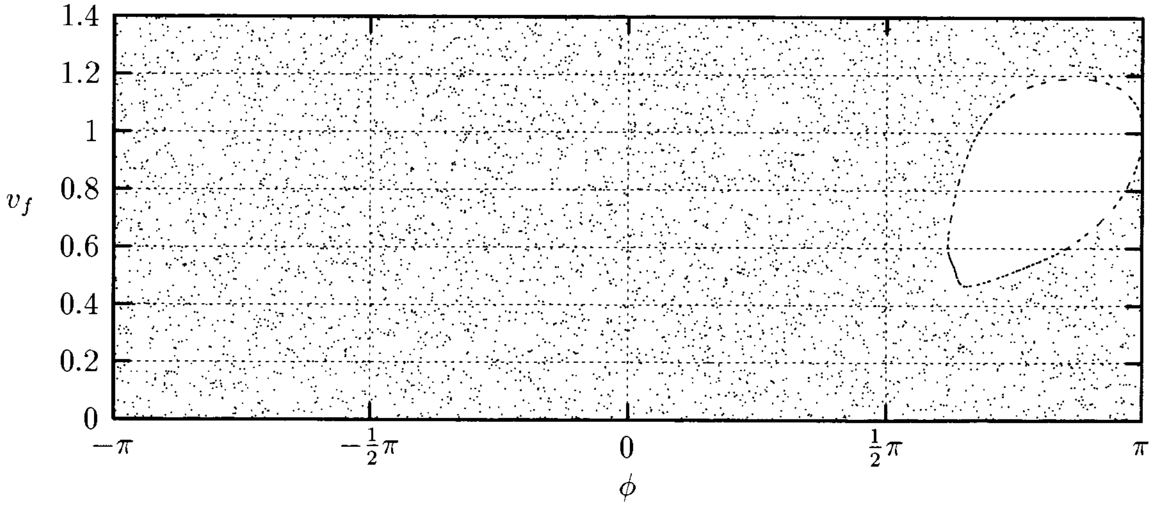

(b) $\omega = 1.00$

Figure 5.1: Phase space of the LPCO system showing the reduction of chaos in the weak-spring limit.

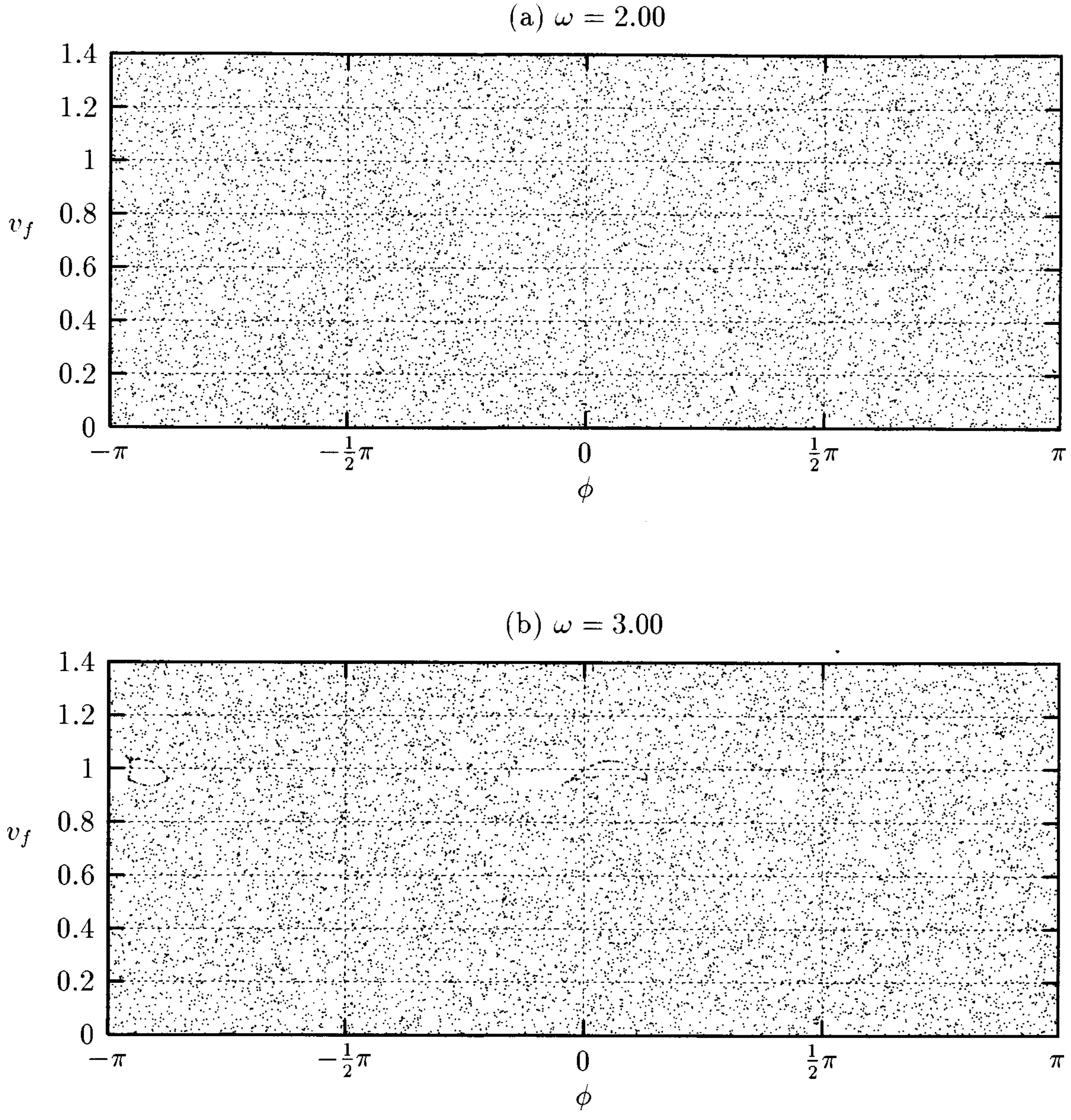

Figure 5.2: Phase space of the LPCO system showing that total chaos is achieved in the stiff-spring limit but (like the ding-a-ling system) the model has small periodic regions that appear at larger ω. These periodic regions appear in (b) for $v_f = 1$ and $\phi = -\pi, 0$

Note that, ϕ^i_+ is the phase in complex space for the momentum p just after collision i, while ϕ^i_- is the phase just before collision i. Also, α will be constant between the collisions. So we have

$$\alpha^{i+1}_- = \alpha^i_+ \tag{5.12}$$

$$\phi^{i+1}_- = \tan^{-1}\frac{p^i_{I+}}{p^i_{R+}} + \frac{\omega\ell}{|v^i_{f+}|} \tag{5.13}$$

$$\phi^i_+ = \tan^{-1}\frac{p^i_{I+}}{p^i_{R+}} = \phi^{i+1}_- - \frac{\omega\ell}{|v^i_{f+}|}. \tag{5.14}$$

If we use Eq. (5.11) to eliminate Δt^i we have 10 variables $p_{R\pm}, p_{I\pm}, v_{f\pm}, \alpha_\pm, \phi_\pm$. We will use Eq. (5.5) to choose either + or −, that is, evaluate just before or just after the collision. This will reduce the possible number of variables further to 5. Then we will use Eq. (5.6) to Eq. (5.14) to reduce this further to 3 variables. Finally, energy conservation will allow us to reduce it to the 2 variables needed to define a Poincaré section.

Start with Eq. (5.9) and use Eq. (5.5) with (Eq. (5.6) and Eq. (5.8) to get rid of p_R and p_I, so

$$\alpha^{i+1}_+ = \left((p^{i+1}_{R+})^2 + (p^{i+1}_{I+})^2\right)^{\frac{1}{2}} \tag{5.15}$$

$$= \left[(v^i_{f+})^2 + \left(\alpha^i_+ \sin\left(\frac{\omega\ell}{|v^i_{f+}|} + \phi^i_+\right)\right)^2\right]^{\frac{1}{2}}. \tag{5.16}$$

Start from Eq. (5.10) and eliminate p_R and p_I as above,

$$\phi^{i+1}_+ = \tan^{-1}\frac{p^{i+1}_{I+}}{p^{i+1}_{R+}} \tag{5.17}$$

$$= \tan^{-1}\left(\frac{\alpha^i_+}{v^i_{f+}} \sin\left(\frac{\omega\ell}{|v^i_{f+}|} + \phi^i_+\right)\right). \tag{5.18}$$

Start from Eq. (5.5) and use Eq. (5.7) to give

$$v^{i+1}_{f+} = p^{i+1}_{R-} \tag{5.19}$$

$$= \alpha^i_+ \cos\left(\frac{\omega\ell}{|v^i_{f+}|} + \phi^i_+\right). \tag{5.20}$$

Dropping the plus signs gives these equations that apply just after the collision,

$$\alpha^{i+1} = \left[(v_f^i)^2 + \left(\alpha^i \sin\left(\frac{\omega\ell}{|v_f^i|} + \phi^i\right)\right)^2\right]^{\frac{1}{2}} \tag{5.21}$$

$$\phi^{i+1} = \tan^{-1}\left(\frac{\alpha^i \sin\left(\frac{\omega\ell}{|v_f^i|} + \phi^i\right)}{v_f^i}\right) \tag{5.22}$$

$$v_f^{i+1} = \alpha^i \cos\left(\frac{\omega\ell}{|v_f^i|} + \phi^i\right). \tag{5.23}$$

Since the energy is conserved in the collision, we have

$$E = \frac{1}{2}p^2 + \frac{1}{2}v_f^2 \tag{5.24}$$

$$2E = p_R^2 + p_I^2 + v_f^2 \tag{5.25}$$

$$\alpha = (2E - v_f^2)^{\frac{1}{2}}. \tag{5.26}$$

This allows us to reduce the number of variables to 2 and leaves us with a useful map. So, using variables evaluated just after the collision gives

$$\phi^{i+1} = \tan^{-1}\left(\frac{\left(2E - (v_f^i)^2\right)^{\frac{1}{2}} \sin\left(\frac{\omega\ell}{|v_f^i|} + \phi^i\right)}{v_f^i}\right) \tag{5.27}$$

$$v_f^{i+1} = \left(2E - (v_f^i)^2\right)^{\frac{1}{2}} \cos\left(\frac{\omega\ell}{|v_f^i|} + \phi^i\right), \tag{5.28}$$

where we have used Eq. (5.26) with Eq. (5.22) then Eq. (5.23).

We have implemented Eq. (5.27) and Eq. (5.28) for a few values of ω as shown in Fig. 5.1 and Fig. 5.2. The important result is that, as seen in Fig. 5.2(a), there is total chaos for large ω and that, as seen in Fig. 5.1(a), the chaos will be reduced by lowering ω. The fact that there is a small periodic region for $\omega = 3$ (see Fig. 5.2(b)) should not cause concern since similar-sized periodic regions were found for large ω in the two particle ding-a-ling loop (see Fig. 4.5). For all larger ω values examined, the chaos appears total.

5.1.2 Establishing a stable thermal gradient

As with the ding-a-ling model, we place the LPCO system between two reservoirs at different temperatures and measure the flux J and the temperature gradient ∇T. From this, we wish to calculate the thermal conductivity $\kappa = -J/\nabla T$.

The first step is to set up the reservoirs. The obvious choice is to use the same reservoirs as used in the ding-a-ling lattice (Eq. (3.1)). In Fig. 5.3, we see the results of this choice of reservoir. We have used a lattice of 50 free and 50 bound particles between two reservoirs both set to a temperature of 2. The resulting average momentum distribution of all free particles (Fig. 5.3(a)) is unusual in that, per collision, the distribution corresponds to a temperature of approximately 4. The correct distribution for a particle with $T = 2$ is shown with a solid line. The distribution per unit time is even more peculiar, displaying a strongly singular behaviour at the origin. This heavy weighting of slow velocities for the free particles results from the fixed distance between collisions, since these slow particles take a long time to travel across the lattice spacing. In the ding-a-ling lattice, a slow particle would likely be met by an oscillator with a large amplitude, thus reducing its lifetime. The average momentum distributions for the two components of the bound particles also show an unusual temperature dependence. These were only calculated on a per-collision basis. The energy distribution of the oscillators was also calculated, and while it shows this same distribution per unit time as per collision, that distribution also corresponds approximately to a temperature of 4 instead of 2.

From Fig. 5.3, we see that the real and imaginary momenta of the bound particles and the momentum of the free particles have the same distribution per collision, but their temperature is not the same as the reservoir's. To address this, we recognized that the momentum distribution of the free particles per collision was Gaussian. Because this is the distribution leaving the bound particles, we should perhaps use a Gaussian for the reservoirs since they should interact with the free particles as the bound particles do. Also, we realized the average temperature of a particle leaving our previous reservoirs was $2T$ (due to the weighting of the faster particles) and that this was exactly what we were seeing with our equilibrium system temperature of 4.

(a)Free particle momentum distribution

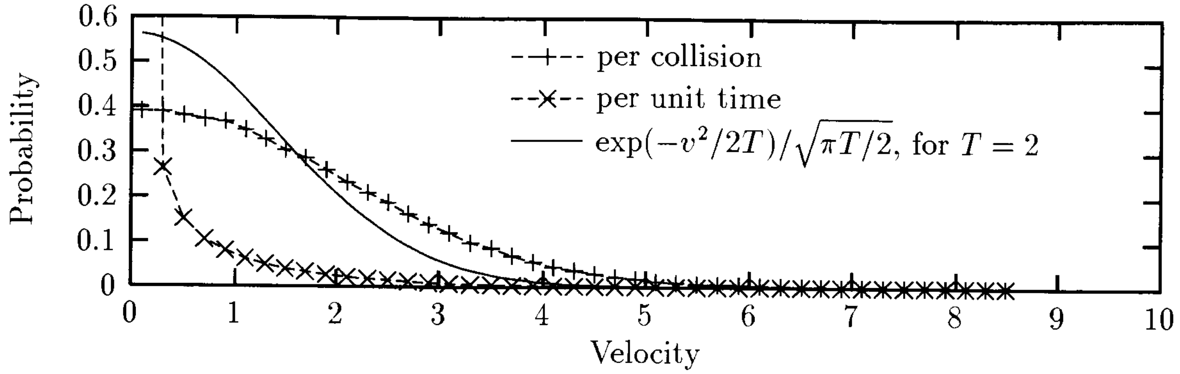

(b)Bound particle momentum distribution per collision

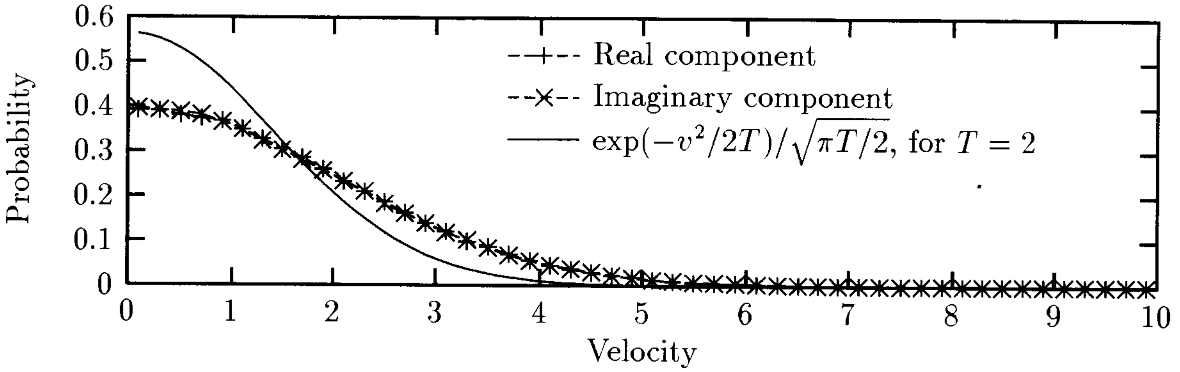

(c)Energy distribution

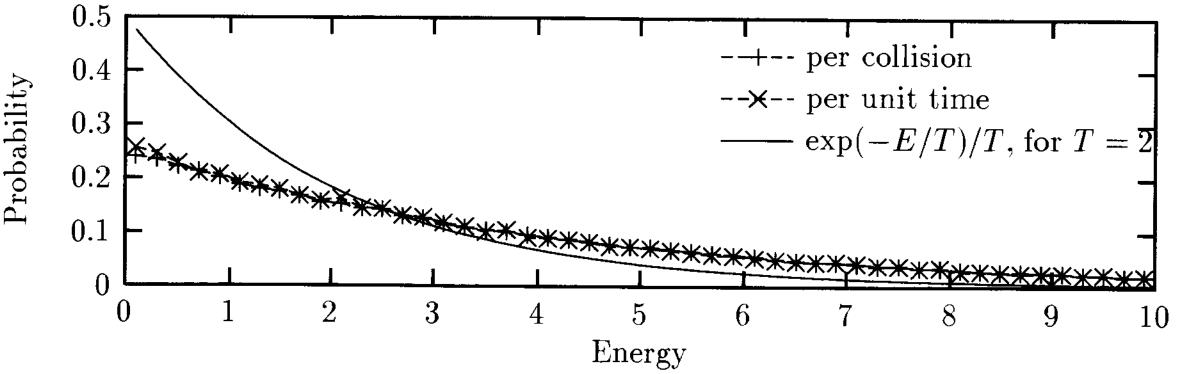

Figure 5.3: The energy and momentum distributions for the particles in the lattice. The reservoirs are the same as in the ding-a-ling model $(|v|\exp(v^2/2T))/\mathrm{T}$.

These two points lead us to try a pure Maxwell velocity distribution

$$P(v) = \frac{1}{\sqrt{\pi T/2}} \exp(-\frac{1}{2}v^2/T) \tag{5.29}$$

for our reservoirs. We have recalculated the system's momentum and energy distributions in Fig. 5.4 using reservoirs with this velocity distribution. Now we have all the momenta in equilibrium with each other and the reservoirs.

For an explanation as to why the original reservoirs are failing to establish the correct equilibrium distribution for the system, we must look at how the distribution is derived. The process we are trying to simulate when the end particle collides with the lattice boundary is the collision of a system particle with a member of a large collection of particle in equilibrium at a temperature T (the reservoir). Conceptually, the Maxwell velocity distribution for the particles inside the 1-d reservoir at temperature T is

$$P(v)dv \propto \exp(-\frac{1}{2}v^2/T)dv. \tag{5.30}$$

This is the probability of finding a particle with a velocity between v and $v + dv$ per unit length of the reservoir. When an interaction between the system and the reservoir occurs the particle is absorbed by the reservoir and ejected back into the system with the first collision it has in the reservoir. It is the velocity distribution of these reservoir particles that we use as our reservoir distributions. Consider only those reservoir particles within dv of v. They move a distance vdt in time dt. Since we assume the particles in the reservoir are uniformly distributed in space, then the probability a particle would collide with the position of the system particle in the time dt is $vP(v)$ per unit time. When we normalize this to a unit probability we get Eq. (3.1)

$$P(v) = (|v|/T)\exp(-\frac{1}{2}v^2/T). \tag{5.31}$$

Since this is the probability of a collision with a reservoir particle of velocity v, and the collision is elastic, it is also the probability distribution for the system particle ejected back into the system. This argument works fine for the ding-a-ling lattice. However, in the LPCO system, the free particles that enter the reservoir expect to interact with an ensemble of bound complex oscillators. In this way we are treating the reservoir as a large version of the lattice in equilibrium at $T = 2$. These bound particles are in an equilibrium distribution (Eq. (5.30)) but they don't move so they are all equally likely to interact with the free particle. That is, the probabilities are not weighted by their velocities. Thus the correct probability distribution to use to simulate a reservoir is the normalized equilibrium distribution Eq. (5.29).

With this modified reservoir distribution in place, we were able to produce thermal gradients and calculate energy fluxes; however, there were large fluctuations. This slow convergence was found to be due to the singular momentum distribution for the free particles. These slow particles were "frozen out" of the system for long periods. Longer run time improved the probability of getting yet slower particles in the system. Adding a noise floor to the velocities allowed the data to converge. From this converged data, we calculated a value for the thermal conductivity that appeared to be independent of length; however, we could not call it normal. The values of κ we found were dependent on the level of noise we added. In order to get convergence, the dynamical system had to be distorted in a fashion that made the results unrelated to a physical system, and we do not present the results.

In defining the LPCO model, we attempted to achieve some gain in computational efficiency over the ding-a-ling model by recognizing that in the stiff-spring limit the oscillator was approximately always at its lattice site. What we did not appreciate was the crucial role even these small oscillations play in the resulting velocity distribution of the free particle. In a ding-a-ling system if the free particle leaves a bound particle (after a collision) with a very small velocity it will likely have a second collision, with the same bound particle, that increases its speed. This means the probability that a free particle has a velocity within dv of 0 leaving a bound particle, in a ding-a-ling model, is 0. This is true even in the stiff-spring limit where the oscillations are small. In an LPCO system, a free particle leaving a bound particle never collides with the same bound particle in the subsequent collision. If it leaves with a small velocity, it will keep it. As a result, the probability of having a v within dv of 0 is finite. In fact, the velocity distribution is the same as the velocity distribution of the bound particle it just collided with (Gaussian).

So the LPCO model is *not* analogous to the stiff-spring ding-a-ling. The fixed (a)Free particle momentum distribution

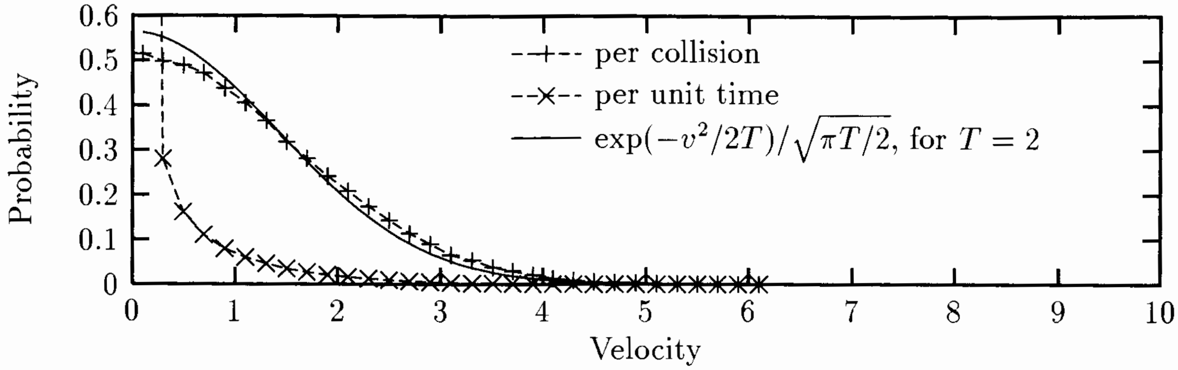

(b)Bound particle momentum distribution per collision

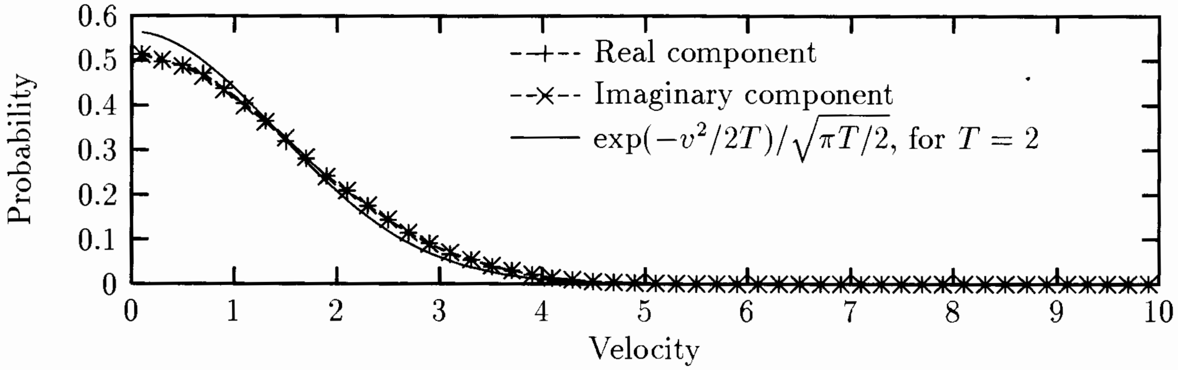

(c)Energy distribution

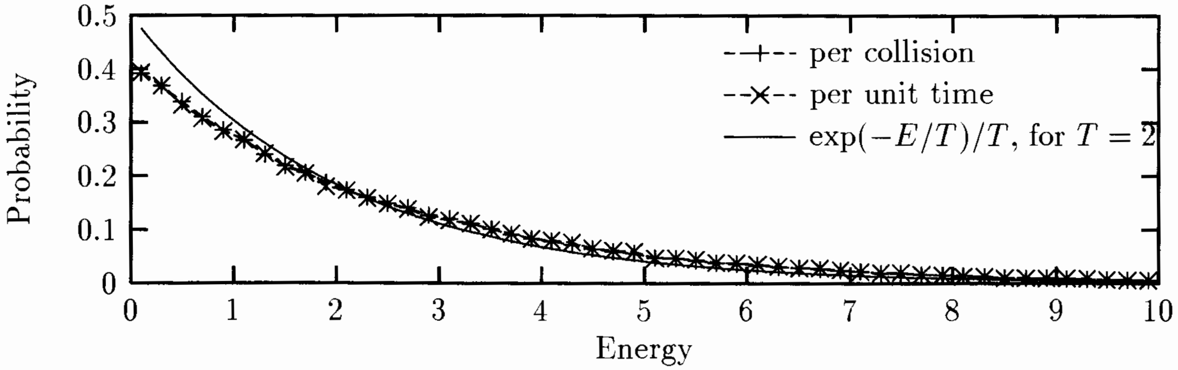

Figure 5.4: The energy and momentum distributions for the particles in the lattice. The reservoirs are Gaussian $\exp(v^2/2T)/\sqrt{\pi T/2}$.

positions of the "oscillators" are an over-simplification that leads to the pathological behaviour requiring custom reservoirs to establish stability. We should expect to be able to couple an LPCO system to a reservoir (at some T) of any kind of particles and have the lattice achieve equilibrium at the same T as the reservoir. Since this is not the case, it would appear that the LPCO model is not a physical system and should be abandoned.

5.2 Linearized Ding-a-ling

Recognizing that the LPCO model was too idealized, we suggest an alternative model. This model retains the simplicity of the ding-a-ling model but offers the possibility of greater computational efficiency without eliminating the position distribution of the bound particles to achieve this efficiency. In this model we replace the harmonic oscillators with constant forces that oppose motion away from the particles' origin. In terms of the potential energy we are replacing a parabolic potential with a piece-wise linear potential so we call the model the linearized ding-a-ling (LD). The Hamiltonian is

$$H = \sum_{i=1}^{N} \left(\frac{1}{2} v_i^2 + a_i |x_i| \right) + \text{hard point core}, \tag{5.32}$$

where a_i equals a for even i and zero for odd i and where all particles have unit mass. The dimensionless energy density is defined as $\varepsilon = E/a\ell_0$ (we will set $\ell_0 = 1$). The average energy of the potential term for the bound particle is

$$\frac{\int_{-\infty}^{\infty} a_i |x_i| \exp(-a_i |x_i|/T) dx}{\int_{-\infty}^{\infty} \exp(-a_i |x_i|/T) dx} = T. \tag{5.33}$$

Since equipartition of energy predicts the average kinetic energy of the free and bound particles is $\frac{1}{2}T$, the average energy of a free bound pair is T. We then have a definition of ε in terms of temperature,

$$\varepsilon = \frac{T_{\mathrm{m}}}{a}. \tag{5.34}$$

Comparing this with Eq. (2.2), we see that the coefficient of 3/4 has been changed to 1. This will be the "true" energy density in the small-amplitude limit, where the oscillator will be allowed to sample all of its range of oscillation.

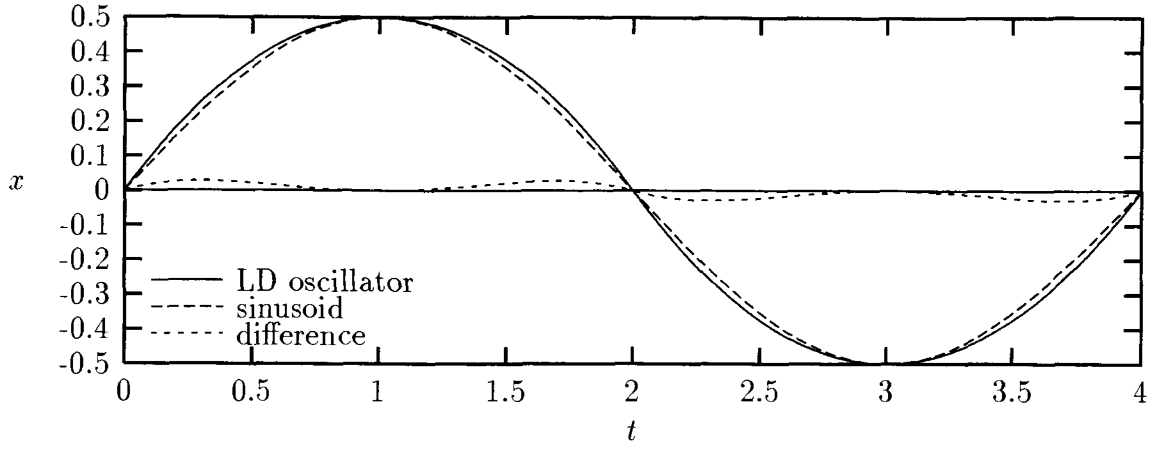

Figure 5.5: Comparison of the displacement for a harmonic oscillator and for the piece-wise linear potential used in the LD model.

As with the ding-a-ling model, between collisions the system is analytic. The evolution of the position of the particles between collision j and $j+1$ is

$$x_i(t) = \begin{cases} \frac{1}{2}u(t)a\left((t-\tau_j+\phi) \bmod \mathcal{T}/2\right)^2 + v_{ij}^0\left((t-\tau_j+\phi) \bmod \mathcal{T}/2\right) + x_{ij}^0 & i \text{ even} \\ v_{ij}^0(t-\tau_j) + x_{ij}^0 & i \text{ odd} \end{cases}$$
$$\text{for } \tau_j < t \leq \tau_{j+1}, \tag{5.35}$$

where ϕ is the phase, $\mathcal{T}$ is the period, and $u(t)$ is a step function that is defined as

$$u(t) = \begin{cases} +1 & (t-\tau_j+\phi) \bmod \mathcal{T}/2 < \mathcal{T}/2 \\ -1 & (t-\tau_j+\phi) \bmod \mathcal{T}/2 > \mathcal{T}/2 \end{cases}. \tag{5.36}$$

Although the equation of motion for the bound particle is more complicated than that for a harmonic oscillator, it looks very similar with the lobes of the sinusoid replaced by parts of a parabola. In Fig. 5.5, we compare the two motions. The collision criterion is still Eq. (2.4). This collision criterion demonstrates the advantage of the LD model. Since it no longer contains a trigonometric function, and does not require a root solver to evaluate the time of the collision. To demonstrate the proposed

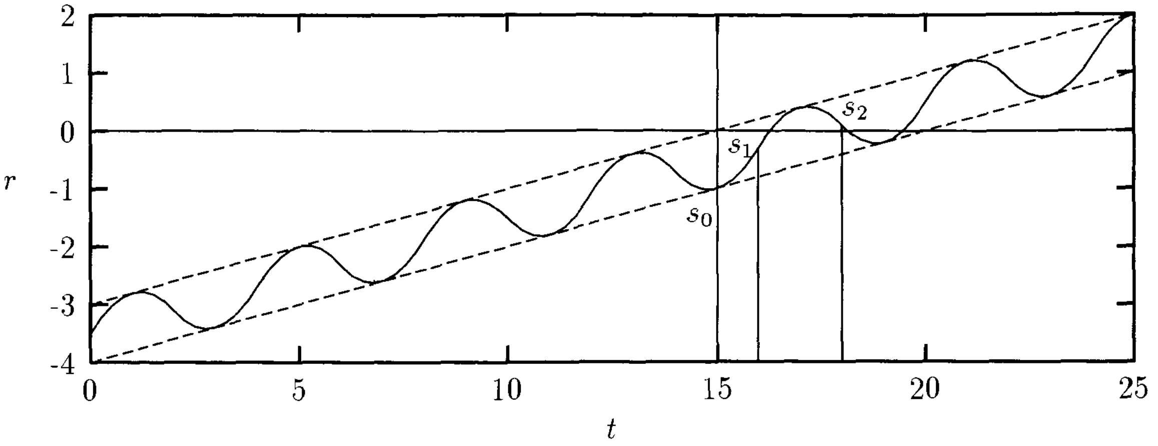

Figure 5.6: The collision function as a function of time. The dashed lines represent the maximum extension of the bound particle.

technique for solution, consider Fig. 5.6, which shows the collision criterion as the zero of

$$r(t) = x_i(t^0_{ij}) - x_{i+1}(t^0_{ij}) - 1. \tag{5.37}$$

The amplitude of the bound particle is $A = v^2/2a$, where v is the velocity at the origin. From this, we can establish when the oscillator is in range of the free particle (s_0 in the Fig. 5.6). Once this is done, we solve for the zero using the current parabola; if that zero occurs after the oscillator passes through its origin (reversing the acceleration), we then use the subsequent parabola (s_1 and s_2 mark these transitions). The collision event is found after a maximum of 2 functional evaluations, and the function itself is a polynomial, which is far more computationally efficient than evaluating a trigonometric function, as was needed in the ding-a-ling model.

With the LD model, we have addressed the issue of improved computational efficiency while avoiding the problems encountered by the fixed bound particle positions of the LPCO system. The only concern might be the effect of the discontinuous slope of the potential. Of course, the collisions themselves contributed effectively infinite potentials in the ding-a-ling model without causing any problems, so it seems reasonable to assume that these discontinuities will not be an issue in terms of establishing the thermal properties of the model.

Chapter 6

Conclusion

We have shown that, although CFVV were premature in their declaration, the ding-a-ling system does, indeed, obey Fourier's law. In fact, this Fourier law behaviour is very robust: the system shows normal thermal conduction for all parameter ranges, as long as the lattice is long enough. This indicates that, though normal thermal conductivity has appeared elusive in the past, this may perhaps be explained if the size of the lattices needed for the particular model studied were too large to compute. The computational efficiency and relatively short lattices needed in the ding-a-ling model allowed us to expose its full range of thermal dynamics.

It has been rather difficult to quantify normal thermal conductivity. Initial claims of normal thermal conductivity in both the ding-a-ling and diatomic Toda lattice have subsequently been shown to be premature. This indicates that the method of verification of this Fourier behaviour is important. Typically, we assume that the value of the thermal conductivity κ should be finite and independent of the length of the chain. This intensive property applies in the thermodynamic limit of large system size. By extrapolating resistivity $(1/\kappa)$ to infinite chains $(1/\sqrt{N} \rightarrow 0)$, we were able to show that the conductivity should not diverge for any finite dimensionless energy, ε. By performing this operation for a large range of parameters (ε and N), we validated the values of ε for which this extrapolation was credible. Beyond simply confirming Fourier-law behaviour, investigated the length scale for which normal thermal conductivity was reached. This was done using the square of the normalized slope of the resistivity, $\bar{\mu}^2$, as a function of ε. From $\bar{\mu}^2(\varepsilon)$, we found that for stiff-springs, the length of chain N_δ needed for normal thermal conductivity was insensitive to ε. For weak springs, N_δ was strongly dependent on ε, obeying a power law. To get a normal thermal conductivity required longer and longer lattices for larger ε. This $\bar{\mu}^2$ data therefore attempts to quantify what is meant by the thermodynamic limit.

The approach of the conductivity to its infinite-lattice limit is non-monotonic. This escaped the notice of CFVV and caused us a great deal of concern at first, since we were not expecting it. The literature is clear that the main culprit in the failures of attempts to verify Fourier's law has been the transport of energy via solitary pulses. This produces infinite thermal conductivity, so one would expect that, as one approaches the asymptotic normal thermal conductivity, it would be from above. This is not the case for the ding-a-ling model (or for the diatomic Toda model, for that matter). It is an interesting phenomenon whose explanation is not yet fully understood.

We have gained a better understanding of the ding-a-ling model. Its simplicity allowed us to make largely accurate predictions of certain quantities. Assuming a linear temperature dependence for the thermal conductivity, we predicted the shape of the temperature profile. We estimated the correct slope for $\kappa(T)$ from a fit using the predicted form of the temperature profile. The $\sqrt{\varepsilon}$ scaling of the conductivity in the stiff-spring limit was also verified. This approximation reduces the lattice to a single free particle between two reservoirs at the local temperatures. The randomness present, as a result of the strong chaos, allows the substitution of bound particles with reservoirs and the stiff springs allow for an accurate estimate of the free particles transit time. A similar approach worked well for estimates of the collision rate in the two limits, stiff- and weak-spring. The probabilistic approach was again successful at estimating the mean free path length of the soliton-like pulses. In our examination of the phase space, there were two notable fixed points that were analytically explored. The value of ε for the destruction of the main fixed point in the CFVV Poincaré sections was confirmed. The secondary fixed point had a periodic stability that could be predicted from linear stability analysis.

A dominant theme running throughout this work is the distinction between the stiff- and weak-spring limits. The reduced collision rate and the ratio of the dimensionless and actual energy densities most clearly show the extent of these asymptotic limits and the range of the transition region. In particular, they established that the changes in length scale of the thermal conductivity, κ, coincide with the onset of the stiff-spring limit. The onset of the weak-spring limit may also coincide with some interesting physics; however, this regime is more difficult to explore and most measured quantities have large error bars.

The graph of the log of the Lyapunov exponent versus the log of ε shows a change in slope at the same value of ε, as does the length scale $\bar{\mu}^2$. The importance of this result, besides being another dynamical measure that predicts changes in the conductivity of the system, is that it allows us to make contact with a theoretical basis for an understanding of the role of chaos in thermal conductivity. By drawing analogies with the work of Pettini and Landolfi [PL90], we suggest that there are differences between the thermal conductivity of a dynamical system that is weakly chaotic and one that is totally chaotic. Thermal conductivity across the lattice is affected when the trajectories in phase space are allowed to travel across as well as along the resonances.

We found no transition to infinite thermal conductivity, as all our calculations show that Fourier's law will be obeyed for a large-enough system. As $\varepsilon \to \infty$, the length of the system that is needed to approximate Fourier's law also diverges to infinity. Since $\varepsilon \to \infty$ is the integrable limit of the free particle gas, it would seem that the transition from finite to infinite thermal conductivity depends on the presence or absence of chaos.

Bibliography

[CFVV84] Giulio Casati, Joseph Ford, Franco Vivaldi, and William M. Visscher. One dimensional classical many body system having a normal thermal conductivity. *Physical Review Letters*, 52(21):1861, 1984.

[CLP95] Lapo Casetti, Roberto Livi, and Marco Pettini. Gaussian model for chaotic instability of Hamiltonian flows. *Phys Rev Lett*, 74(3):375–378, 1995.

[Dea60] P. Dean. Vibrational spectra of diatomic chains. *Proc. Roy Soc.*, 254:507, 1960.

[Dea61] P. Dean. Vibrational spectra of diatomic chains II. *Proc. Roy. Soc.*, 260:263, 1961.

[For92] Joseph Ford. The Fermi-Pasta-Ulam problem: Paradox turns discovery. *Physics Report (Review Section of Physics Letters)*, 213(5):271–310, 1992.

[Geb93] Benjamin Gebhart. *Heat conduction and mass diffusion.* McGraw-Hill series in mechanical engineering. McGraw-Hill, New York, 1993.

[GM92] O. V. Gendel'man and L. I. Manevich. Nonlinear dynamics of the diatomic toda lattice and the problem of thermal conductivity of quasi-one-dimensional crystals. *Sov. Phys. JETP*, 75(2):271, 1992.

[IC66] F. M. Izrailev and B. V. Chirikov. Statisical properties of a nonlinear string. *Sov. Phys. Dokl.*, 11(1):30, 1966.

[Ish73] K. Ishii. *Prog. Theor. Phys.*, (53):77, 1973.

[JM89] E. Atlee Jackson and Antonis D. Mistriotis. Thermal conductivity of one- and two-dimensional lattices. *J. Phys. Condensed Matter*, 1(7):1223–1238, Feb. 1989.

[JPW68] E. A. Jackson, J. R. Pasta, and J .F. Waters. Thermal conductivity in one dimensional lattices. *J. Comput. Phys.*, 2:207–227, 1968.

[KM93] Hideo Kaburaki and Masahiko Machida. Thermal conductivity in one dimensional lattices of Fermi-Pasta-Ulam type. *Physics Letters A*, 181:85–90, 1993.

[MA88] M. Mareschal and A. Amellal. Thermal conductivity in a one-dimensional Lennard-Jones chain by molecular dynamics. *Phys. Rev. A*, 37(6):2189, 1988.

[MB83] F. Mokross and H. Büttner. Thermal conductivity in the diatomic Toda lattice. *J. Phys. C:Solid State Phys.*, 16:4539–4546, 1983.

[MI70] H. Matsuda and K. Ishii. Localization of normal modes and energy transport in the disordered harmonic lattice. *Prog. Theor. Phys. Suppl.*, (45):56, 1970.

[Miu73] K. Miura. *The Energy Transport Properties of One-Dimensional Anharmonic Lattices.* PhD thesis, University of Illinois at Urbana-Champaign, 1973.

[MM95] Atsuhiko Maeda and Toyonori Munakata. Lattice thermal conductivity via homogeneous nonequilibrium molecular dynamics. *Phys Rev E*, 52:234–239, 1995.

[MT78] R. A. MacDonald and D. H. Tsai. Molecular dynamics calculations of energy transport in crystalline solids. *Physics Reports*, 46(1):1–41, 1978.

[NP64] Robert S. Northcote and Renfrey B. Potts. Energy sharing and equilibrium for nonlinear systems. *Journal of Mathematical Physics*, 5(3):383–398, 1964.

[NS90] Norihiko Nishiguchi and Tetsuro Sakuma. Temperature-dependent thermal conductivity in low-dimensional lattices. *J.Phys.Condens. Matter*, 2:7575–7584, 1990.

[PCS91] Marco Pettini and Monica Cerruti-Sola. Strong stochasticity threshold in nonlinear large Hamiltonian system: Effect on mixing times. *Phys Rev A*, 44(2):975–987, July 1991.

[Pei29] R. Peierls. Zur kinetischen theorie der warmeleitung in kristallen. *Ann. Phys.*, 3:1055, 1929.

[PL90] Marco Pettini and Marco Landolfi. Relaxation properties and ergoticity breaking in Hamiltonian dynamics. *Phys Rev A*, 41(2):768–782, January 1990.

[PRV67] D. N. Payton, M. Rich, and W. M. Visscher. Lattice thermal conductivity in disordered harmonic and anharmonic crystal models. *Phys Rev*, 160:706, 1967.

[PTVF92] William H. Press, Saul A. Teukolsky, William T. Vetterling, and Brian P. Flannery. *Numerical Recipes in Fortran.* Cambridge University Press, second edition, 1992.

[Ras90] S. Neil Rasband. *Chaotic Dynamics of Nonlinear Systems.* Wiley, New York, 1990.

[RLL67] Z. Rieder, J. L. Lebowitz, and E. Lieb. Properties of a harmonic crystal. *J. Math Phys.*, 8:1073, 1967.

[Tod75] M. Toda. Studies of a non-linear lattice. *Phys. Rep.*, 18C:1–123, 1975.

[Tod79] Morikazu Toda. Solitons and heat conduction. *Physica Scripta*, 20:424–430, 1979.

[Vis71] W. M. Visscher. Localization of normal modes and energy transport in the disordered harmonic chain. *Prog. Theor. Phys.*, (46):729, 1971.

[ZK65] N. J. Zabusky and M. D. Kruskal. Interaction of "solitons" in a collisionless plasma and the recurrence of initial states. *Phys. Rev. Lett.*, 15:240, 1965.